R·I·T

Lubrication and Wear Analysis of a Novel Squeeze Film Artificial Hip Joint

Submitted by

Sean A. Coots

A Thesis Submitted in Partial Fulfillment of the Requirements for Master of Science in Mechanical Engineering

Department of Mechanical Engineering

Kate Gleason College of Engineering

Rochester Institute of Technology

Rochester, NY

July 22nd, 2014

Lubrication and Wear Analysis of a Novel Squeeze Film Artificial Hip Joint

Submitted by

Sean A. Coots

A Thesis Submitted in Partial Fulfillment of the Requirements for Master of Science in Mechanical Engineering

Approved by

Dr. Stephen Boedo Department of Mechanical Engineering	(Advisor)
Dr. Steven Day Department of Mechanical Engineering	(Committee Member)
Dr. Steven Weinstein Department of Chemical Engineering	(Committee Member)
Dr. Agamemnon Crassidis Department of Mechanical Engineering	(Department Representative)

Abstract

Conventional artificial hip joints are characterized by inadequate ‘wedge film’ lubrication due to cyclic non-reversing loading and low frequency oscillatory ball motion. A novel ‘squeeze film’ design concept is presented which employs elastic restoring action and ellipsoidal cup geometry to enact separation of the bearing surfaces and improve lubrication behavior. Lateral and in-line design configurations were developed and analyzed using established finite element lubrication models with realistic gait cycle and bearing design specifications likely to be found in practice. An Archard-based wear formulation that relates contact pressure and sliding distance to linear wear depth was applied to the design configurations utilizing ANSYS to investigate the wear characteristics of the novel implant design. From a lubrication perspective, it was found that significantly larger minimum film thicknesses and significantly smaller maximum film pressures are predicted over the stance phase when compared with conventional designs, while complete reformation of the lubricant film is predicted over the swing phase of the gait cycle. From a wear perspective, it was found that low-modulus elastic elements with bonded high-modulus metal coatings offer significant improvement in volumetric wear rates and maintain acceptable levels of linear wear rates when compared with conventional implant geometries.

Acknowledgements

I have been very fortunate during this process to have been given exceptional guidance and substantial support from a number of sources. Foremost, I want to sincerely thank Dr. Stephen Boedo for the significant time and energy he provided during the course of this project; without his guidance and expertise, this thesis would not have been possible. I also want to thank the Department of Mechanical Engineering at the Rochester Institute of Technology – especially those associated with the graduate program and the staff members who have always been so helpful – for providing me the resources and facilities necessary for the completion of this project. Furthermore, I want to thank my committee members Dr. Steven Day and Dr. Steven Weinstein for their guidance. Lastly, I want to thank my family and friends, whose constant support and encouragement kept me focused and on schedule.

Table of Contents

List of Figures

List of Tables

Nomenclature

X,Y,Z	system coordinates	[L]
X',Y',Z'	system coordinates	[L]
X_N,Y_N,Z_N	lateral configuration system coordinates	[L]
X_N',Y_N',Z_N'	lateral configuration system coordinates	[L]
X_V,Y_V,Z_V	in-line configuration system coordinates	[L]
X_V',Y_V',Z_V'	in-line configuration system coordinates	[L]
X_C,Y_C,Z_C	conventional design system coordinates	[L]
X_C',Y_C',Z_C'	conventional design system coordinates	[L]
r_2	cup surface radius	[L]
R	reference radius	[L]
R_1	ball radius	[L]
R_2	cup surface nominal radius	[L]
δ	cup ellipticity	[L]
θ	spherical coordinate	[-]
C	radial clearance	[L]
C_0	nominal radial clearance	[L]
d	elastic column diameter	[L]
L	elastic column length	[L]
φ	contact angle of elastic columns	[-]
α	cup angle of inclination	[-]
β	slot centerline latitude angle	[-]
Δ_0	column radial offset	[L]
e	ball eccentricity	[L]
F	load	[L]
S	column stiffness	$[FL^{-1}]$
S^*	equivalent stiffness	$[FL^{-1}]$
S,s	sliding distance	[L]
E	elastic modulus	$[FL^{-2}]$
v	Poisson's ratio	[-]

ω	angular velocity	$[T^{-1}]$
t	material thickness	[L]
t	time	[T]
h	film thickness	[L]
h	linear wear depth	[L]
ρ	fluid density	$[ML^{-3}]$
p	film pressure	$[FL^{-2}]$
P,σ	contact pressure	$[FL^{-2}]$
P	external load	[F]
μ	fluid viscosity	$[FTL^{-2}]$
μ	coefficient of friction	[-]
v	ball velocity	$[LT^{-1}]$
k	wear coefficient	$[L^3F^{-1}L^{-1}]$
W	linear wear distribution matrix	[L]
n	angle of rotation	[-]
r	distance from node to axis of rotation	[L]
A	area	$[L^2]$
SA	surface area	$[L^2]$
CN	number of nodes 'in contact'	[-]
TN	number of total contact nodes	[-]

Chapter 1: Introduction

1.1 Background on natural and artificial hip joints

The natural human hip joint is a 'ball-in-socket' joint capable of transmitting high loads and accommodating a wide range of gait conditions and movements. Figure 1.1 shows a diagram of the natural hip joint. The femoral head (ball) is the upper part of the neck of the femur which is allowed the freedom to articulate within the acetabulum (socket) of the pelvic bone. A smooth layer of articular cartilage coats the surfaces of the femoral head and the socket, providing an elastic, porous surface for effective lubrication. The combination of high-strength ligaments (especially the acetabular labrum) and muscle tissue that surround the joint prevent dislocation and stabilize the joint during physical activity.

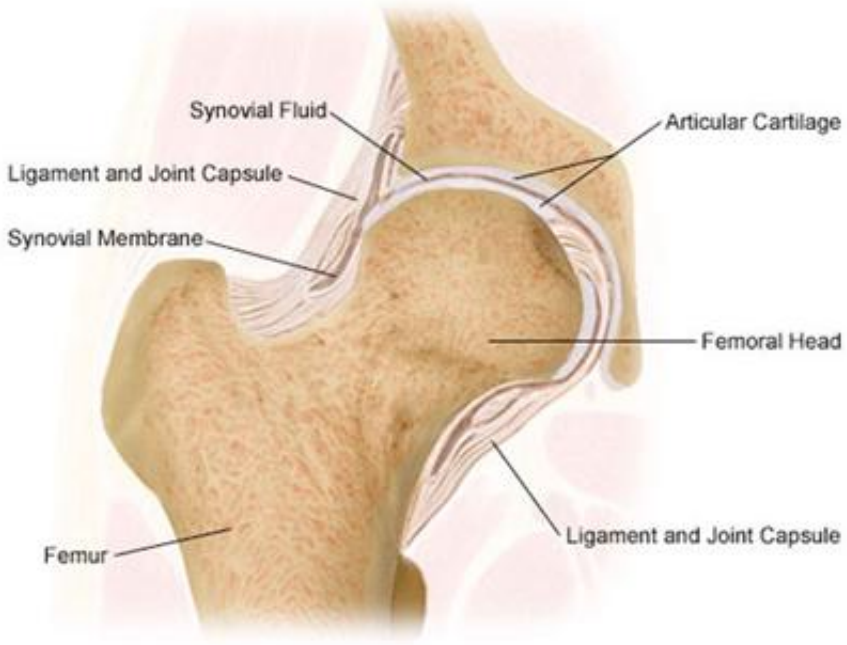

Figure 1.1: Natural hip joint [1]

The femoral head and acetabulum surfaces are spheroidal in nature and have a radius of curvature of approximately 25mm. The surface geometry of the joint varies between individuals but is characteristically shaped in a manner that promotes effective lubrication in the individual; hence, natural hip joints frequently last the person's entire lifetime [2]. The lubricant is called

synovial fluid and is a non-Newtonian, yolk-like fluid that is secreted by the synovial membrane within the joint. The articular capsule (or capsular ligament) is a strong, fibrous tissue that surrounds the femoral head, containing synovial fluid and stabilizing the joint [2].

The natural hip joint is the most important component of balance in the body and its orientation is the most important element of body posture. The hip joint is capable of transmitting high loads during physical activity and allows for a greater range of motion than any other human joint besides the shoulder. The combination of these capabilities coupled with its relatively high usage rate – especially in exercise-oriented individuals – can lead to biological issues in the joint. Due to repeated loading, disease and/or trauma, the hip joint can cause chronic pain or be physically damaged and require replacement, especially in older people. As such, a variety of hip implants have been developed over the past fifty years to replace the natural joint and provide relief to patients suffering from joint-related pain. These implants are essentially spherical bearings made of a variety of materials that are lubricated by synovial fluid secreted by the human body.

Total hip replacements (THR) typically consist of three components: the femoral stem, which is inserted into the hollowed-out center of the femur; the femoral head (or ball), which is attached mechanically to the femoral stem; and the acetabular cup, which often consists of a rigid backing that is fastened to the pelvis and a cup insert (or liner) that is bonded to the backing and typically of a softer material. Furthermore, there are three main types of material combinations used in THR surgery: metal-on-plastic (MOP), in which a (harder) metal ball articulates within a (softer) plastic cup; metal-on-metal (MOM), in which a metal ball articulates within a metal cup that is often the same material as the ball; and ceramic-on-ceramic (COC), in which a ceramic ball articulates within a ceramic cup. Figure 1.2 shows a typical MOP hip implant and its associated orientation in the human body.

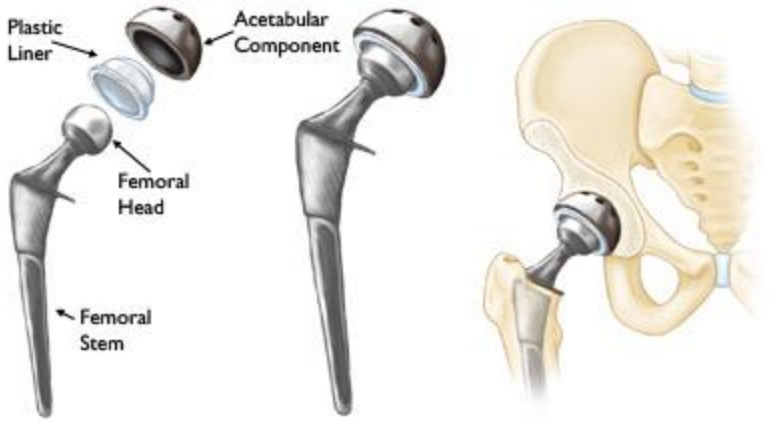

Figure 1.2: Conventional metal-on-plastic artificial hip joint [3]

There are, expectedly, many issues related to hip implants that affect their function and longevity *in vivo*. Specifically, wear particles generated from contact and friction between the articulating ball and cup surfaces have been shown to cause a variety of complications in the joint region. In MOP implants, wear particles from the softer polyethylene cup material have been shown to cause osteolysis, an auto-immune response that results in bone resorption specifically due to implant wear [4]. As a consequence of weakened and/or deteriorated bone in the implant region, aseptic loosening of the implant can occur, necessitating a revision surgery or total replacement of the implant. In metal-on-metal implants, nanoscale wear particles have been shown to cause high concentrations of metallic ions to be deposited in the tissue surrounding the implant [5, 6], and there is concern that these high ion concentrations will pose long-term health concerns [7-9]. Ceramic-on-ceramic implants are relatively more expensive and brittle in nature than MOP and MOM designs, necessitating especial attention to their fabrication and surgical insertion. Moreover, COC implants have been known to squeak during normal gait motions, an undesirable trait for any implant [10].

As such, a significant amount of research has focused on decreasing wear in total hip replacements in recent years. Notably, there has been a significant amount of work concentrated on nonspherical bearing surfaces, surface textures and materials, and implant size. Wang *et al.* [11, 12] pioneered the primary nonspherical efforts which were continued by others such as Meng *et al.* [13], though these studies often recommend unrealistically small clearance specifications. Surface textures and material selections have been a very popular avenue of research, beginning with the development of highly cross-linked polymers in the early 1990s that

improved wear characteristics to some degree [14]. More recently, surface coatings and finishes have been shown to decrease wear in certain cases, though their clinical use is highly restricted [15-18]. Implant size has become a major topic of study more recently due largely to the increased popularity of the MOM implant. There has generally been a switch to larger cup and head sizes to enhance stability and improve lubrication behavior. These larger designs are closer to the size of the actual human hip joint (25mm radius) [19].

Though these areas of research have contributed to lower predictions of wear in total hip replacements, they fail to address several key factors inherent specifically to hip implant functionality and are therefore limited in the magnitude of their improvement over conventional designs. Most significantly, the spherical bearing is subjected to non-reversing loading through the course of the gait cycle. According to *in vivo* load data and generally accepted hip simulator testing duty cycles such as the ISO 14242 standard [20], the gait cycle comprises a relatively high double-peak load upwards on the ball during the stance-phase (corresponding to heel-strike and toe-off) and a low-magnitude upwards force on the ball during the swing-phase, which can be attributed to muscle forces and lubrication behavior in the joint [21-23]. The nature of this unidirectional loading coupled with low-frequency oscillatory ball motion results in the limited hydrodynamic lubrication and undesirable levels of wear seen in conventional implants. This 'wedge-film' action alone functions as the lubricating mechanism in the joint, causing high film pressures and low film thicknesses over a relatively small 'point-contact' region between the ball and cup surfaces.

In an effort to address these issues, Boedo and Booker [24] have presented a novel design that incorporates elastic elements to provide a reversing load to the bearing during the swing-phase. By generating separation between the bearing surfaces, 'squeeze-film' action supersedes wedge-film action to enhance lubrication characteristics in the implant, which when combined with ellipsoidal cup geometry, leads to markedly smaller maximum film pressures and higher minimum film thicknesses during the stance-phase when compared with conventional designs. Similar analysis of the swing-phase employing a well-established transient mass-conserving finite element (FE) cavitation algorithm shows that complete reformation of the lubricant film is predicted after separation of the bearing surfaces over a wide range of gait cycle kinematics and bearing design specifications likely to be encountered in practice [25].

Effective wear rates for this proposed design have not been studied but are an integral component of this research since the elastic elements remain in direct contact with the ball surface at all times, albeit at significantly lower loads compared with the surfaces in a conventional implant.

1.2 Review of wear formulations

Quantifying wear rates in total hip replacements is an important but subjective area of research. Clinical results of wear rates present a wide range of values, primarily due to highly variable gait conditions, surgical orientation and implant size [26-30]. Moreover, *in vivo* clinical testing of wear rates require the implant to be removed from the patient, while hip simulator wear testing may not replicate the lubrication or gait conditions that exist in the body. As such, theoretical models of wear have become a popular tool to predict wear in implants in lieu of long-term clinical studies that are considerably more time-intensive and expensive. Specifically, sliding/abrasive wear formulations based on Archard's wear law [31] have been applied to hip implants in recent years, especially to MOP designs.

An early embodiment of this type of wear formulation was developed by Maxian *et al.* [30] in the mid-1990s to predict wear rates of MOP implants. This research details a sliding-distance-coupled formulation that relates contact pressures (in this case, found through a FE software package) directly to linear wear rates using sliding distance of nodes on the articulating surfaces. More recently, Mattei *et al.* provided a summary and comparison of existing wear formulations developed based on Archard's wear theory using a simplified FE model and analytic methods [32]. Adaptive wear models have been also used to more accurately predict long-term wear by updating the FE mesh according to wear results to effectively characterize the wearing-in of the implant [33, 34]. The more recent wear models have not, however, employed full three-dimensional FE models to obtain contact stresses but have preferred simplified models and analytic solutions in an effort to minimize computing time.

A sliding-distance-coupled wear formulation adapted from Maxian *et al.* [30] is applied in this work to the novel design to characterize wear rates of the elastic elements, which contact the ball surface during the entirety of the gait cycle. Furthermore, conventional models are

analyzed to determine whether the novel design is a feasible alternative from a wear standpoint to conventional hip implants.

1.3 Review of gait cycle conditions

Gait cycle conditions are a topic of extensive study and of particular importance to the prediction of lubrication and wear in hip implants. Due to body weight, muscle strength, movement activity of the patient and the surgical orientation of the implant (among many other variables), it is impossible to apply a single inclusive gait cycle that is representative of every patient [35]. As such, there are two main gait cycle categories in literature that are relevant to this work. The first are hip simulator duty cycles, which are typically characterized by smooth curves that provide a double peak in the stance-phase of the same value (typically greater than 2000N) and a constant low-magnitude swing-phase load (typically between 0N and 300N). The ISO 14242 specification [20] is considered the golden standard for many lubrication and wear analyses. Additionally, the conditions applied using the Leeds ProSim hip simulator are well documented [32, 36, 37] and other hip simulator data from the Hospital for Special Surgery has been applied in lubrication analyses [38]. These gait conditions are preferred by some authors due to institutional history and their reproducibility from a testing standpoint.

The second category of gait cycles consist of data found experimentally through the use of pressure plates and later instrumented implants in total hip replacement patients. Bresler and Frankel [39], Rydell [40], and Paul [41], among others, pioneered the experimental study of hip joint forces and kinematics in the 1950s and 60s. The most extensive experimental data has been collected by Bergmann and his associated colleagues [21-23, 42, 43] in more recent years, though work by Brand *et al.* [44] is also heavily referenced. A particularly helpful review of experimental studies through 1997 is presented by Andriacchi and Hurwitz [45]. Issues with these types of studies center on the small quantity of data taken, as very few patients have participated. Moreover, the experimental data is highly variable and especially dependent on body weight and the movement being performed by the patient. These studies commonly present results in terms of body weight of the patient – essentially making these gait cycles specific to a single person – and they hardly can be considered representative of a majority of patients.

Due to the high variability in published gait conditions and the computing time required to run lubrication analyses, it is difficult to prove that a certain implant design or material selection will be effective in every patient. As such, this work builds on the predictions in Boedo and Booker [24, 25] employing the ISO 14242 specification due to its general acceptability among artificial hip joint designers.

1.4 Thesis objectives

There are two main objectives for this thesis. First, the characterization of wear in the novel implant and its comparison to conventional designs is an integral part of this research. Lubrication results for this design may be favorable, but there is direct continued contact between the elastic elements and the femoral head in the novel implant design, and the effects of this contact from a wear perspective are unknown. The primary focus of this thesis therefore is to predict wear rates of the novel design to gauge whether it is a viable implant design when compared against wear rates in conventional designs. This process requires the application of a sliding-distance-coupled wear formulation and the use of three-dimensional, non-linear contact analysis using a finite element program.

Second, alternative design orientations that are governed by the same qualitative principles as the novel design configuration presented by Boedo and Booker [24] – namely alternative methods and/or geometries that incorporate the elastic elements – are to be investigated. These alternative configurations are to be subjected to the same lubrication and wear analyses as the novel lateral design configuration. This process requires the comparison of both lubrication behavior and wear results to the novel and conventional designs to gauge the alternative configuration's viability. The lubrication analysis is to be presented in a similar manner to Boedo and Booker [24, 25].

1.5 Organization of thesis

This thesis is organized into six chapters and two appendices. Chapter 1 provides an introduction to the natural hip joint and the conventional artificial hip joint. It also includes brief literature reviews regarding the application of wear theory to artificial hip joints and the human gait cycle.

Chapter 2 introduces the novel squeeze film artificial hip joint design. It is further organized into three sections: a review of the novel design and the specific configurations investigated in this thesis, a discussion of the qualitative function of the novel design and its relation to the human gait cycle, and a discussion of the lubrication behavior in conventional designs. This chapter defines the coordinate systems, design specifications, fluid-film meshes and FE contact models for the novel and conventional design configurations.

Chapter 3 presents the stance phase lubrication analysis for the novel design configurations. This includes a review of the lubrication results predicted by Boedo and Booker [24] for the specific configuration presented in that paper. This chapter defines the modeling assumptions used for lubrication analysis and presents the dimensional results for the alternative design configuration investigated in this thesis.

Chapter 4 presents the swing phase lubrication analysis for the novel design configurations. It contains a review of the swing phase results predicted by Boedo and Booker [25], which center on the formation and collapse of the cavitation region in the implant. This chapter details the modeling assumptions associated with the swing phase and presents the dimensional results for the alternative design configuration.

Chapter 5 presents the wear analysis of the novel and conventional designs that are defined in Chapter 2. This chapter explains the FE contact analysis methodology and the wear formulation applied to the various implant designs. The results are organized in the following manner: first, the wear predictions for the conventional design are evaluated as the control case; second, the wear rates for the novel design configurations are presented and compared against the conventional results; and third, supplemental studies are presented that focus on the effects of friction, radial clearance and cup ellipticity on wear.

Chapter 6 provides a summary of the results presented in Chapters 3, 4 and 5. This chapter further formulates a series of conclusions taken from the lubrication and wear results evaluated in this thesis regarding the viability of the novel design configurations.

Appendix A details the validation of the methodologies applied to the finite element modeling and contact analysis used in this thesis. This includes validation studies on simplified geometries (sphere-on-plane, sphere-on-cup, and axisymmetric models), explanation regarding the meshing procedure applied to the FE models, and a summary of the mesh density and refinement studies completed on the models to ensure accuracy of results. Furthermore, there is a section that validates the conventional design used in this thesis.

Appendix B contains a brief discussion regarding the validation of the time steps and fluid-film mesh densities associated with the lubrication analysis in this thesis.

Chapter 2: The Novel Squeeze Film Artificial Hip Joint

2.1 Geometry

2.1.1 Lateral design

The following section is largely taken from Boedo and Booker [24] and is described here to provide the necessary background information for this work. Figure 2.1 shows the physical embodiment of the 'lateral' design. The acetabular cup is ellipsoidal in nature and can be divided into 'rigid' and 'elastic' elements. (The 'rigid' denotation is used solely to distinguish from the much more compliant 'elastic' elements, as there is an inherent elasticity to the 'rigid' material of the cup.) In their unstressed position (the point of initial contact between the elastic elements and the ball surface), the elastic columns protrude into the clearance space of the bearing so that contact is maintained over both the stance and swing phases of the gait cycle. It should be noted that this design is only one possible configuration of the concept of supplying a reversing load in the implant using elastic elements.

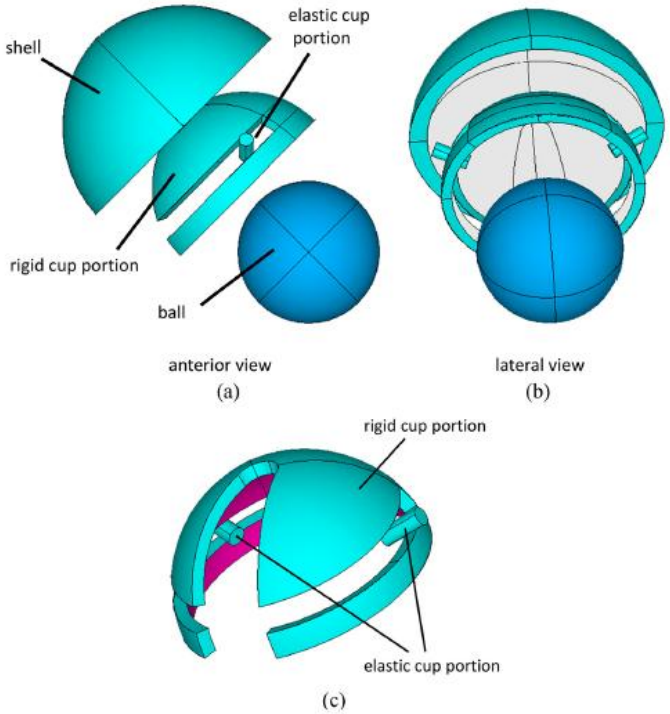

Figure 2.1: Novel hip implant design, lateral configuration [24]

Figure 2.2 defines the coordinate systems used by Boedo and Booker [24] and consequently in this work. System X, Y, and Z axes are oriented along the abduction-adduction, flexion-extension, and internal-external rotation axes of the implant, respectively, while coordinate system X'-Y'-Z' is affixed to the cup with the Z'-axis oriented along the cup polar axis.

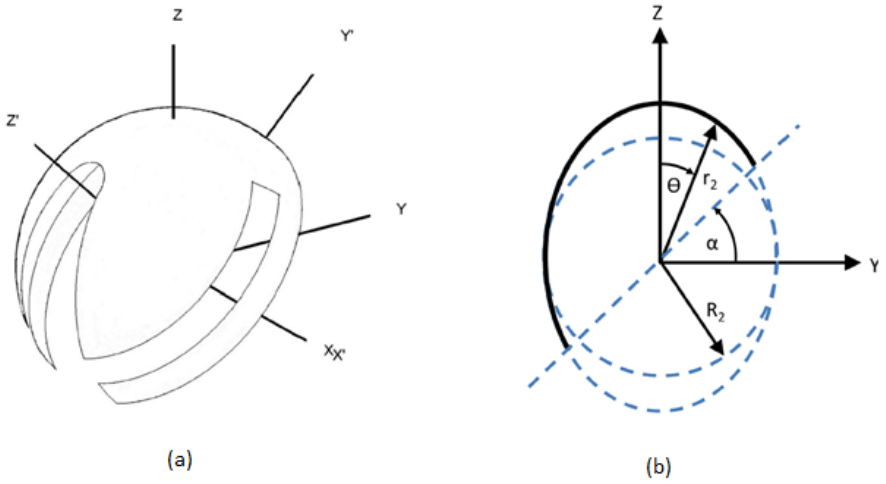

Figure 2.2: Coordinate system and surface geometry of rigid cup [24]

The ellipsoidal cup surface is oriented with its major axis in the vertical Z-direction and its surface radius r_2 is defined by

$$r_2 = R_2 + \delta \cos^2 \theta \tag{2.1}$$

where R_2 is the nominal radius of the cup; δ is a prescribed ellipticity parameter; and θ is a spherical coordinate with respect to the positive Z-axis. The radial clearance C between the bearing surfaces is thus given by

$$C = C_0 + \delta \cos^2 \theta \tag{2.2}$$

with nominal clearance $C_0 \equiv R_2 - R_1$.

Figure 2.3 shows a spatial view of the lubricant film that is associated with the rigid portion of the cup surface used by Boedo and Booker [24]. The film is represented by a contiguous set of three-noded planar triangular finite elements. Figure 2.4 displays a view of the lubricant film mesh projected onto the X'-Y' plane. The mesh is displayed as an equal area

projection, meaning that the surface area of the hemispherical mesh and the projected planar mesh are equivalent. The fluid-film meshes are discussed in further detail in Chapters 3 and 4.

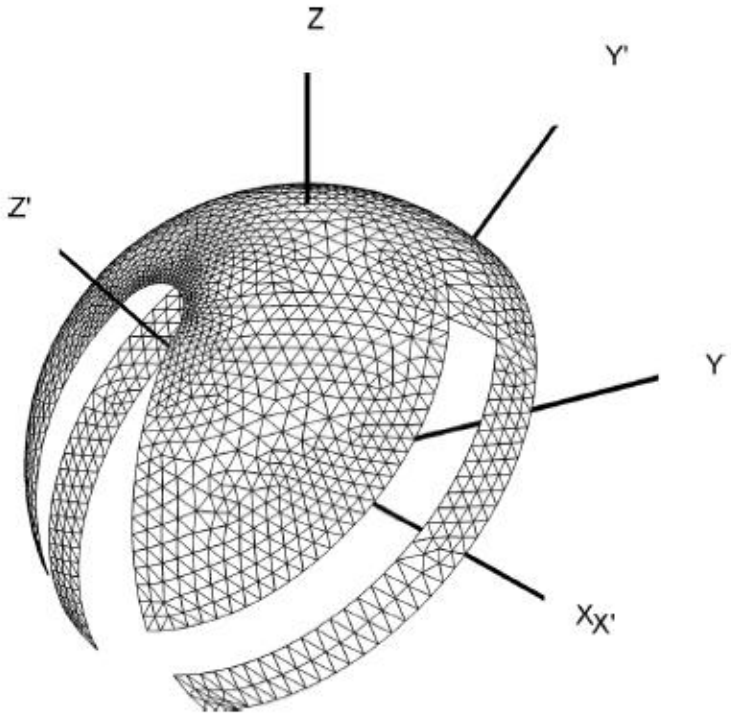

Figure 2.3: Spatial view of lubricant film mesh [24]

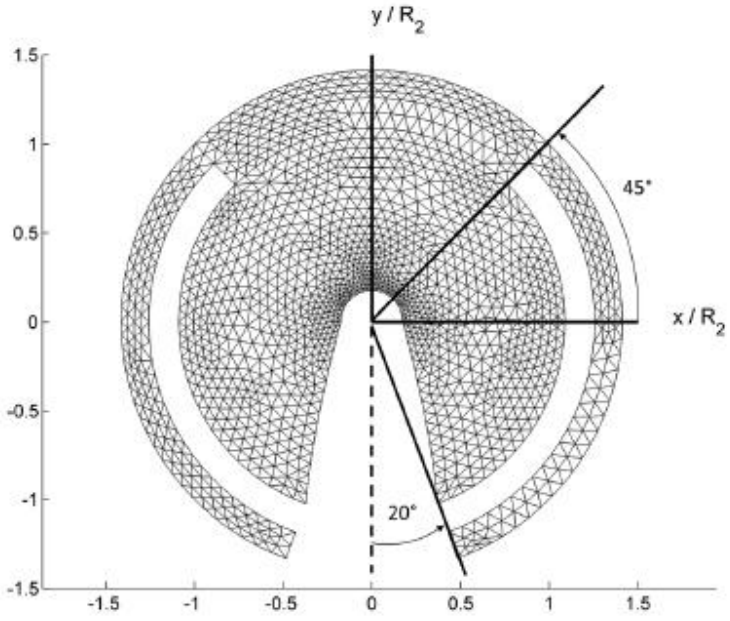

Figure 2.4: Equal area projection of lubricant film mesh [24]

Figure 2.5 shows sectional views of the rigid and elastic elements of the acetabular cup and their associated parameters. The columns are dimensioned by diameter d_c and length L and are oriented at a contact angle φ. Since the columns must pass through the narrow slots of the cup surface, their diameter values are restricted; the maximum allowable diameters for the columns are 3.18mm and 4.97mm for the 16mm and 25mm radius cups, respectively.

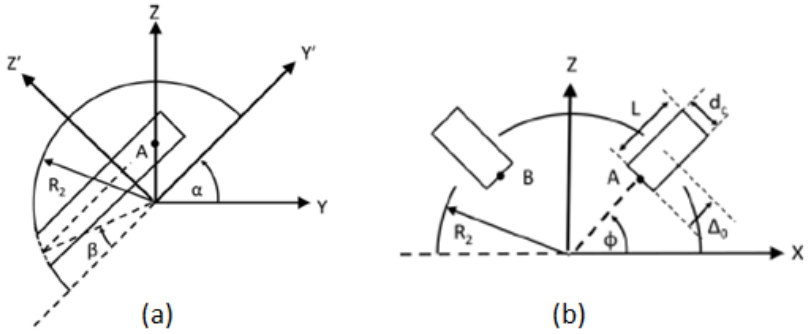

Figure 2.5: Column geometry [24]

The contact angle φ is dependent upon the inclination angle α and the slot centerline latitude angle β and is given by

$$\sin\varphi = \sin\beta \,/\, \cos\alpha \tag{2.3}$$

In their unstressed state, the columns protrude a radial distance Δ_0 into the clearance space of the bearing. As such, at the point of initial contact between the ball and the elastic elements there exists a vertical 'offset' distance $\boldsymbol{e}_0$ along the Z-axis between the center of the ball and the center of the cup given by

$$\boldsymbol{e}_0 \equiv e_0\boldsymbol{k} = -(\Delta_0/\sin\varphi)\boldsymbol{k} \tag{2.4}$$

Assuming linear compression of the columns, the effective spring force $\boldsymbol{F}_{elast}$ transmitted from ball to cup in the Z-direction is given by

$$\boldsymbol{F}_{elast} = S(e^z - e_0)\boldsymbol{k} \tag{2.5}$$

where $e^z > e^0$ is specified ball eccentricity (position), and S is the effective stiffness of the columns given by

$$S = \left(\pi {d_c}^2 E \sin^2\varphi\right)/(2L) \tag{2.6}$$

where E is the elastic modulus of the column material. As the value of e^z is limited by the clearance between bearing surfaces and is a relatively small value compared with e_0, $\boldsymbol{F}_{elast}$ increases only a small percentage above the prescribed reaction load value due to the columns (set at 350N) [24, 25].

A design feature yet to be discussed is the radial slot present in the rigid cup portion of the implant. This slot controls film load direction and promotes lubricant transportation to the load-carrying portion of the cup. Its presence in the design results primarily in smaller maximum film pressures when compared with a full hemispherical cup design.

It is not necessary to model the entire lateral design during contact analysis. Therefore, this design is modeled without the rigid acetabular cup, as the contact occurs only between the elastic columns and the ball surface. Figure 2.6 shows the novel design FE model. System X_N, Y_N, and Z_N axes are oriented to correspond to the system X, Y, and Z axes given by Boedo and Booker [24], respectively, where the centerlines of the columns lie in the X_N-Z_N plane. The X_N'-Y_N'-Z_N' frame is affixed to the contact surface of the left elastic column in Figure 2.6a, where X_N' is oriented along the cylindrical axis of the column 'into' the surface and lies in the X_N-Z_N plane. The back surface of each column is assumed to be fixed, while the ball is constrained to move only in the Z_N-direction.

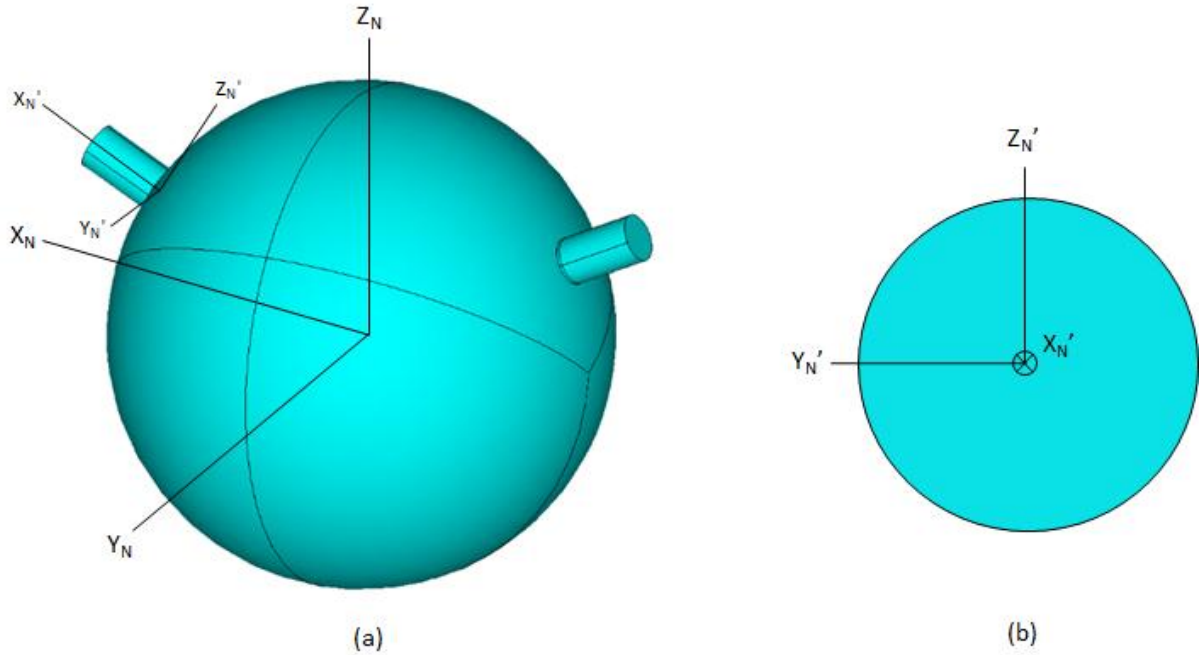

Figure 2.6: Novel design FE model, lateral configuration

The design specifications shown in Table 2.1 are adapted directly from Appendix C of Boedo and Booker [24] and follow the theory provided previously in this section. Due to the geometry of the acetabular cup, the maximum allowable diameters for the columns are 3.18mm and 4.97mm for the 16mm and 25mm radius cups, respectively. The diameter values used in this work are chosen so as to maximize the contact area on the column surface to provide lower contact stresses and a comparable effective reaction force to the theoretical value of 350N given in Appendix C of that paper. Validation of the mesh densities applied to the novel design models can be found in Appendix A of this work.

Parameter	$\mathbf{d_c}$	$\mathbf{e_0}$	**L**	**Φ**	$\mathbf{E_{ball}}$	$\mathbf{\nu_{ball}}$	$\mathbf{E_{columns}}$	$\mathbf{\nu_{columns}}$
Units	mm	mm	mm	°	GPa	-	GPa	-
R = 16mm	3.0	-0.648	5	25.9	210	0.31	1.0	0.46
R = 25mm	3.5	-0.476						

Table 2.1: Design parameters for lateral element configuration

In addition to this particular design, which employs low-modulus elements as the contact structures, models including high-modulus coatings are simulated that are bonded to the contact surfaces of the elastic columns. These coating are a thin layer of metallic material with the same elastic modulus and Poisson's ratio as the ball (210 GPa and 0.31, respectively). The coatings are applied in an effort to lower the material removal rate of the elastic elements and increase the lifespan of the implant.

Two coating thicknesses are simulated: 200µm and 400µm. These values are taken from published literature as common coating thicknesses simulated in hip implant lubrication studies [16-18]. Figure 2.7 shows the FE model used for the 200µm-thickness case, using the same coordinate systems as shown in Figure 2.6. The geometric parameters listed in Table 2.1 apply to this design. It should be noted that the length of the column L increases from 5mm to 5.2mm and 5.4mm for the 200µm and 400µm thicknesses, respectively. Due to the large difference in elastic moduli between the polyethylene and cobalt-chrome materials that make up the elastic columns, the initial vertical offset e_0 remains the same for the coated models as for the uncoated models. This validation is detailed further in Appendix A.

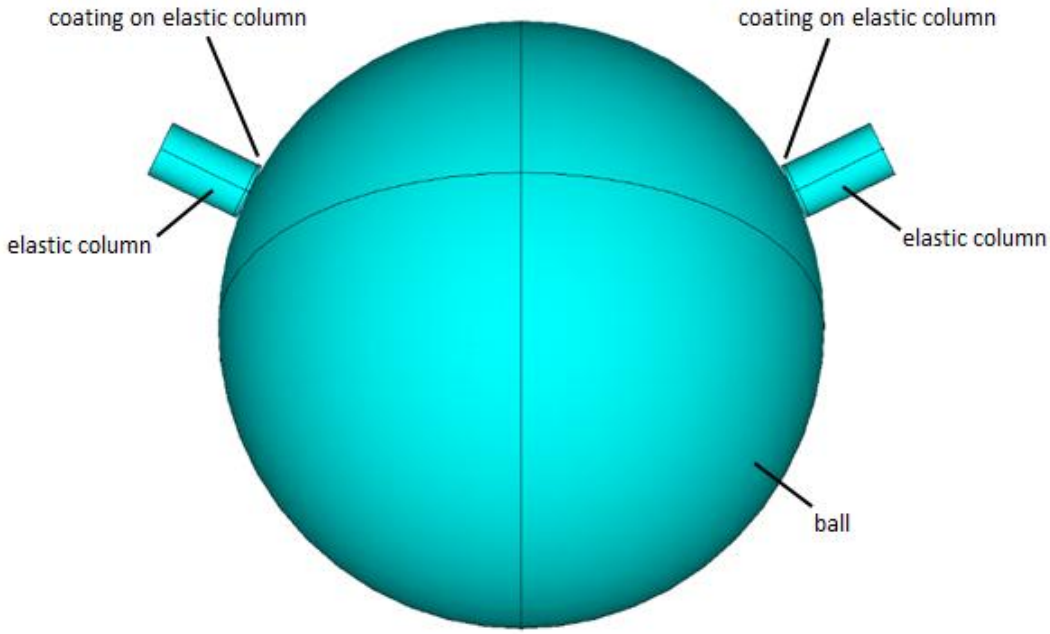

Figure 2.7: Coated lateral design FE model

2.1.2 In-line design

The second design that is simulated in this work places the location of the elastic portion of the cup at the pole (aligned with the Z-axis). The 'in-line' design therefore only requires a single column to provide the reaction load to the top of the ball. This design is easier to manufacture than the lateral design, as only a single elastic column is required in the implant in an orientation that is likely to be more simply assembled.

Figure 2.8 shows the physical embodiment of the in-line design. In contradistinction to the lateral design, the acetabular cup for the in-line design includes a single hole centered at the peak ellipticity location (where the Z-axis passes through the cup). There are no slots in this design and therefore no particular limits on the size of the elastic element, though a smaller column provides a larger lubricant film to carry the load in the bearing.

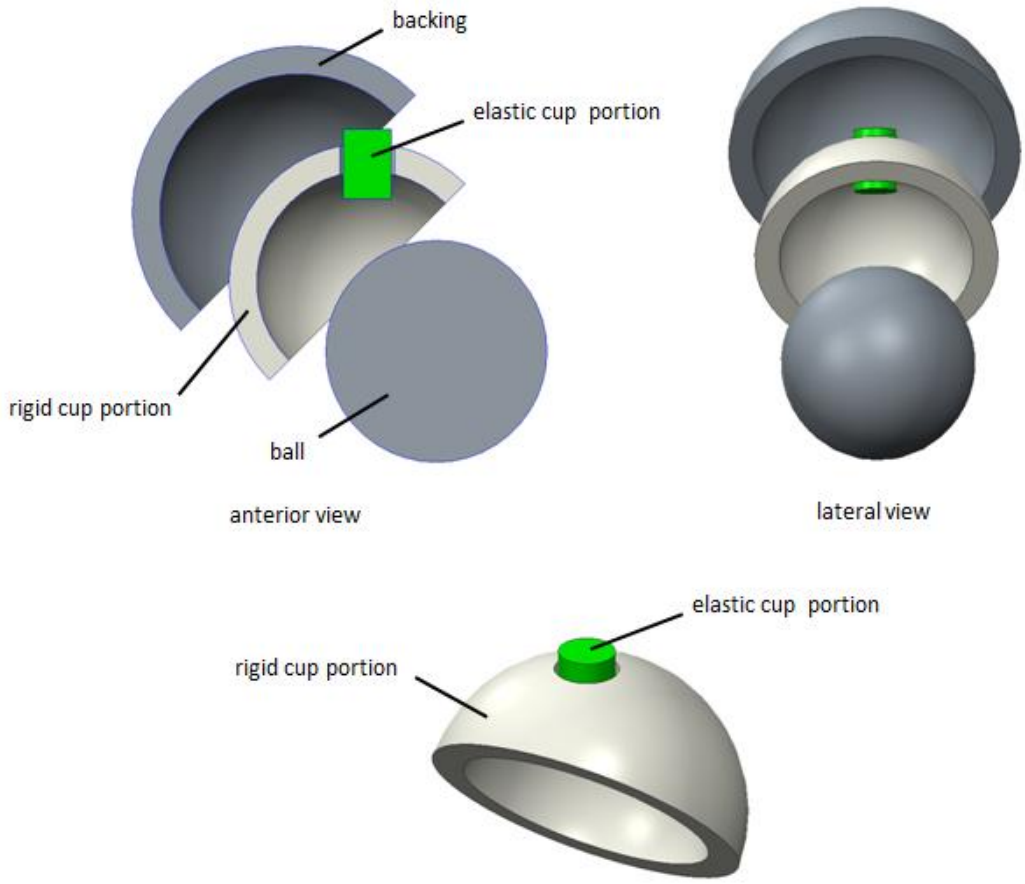

Figure 2.8: Novel hip implant design, in-line configuration

Figure 2.9 shows a spatial view of the lubricant film that is associated with the rigid portion of the cup surface used for the in-line configuration. Figure 2.10 displays an equal area projection of the lubricant film mesh onto the X'-Y' plane. The fluid-film meshes are discussed in further detail in Chapters 3 and 4. Note that the diameter of the clearance hole located at the polar axis of the cup in these meshes is equal to 4mm, which corresponds to the largest diameter elastic column that is simulated for the wear calculations presented in Chapter 5.

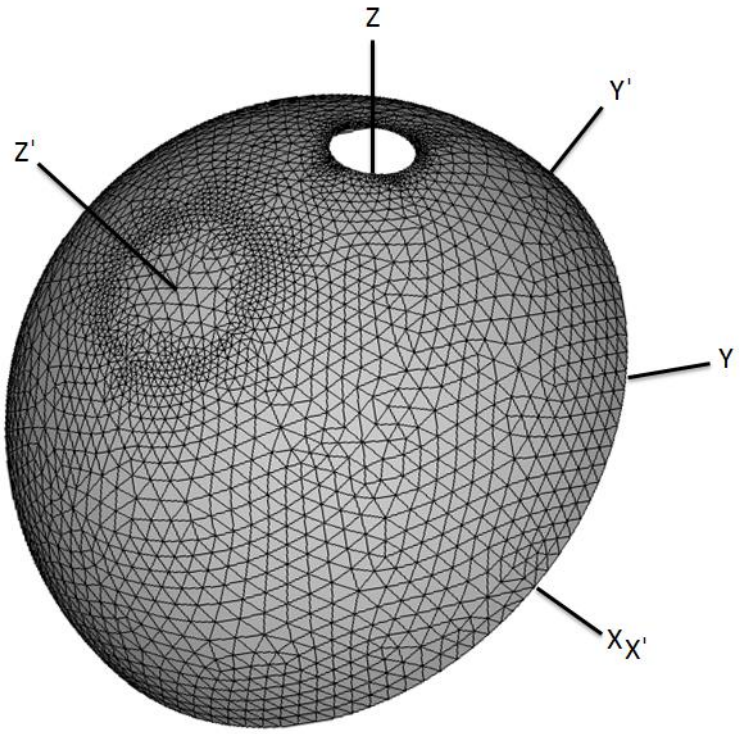

Figure 2.9: Spatial view of lubricant film mesh, in-line configuration

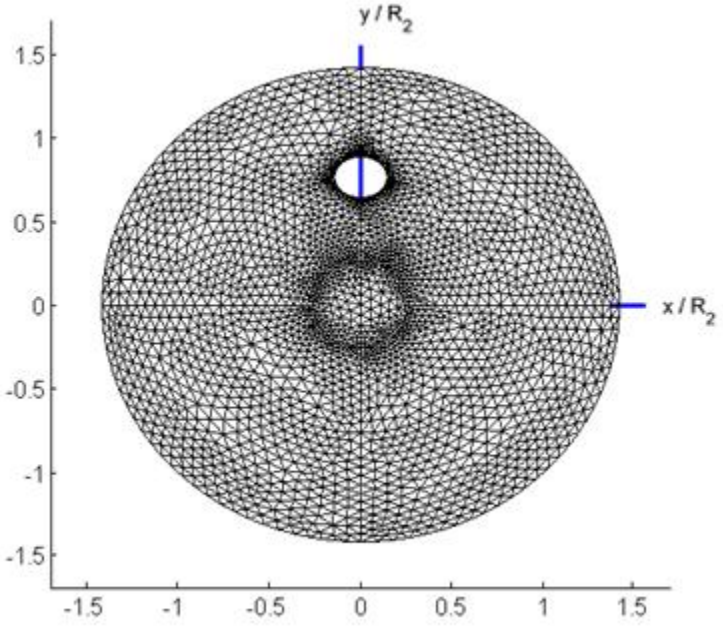

Figure 2.10: Equal area projection of lubricant film mesh, in-line configuration

A similar approach is applied to this design as for the lateral design in Section 2.1.1 to calculate the initial vertical offset e_0. Assuming pure compression of the column, the stiffness S_V is given by

$$S_V = \frac{AE}{L} = \frac{\pi E {d_v}^2}{4L} \tag{2.7}$$

where A is the cross-sectional area of the column; E is the elastic modulus; L is the length of the column; and d_v is the cross-sectional diameter of the column. The required deflection e_0 to obtain the desired net reaction load $\boldsymbol{F}_{elast}$ is related to the stiffness S_V:

$$\boldsymbol{F}_{elast} = S_V(e^z - e_0)\boldsymbol{k} \tag{2.8}$$

where e^z is a specified ball eccentricity greater than e_0.

The 4.0mm diameter FE contact model and its associated X_V-Y_V-Z_V coordinate system, which is oriented in the same manner as system X_N-Y_N-Z_N, are shown in Figure 2.11. The back side of the elastic column is assumed to be fixed and the model is constrained to only allow motion only in the Z_V-direction. The X_V'-Y_V'-Z_V' coordinate system is attached to the contact surface of the elastic column, where the Z_V' axis is directed 'into' the surface. The X_V'-Y_V'-Z_V' can be thought of as the X_V-Y_V-Z_V system shifted in the $+Z_V$-direction until the contact surface of the vertical column lies in the X_V-Y_V plane.

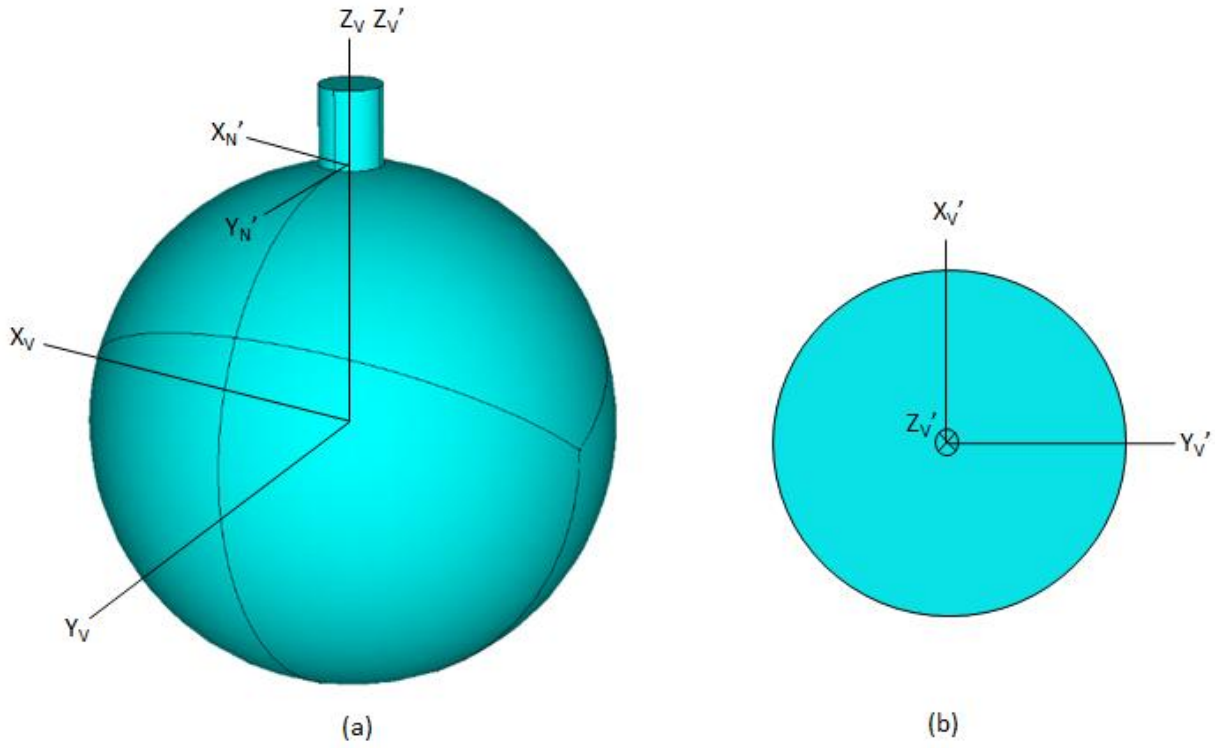

Figure 2.11: In-line novel design FE model

Three column diameters d_v are simulated for both the 16mm and 25mm radius models to better understand the affect that column size/stiffness has on calculated contact stresses in the in-line orientation. The initial vertical displacement e_0 is chosen a 350N elastic load. The parameters for these models are shown in Table 2.2.

Parameter	$\mathbf{d_v}$	$\mathbf{e_0}$	**L**	$\mathbf{E_{ball}}$	$\mathbf{\nu_{ball}}$	$\mathbf{E_{column}}$	$\mathbf{\nu_{column}}$
Units	mm	mm	mm	Gpa	-	Gpa	-
Model 1	3.00	-0.248	5	210	0.31	1.0	0.46
Model 2	3.50	-0.182					
Model 3	4.00	-0.139					

Table 2.2: Design parameters for in-line design models

In addition to the standard low-modulus elements, coated columns are also simulated. Similarly to the coated lateral design models, the coatings that are employed in this orientation are 200μm and 400μm thick. Figure 2.12 displays the FE model used for the 400μm-thickness, 4.0mm diameter case (this is the only diameter model simulated with coatings). Again, the

coatings have the same material properties as the ball and backing (that is, an elastic modulus of 210 GPa and Poisson's ratio of 0.31). These models use the same coordinate systems as the uncoated in-line models (X_V-Y_V-Z_V and X_V'-Y_V'-Z_V', see Figure 2.11). Furthermore, the design parameters in Table 2.2 apply to the coated models as well, with the exception that *L* increases from 5mm to 5.2mm and 5.4mm for the 200µm and 400µm thicknesses, respectively. Validation of the mesh densities applied to the in-line models can be found in Appendix A.

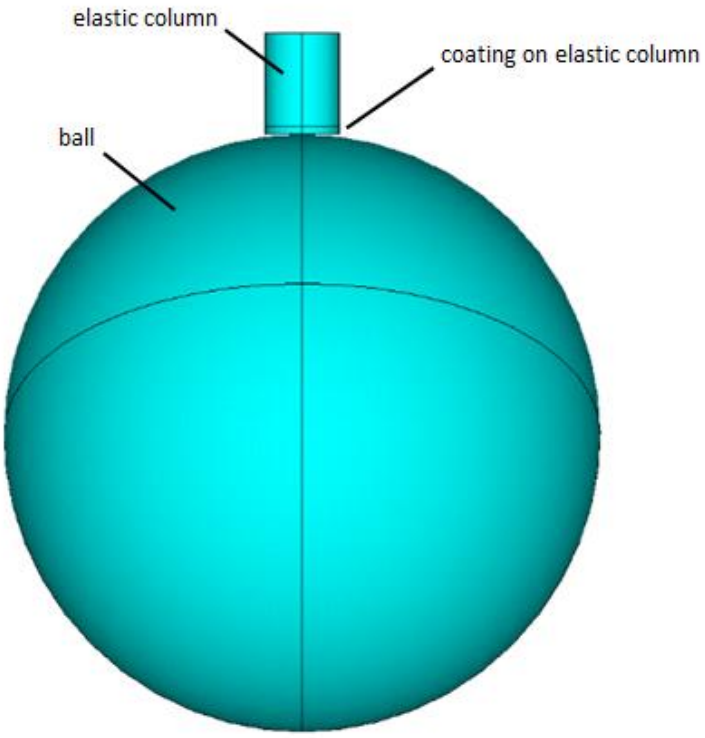

Figure 2.12: Coated in-line design FE model

2.2 Kinematics and dynamics

The primary inhibitor to extended life of conventional hip implants is the wear of the articulating bearing surfaces. Wear-related failures continue to account for the majority of revision surgeries in both MOP and MOM total hip replacements [19]. The conclusions drawn

from clinical studies center on a singular principle: wear is the major concern in hip implants. But what causes wear in implants, and how can these sources of wear be resolved?

A more complete response to this question is addressed in Section 2.3; for the sake of brevity, the most important cause of wear is that conventional hip implants are inherently different than the natural hip joint, which does not have a spherical geometry and incorporates significantly different materials in the lubricated regions. Spherical implants are characterized by wedge-film action, which is in many cases an inadequate lubrication mechanism that leads to relatively small film thicknesses and large film pressures. This wedge-film action is caused primarily by the relatively high-magnitude, non-reversing loading of the implant coupled with low-frequency oscillatory ball motion that results in a very small load-carrying region of the lubricant film that approaches point contact.

The novel squeeze film design addresses the associated issues causing wedge-film action in conventional implants by employing elastic elements and an ellipsoidal cup geometry to promote squeeze-film action. The elastic elements generate a reaction load on the ball to enact separation of ball and cup during the swing phase of the gait cycle. Moreover, the ellipsoidal nature of the cup leads to the bifurcation of the contact region from point contact to circular line contact as the ellipticity factor δ increases with respect to the nominal clearance in the bearing. By effectively increasing the contact region and providing a reversing load to the system, squeeze-film action supplants wedge-film action in the implant, leading to larger film thicknesses and smaller film pressures.

There are two main segments of the (walking) gait cycle that are important to lubrication in the hip joint: the stance phase and the swing phase. The stance phase is the period in which the foot is planted on the ground and is characterized by a double-peak loading on the hip joint that corresponds to heel-strike and toe-off. During this segment of the gait cycle, the major portion of the load is carried by the lubricant film transmitted to the cup through squeeze-film action, which allows the implant to maintain surface separation. A minor portion of the load is transmitted through direct contact with the elastic elements. Figure 2.13 provides a pictorial representation of the function of the novel design during the stance phase.

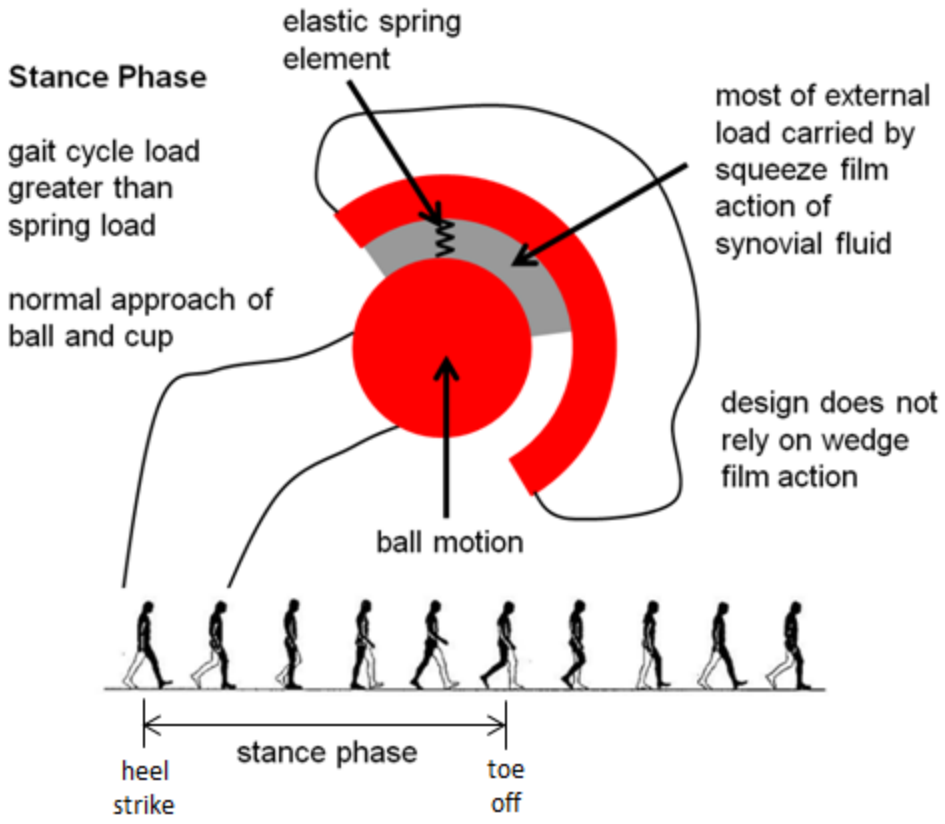

Figure 2.13: Function of the novel THR during the stance phase

The swing phase is the period in which the foot is free from ground contact between toe-off and the next heel-strike. This segment is characterized by a low-magnitude load on the joint in the same direction as during the stance phase. This seems contrary to common sense, in which one would expect a natural separation of the ball and cup due to the force of gravity acting on the leg. This is not the case; due to muscle tension, lubricant behavior and other tissue-related effects in the hip region, a net load is transmitted to the joint that prevents separation. The elastic elements are designed to provide a reaction force greater than the swing phase load to the ball during the swing phase that initiates normal separation of the ball and cup surfaces. Cavitation of the lubricant film occurs at this point; pressures in the cavitation region are generally believed to be sub-ambient [46], creating a pressure difference that serves as a mechanism to supply lubricant back into the bearing clearance space. Figure 2.14 provides a pictorial representation of the function of the novel design during the swing phase.

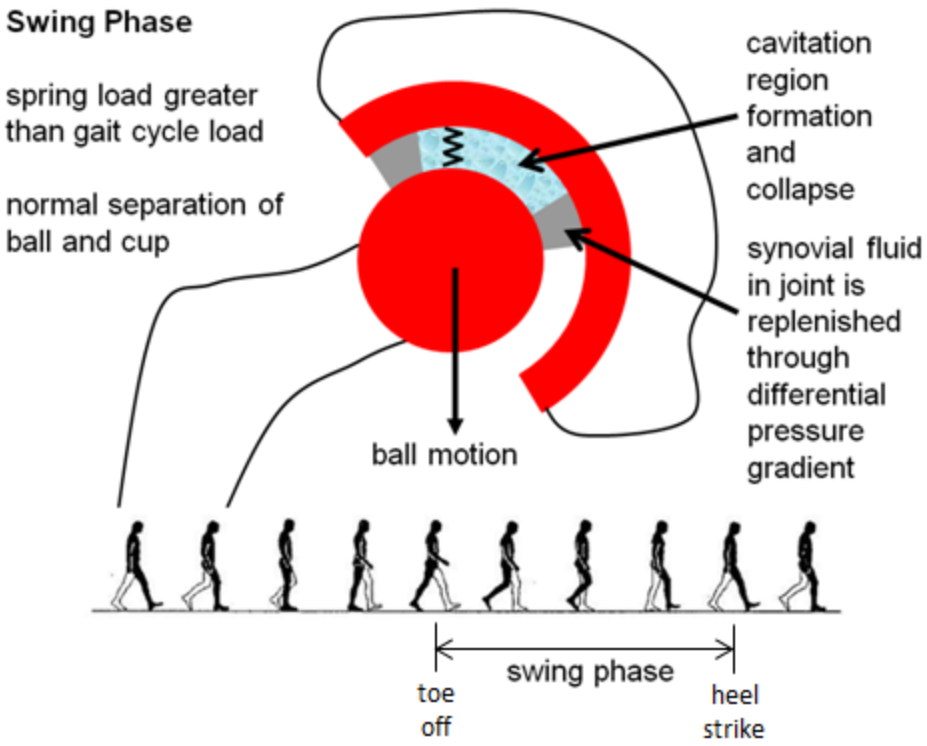

Figure 2.14: Function of the novel THR during the swing phase

Since the novel THR has functionality that is dependent on the external load applied to the implant, gait cycle loading and kinematic conditions are highly important to the design. There are two categories of gait cycle conditions that are commonly applied to lubrication and/or wear analyses: first, gait cycle data taken *in vivo* is often used because it has a realistic source; second, hip simulator gait cycles are often applied because they are easily reproducible in a test environment.

Experimental measurements of gait were pioneered by Bresler and Frankel [39], Rydell [40], and Paul [41] in the 1950s and 60s, typically measuring forces transmitted through the leg to the foot using pressure plates. The most extensive experimental data collection – using instrumented implants fitted with strain gauges – has been completed by Bergmann and his colleagues [21-23, 42, 43], though data collected by Brand *et al.* [44] is also heavily referenced. Experimental gait cycles are difficult to characterize; each gait cycle is unique to a specific patient due to the subject's distinctive muscle strength and location, body weight, and stride, among many other parameters [35]. This is the major issue when applying an experimentally

measured gait cycle to lubrication/wear predictions: the results of the analysis will only hold true for one specific patient.

This shortcoming is exacerbated by the high variability of the loading and kinematic conditions measured from patient to patient and the very small sample size of experimental data. For example, Figure 2.15 displays the loading conditions taken experimentally by Bergmann *et al*. [22] for steady walking in four patients: HSR, IBL, KWR and PFL (NPA shows the average).

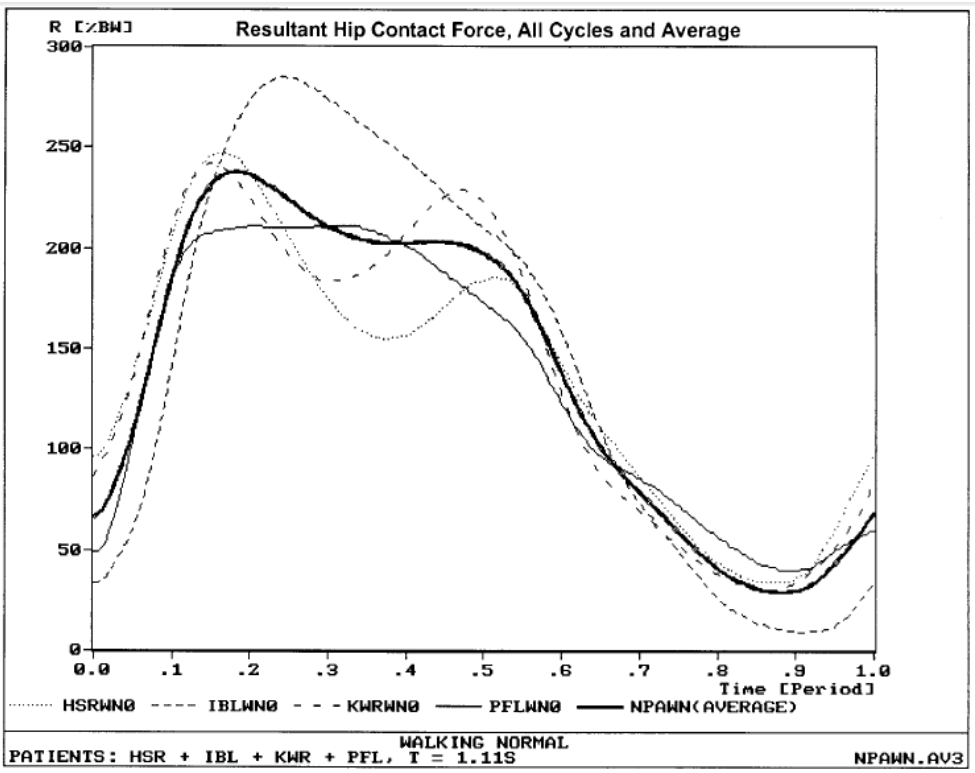

Figure 2.15: Experimental loading conditions from four patients [22]

Note that these 'Resultant Hip Contact Forces' are in terms of body weight. The body weights of these patients range from 702N (KWR) to 980N (PFL), which is a significant range and adds further to the variability seen in Figure 2.14. The general shape is common between each patient (the double-peak in the stance phase), but the magnitudes and timing of the peak loads are highly variable. Furthermore, activities other than walking (such as standing/sitting, walking up/down stairs, and jogging) show even greater ranges for peak loading between individuals [22, 23]. This variability is even more pronounced between studies; Table 2.3 is

taken from Andriacchi and Hurwitz [45] and provides a comparison of experimentally measured peak contact forces in the hip during steady walking.

Peak hip contact forces during walking

Author	Method	Subjects	Post-op (months)	Magnitude (BW)
Paul [10,16]	Reduction	Normal		4.8
	Reduction	Post-op THR	6	2.5–3.5
Crowninshield [26]	Optimization	Normal		5.0
Seireg [12]	Optimization	Normal		5.5
Rydell [18]	Instrumented implant	Post-op THR	6–7	3.0
English [19]	Instrumented implant	Post-op THR	1.5	2.7
Davy/Kotzar [20,24]	Instrumented implant	Post-op THR	1–2	2.7
Bergmann [22,23]	Instrumented implant	Post-op THR	8–33	2.7–4.3
Brand [17]	Instrumented implant	Post-op THR	6	1.8–3.3

Table 2.3: Comparison of peak hip contact forces during walking [45]

The variability in measured loading conditions in the human hip is simply reflective of the complex mechanical nature of the joint of the variability of the human anatomy. The experimental studies cited in this section demonstrate the limitations of applying measured gait cycles to lubrication analyses. In an effort to reduce the variability and uniqueness seen in experimental gait cycles, a number of hip simulator-based gait cycles have been used in recent years that are more generic in shape and magnitude. These gait conditions are developed based on the synthesis of experimental data taken *in vivo*.

Hip simulator gait cycle conditions are commonly applied, especially in lubrication analyses, because they often are more representative of a larger group of patients than data taken *in vivo*. Simulator conditions have become a more popular analysis tool in recent years for both lubrication and wear studies, marking a change from earlier studies which often applied experimental data [35]. Since extensive prototyping and testing is required for a new material combination or design geometry prior to its use by implant companies or surgeons, simulator gait cycles are also becoming more popular due the ability to reproduce these gait conditions in a testing environment.

Hip simulator loading conditions are often characterized by smooth curves that follow a double-peak stance phase (with typical peak loading between 2000N and 3000N) and a constant low-magnitude swing phase load (approximately 300N or lower). Usually, loading is only considered in the vertical (Z) direction or has relatively low-magnitude lateral loading. Figure 2.16 displays the loading conditions used for a number of studies by the Hospital for Special

Surgery (in the cup-stationary configuration). Figure 2.17 displays the loading conditions tied to the ProSim hip simulator used by the Institute of Medical and Biological Engineering at the University of Leeds.

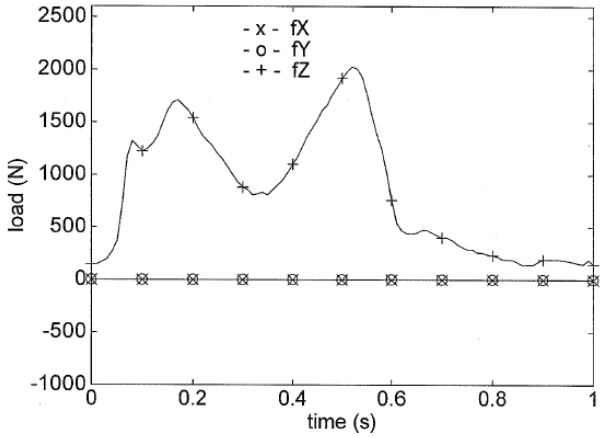

Figure 2.16: Hospital for Special Surgery loading conditions [38]

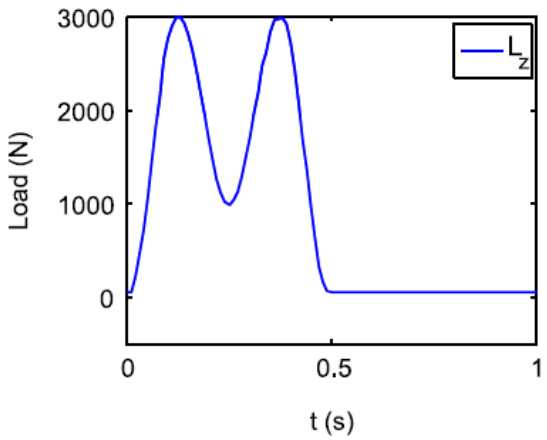

Figure 2.17: Leeds ProSim loading conditions [32, 36, 37]

The kinematic conditions for hip simulator duty cycles are often simplified to only include flexion-extension rotation, which dominates the kinematic behavior of the human hip. This simplifies testing conditions and is an especially common assumption applied to Archard-based wear predictions because it simplifies the sliding-distance calculation considerably. Regardless, simulator kinematics are typically characterized by smooth curves and low angular velocities that correspond to the relatively slow articulation of the hip joint during walking.

Figure 2.18 shows the kinematics for the Hospital for Special Surgery simulator, while Figure 2.19 shows the kinematics used for the Leeds ProSim device.

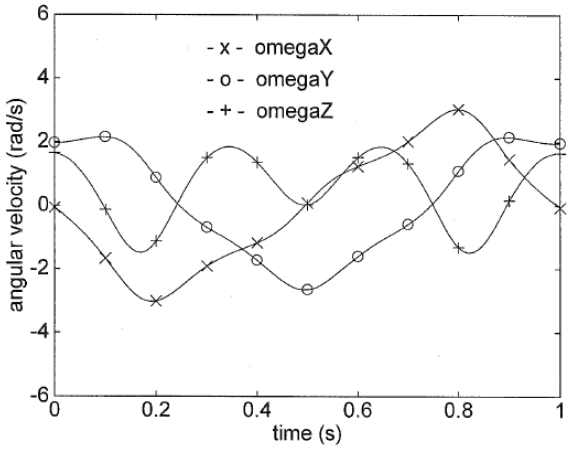

Figure 2.18: Hospital for Special Surgery kinematic conditions [38];

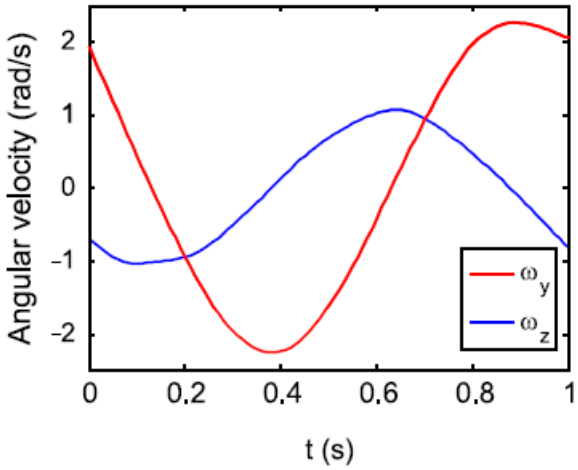

Figure 2.19: Leeds ProSim kinematic conditions [32, 36, 37]

These hip simulator gait cycles, though referenced in multiple studies, are still not representative of every THR patient. In fact, it is impossible to develop a single gait cycle that applies to all patients. Therefore the ISO 14242 standard [20] has been developed. The conditions provided in the standard are used for hip simulator testing of current and novel implant designs and is generally accepted as a reasonable gait cycle for lubrication and wear analyses [19].

Figure 2.20 displays the loading and kinematic conditions specified in the ISO 14242 standard [20]. The gait cycle is characterized by loading only in the vertical (Z) direction with a relatively conservative double-peak stance phase load of 3000N and constant low-magnitude swing phase load of 300N. Only flexion-extension rotation (ω^Y) is considered, which varies between -2 rad/s and +2 rad/s. As is the case with most gait cycles, its period is 1.0 s; the stance phase lasts between 0.0 and ~0.62 s, while the swing phase conditions are applicable between ~0.62 and 1.0 s. The ISO 14242 standard is representative of the 'standard man' with a body weight of 750N (nearly 170 pounds) [20].

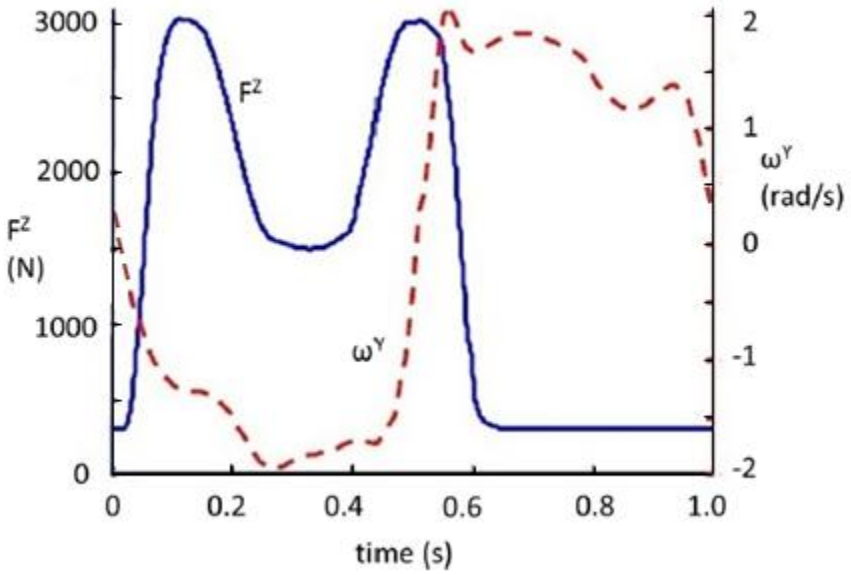

Figure 2.20: ISO 14242 gait cycle [20]

This gait cycle is applied by Boedo and Booker [24, 25] in the lubrication studies for the novel design and is further used in this work to characterize the lubrication behavior of the in-line design orientation and the wear rates associated with the elastic elements. Since this is the generally accepted hip simulator testing duty cycle, the experimental results from any future testing of a prototype for this design can be directly compared with the lubrication and wear analyses.

2.3 Comparison to conventional designs

Conventional hip implants are characterized by wedge-film lubrication, a mechanism that is dependent on the external load and primarily relies on the angular velocity of the articulating surfaces to lubricate the bearing. Since the loading is relatively high and the angular velocities relatively low, this mechanism of lubrication in the implant is often ineffective, leading to high film pressures and low film thicknesses. Moreover, the non-reversing nature of the external load prevents natural separation of ball and cup which further discourages effective lubrication.

The spherical nature of the bearing also limits the effectiveness of the implant. Due to the unidirectional nature of loading and spherical geometry, a small 'point contact' region of the lubricant film is responsible for carrying the external load. The lubricant film in this load-carrying region may 'squeeze out' and lead to direct contact between the bearing surfaces that inevitably is the cause of wear in the THR. The nature of the design of conventional implants is simply not inclined to effective lubrication.

Transient hydrodynamic lubrication studies completed by Goenka [47], Kothari *et al.* [48], and Jin and Dowson [49] incorporated realistic gait cycle conditions and assumed rigid ball and cup surfaces. These studies investigated nonspherical bearing geometries (*ie.* dimples, ellipsoidal geometries) in addition to the conventional spherical cases and found that improvements in bearing performance were observed for these 'irregular' bearing surfaces, though unrealistically large lubricant viscosities and unrealistically small clearance specifications were used. Additionally, elastic deformations on the order of film thickness were predicted by Jin and Dowson when the predicted pressure distributions were applied to an elastic model of the cup.

Transient elastohydrodynamic (EHD) studies completed by Wang and Jin [11, 50], Wang *et al.* [12], and Meng *et al.* [13] further investigated nonspherical bearing surfaces employing structural elasticity appropriate for MOM bearings. Furthermore, these studies incorporated realistic gait cycle conditions, clearance specifications, and lubricant viscosities. These studies found that ellipsoidal cup geometries improved bearing performance, leading to lower film pressures and higher film thicknesses than for conventional spherical implants. Specifically, film thicknesses in the range of 10-40nm and film pressures in the range of 55-65MPa were predicted for conventional spherical geometries. For nonspherical geometries, somewhat improved film

thicknesses in the range of 40-60nm and film pressures in the range of 45-55MPa were predicted. These results confirm the need for an EHD formulation for MOM implants and further suggest a mixed-lubrication regime in these bearings.

Neglected in these lubrication studies are protein layers observed by Fan *et al.* [51] that accumulate on the articulating bearing surfaces. Protein aggregation and deposition cause complex film formation mechanisms in solutions containing synovial fluid (the natural lubricant in the hip joint). These films have been measured in the range of 20-100nm [51, 52]. The effect of these protein films (which are on the order of predicted film thickness in conventional implants) on lubrication *in vivo* are not well-understood.

It is now appropriate to briefly discuss the design specifications used to describe and to assemble conventional hip implants. Spherical implants are typically MOP or MOM in nature, consisting of a (metal) spherical ball and a (metal or plastic) spherical cup with a nominal radial clearance between the bearing surfaces. The typical MOP implant size is between an 11mm and 16mm cup radius, while the MOM implant size is approximately a 25mm cup radius. Artificial hip joints used in practice are, however, evolving towards the use of larger radius implants (greater than 18mm radius), which more closely resembles the size of the natural hip joint (approximately 25mm radius) [19]. Nominal radial clearance values typically range between 30μm (MOM) and 150μm (MOP) [19].

Many implant designs (especially MOP) employ a metal backing that is fastened to the pelvis through a cementing process or by mechanical fasteners. The cup 'insert' is bonded to the backing and is often a softer material such as UHWMPE in MOP designs. Another key parameter that is related to wear is the orientation of the cup assembly. This variable is chosen by the surgeon to allow for the greatest range of motion for the artificial joint and varies significantly among patients due to pelvis size, muscle strength and location in the joint region, and femur geometry. For lubrication predictions, the inclination angle is typically set to 45° and the anteversion angle is typically set to 0°.

Figure 2.21 shows the conventional implant design analyzed in this work for comparison purposes. This FE model is identical to the model used by Maxian *et al.* [30]. The X_C, Y_C and Z_C axes correspond to the X, Y, and Z coordinate frame given by Boedo and Booker [24]; likewise, the X_C', Y_C' and Z_C' axes are oriented identically to the X', Y', and Z' coordinate axes, where Z_C' is oriented along the polar axis of the cup assembly. The polyethylene cup is assumed to be

bonded to the metal backing, while the outside area of the metal backing is assumed to be fixed. A cup inclination angle of 45° and anteversion angle of 0° are chosen, consistent with Maxian *et al.* [30]. The effect of radial clearance on wear has been reported to be negligible when less than 200μm [33]; therefore a clearance of 40μm is chosen for this work which corresponds to the more promising lubrication results in the novel design [24, 25]. A 25mm radius cup geometry is also analyzed as a comparator for the novel design of that size, though there are no comparable wear results in literature for this particular geometry for validation purposes.

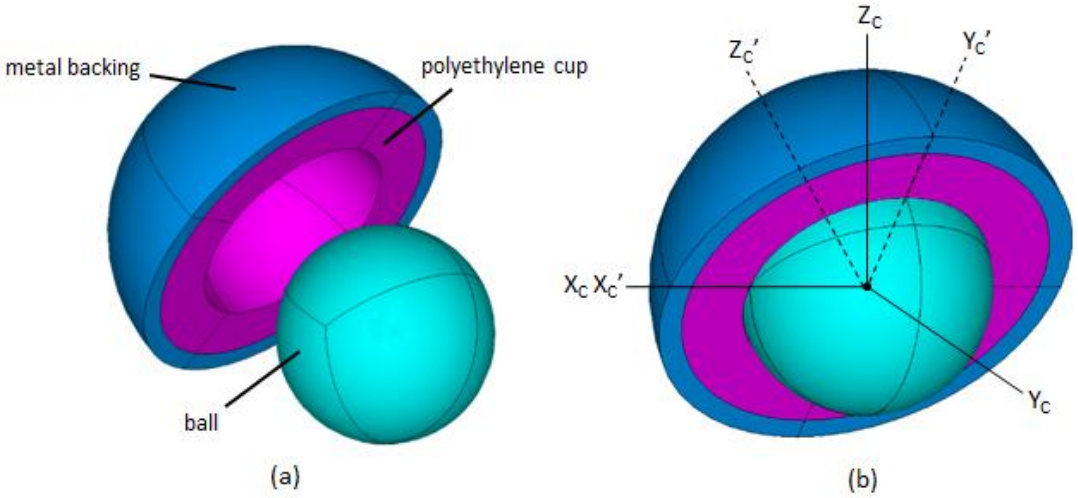

Figure 2.21: Conventional design FE model

Table 2.4 lists the critical dimensions for the conventional models. Note that the thickness of both the polyethylene insert and the metal backing are constant between the 16mm and 25mm radius implant models. Validation of the mesh densities applied to the conventional models can be found in Appendix A.

Parameter	t_{UHMWPE}	$t_{backing}$	**C**	$E_{ball/backing}$	$\nu_{ball/backing}$	E_{UHMWPE}	ν_{UHMWPE}
Units	mm	mm	μm	GPa	-	GPa	-
Value	8	3	40	210	0.31	1.4	0.46

Table 2.4: Design parameters for conventional models

In addition to the MOP model, this design is also simulated with a cobalt-chrome cup insert instead of a polyethylene material. The geometric parameters for the model remain the

same as for the MOP case; however, the material of the cup insert has an elastic modulus of 210 GPa and a Poisson's ratio of 0.31. The MOM models are required for comparison with the coated novel designs discussed in Section 2.1.

Chapter 3: Lubrication Analysis – Stance Phase

3.1 Modeling assumptions

The majority of what follows is taken from Boedo and Booker [24] and is included here for completeness. The assumptions associated with the stance phase lubrication analysis are important to reiterate due to their effects on the fluid-film behavior within the bearing.

The lubrication analysis for the stance phase employs a mass-conserving FE cavitation algorithm developed by Kumar and Booker [53], Boedo and Booker [54] and Booker and Boedo [55], where components of ball eccentricity $\boldsymbol{e}$ and nodal density $\{\rho\}$ are state variables. The bearing surfaces of the implant are assumed to be rigid. Ball motion and fluid film evolution are governed by the following state rate relations:

$$\frac{d\boldsymbol{e}}{dt} = \boldsymbol{f}(\boldsymbol{e}, \{\rho\}, t) \tag{3.1}$$

$$\frac{d\{\rho\}}{dt} = \{g\}(\boldsymbol{e}, \{\rho\}, t) \tag{3.2}$$

with the initial state:

$$\boldsymbol{e}(t_0) = \boldsymbol{e}_0 \tag{3.3}$$

$$\{\rho(t_0)\} = \{\rho_0\} \tag{3.4}$$

and the state rate relations incorporate the quasistatic force balance:

$$\boldsymbol{F}_{film} = \boldsymbol{F}(t) - \boldsymbol{F}_{elast}(\boldsymbol{e}) \tag{3.5}$$

where $\boldsymbol{F}_{film}$ and $\boldsymbol{F}_{elast}$ are film load and elastic load vectors, respectively, transmitted from ball to cup. Elastic load components in the X and Y directions are assumed to the negligibly small.

The ISO 14242 loading and kinematic conditions are applied to the lubrication studies. The stance phase starts when $F^Z - F^Z{}_{elast} > 0$ at $t_0 = 0.03s$, where F^Z is the external vertical load applied to the ball defined by the ISO 14242 standard [20]. It is further assumed that the ball is in a centered condition at the origin in the bearing at the start of the stance phase and that full reformation of the fluid film occurs during the swing phase (which is predicted analytically in

Chapter 3). The stance phase ends when $F^Z - {F^Z}_{elast} < 0$ at $t = 0.63s$. The results in Section 3.2 employ an implicit variable-step numerical integration routine, while the results associated with the novel in-line design employ an explicit numerical routine. Validation of the explicit routine against the implicit routine is provided in Appendix B of this thesis.

As stated in Chapter 2, the FE mesh used to represent the lubricant film is composed of a planar set of contiguous three-noded elements (two-dimensional) that are connected at a discrete set of nodes. Triangularly-shaped elements offer greater flexibility from a modeling perspective (especially considering the irregular geometries associated with this work) and avoid numerical issues associated with spherical coordinates. Further information regarding the formulation and validation of this meshing methodology is provided in Boedo and Booker [24].

The results displayed in this thesis are representative of only the 16mm cup geometry. Ambient (zero gauge) pressure and lubricant density (in this case, 850 kg/m^3) conditions are prescribed to the nodes located on the mesh boundary. The lubricant (periprosthetic synovial fluid) is assumed to have isoviscous qualities and is prescribed a viscosity value of 2.5 mPa-s, which is representative of the high shear rates encountered during walking [19, 24]. The cavitation algorithm requires the specification of a cavitation threshold parameter; it is set in this work at 0 gauge pressure, though essentially identical results are obtained using a value at the generally-accepted lower bound of -101 kPa. The piezoviscous behavior of perisynovial fluid is assumed to be negligible at the film pressures found in the hip joint [19]. Furthermore, the inclination angle of the acetabular cup is set at 45°.

3.2 Dimensional results – lateral design configuration

The results presented in this section are taken directly from Boedo and Booker [24]. Figure 3.1 shows the progression of minimum film thickness h_{min} and maximum film pressure p_{max} over the stance phase for the 16mm geometry. A nominal radial clearance C_0 of 30μm is used to analyze three ellipticity values: $\delta =$ 30μm, 40μm, and 50μm.

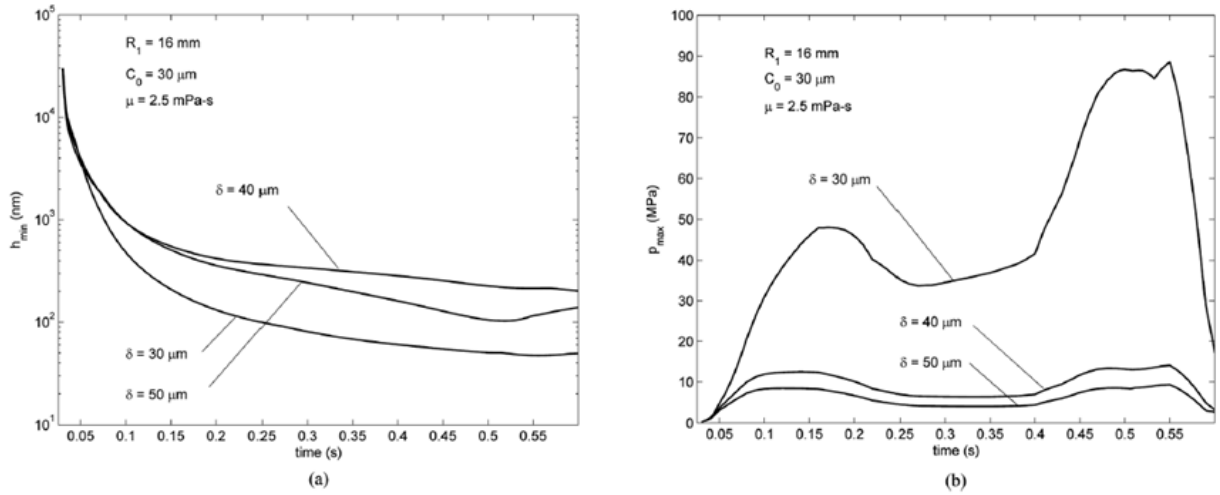

Figure 3.1: Effect of ellipticity on time histories of minimum film thickness and maximum film pressure [24]

The minimum film thickness values for $\delta > C_0$ fall well within the full-film lubrication regime for MOM and COC implants. Maximum film pressures are much smaller than those predicted in EHD studies and this strongly suggests that rigid cup surface assumptions are justifiable to these studies. Figure 3.2 shows spatial distributions of film pressure at $t = 0.5s$ for the three ellipticity cases analyzed in Figure 3.1.

For ellipticity values $\delta > C_0$, the ball and cup surfaces approach circular line contact, resulting in substantially redistributed pressures that are reduced to a nearly uniform value over the polar region of the cup when compared with conventional spherical designs.

Figure 3.3 displays extrema values of minimum film thickness and maximum film pressure over a wider range of nominal radial clearances and ellipticity values. The selected parameter values fall within current manufacturing ranges for MOM implants.

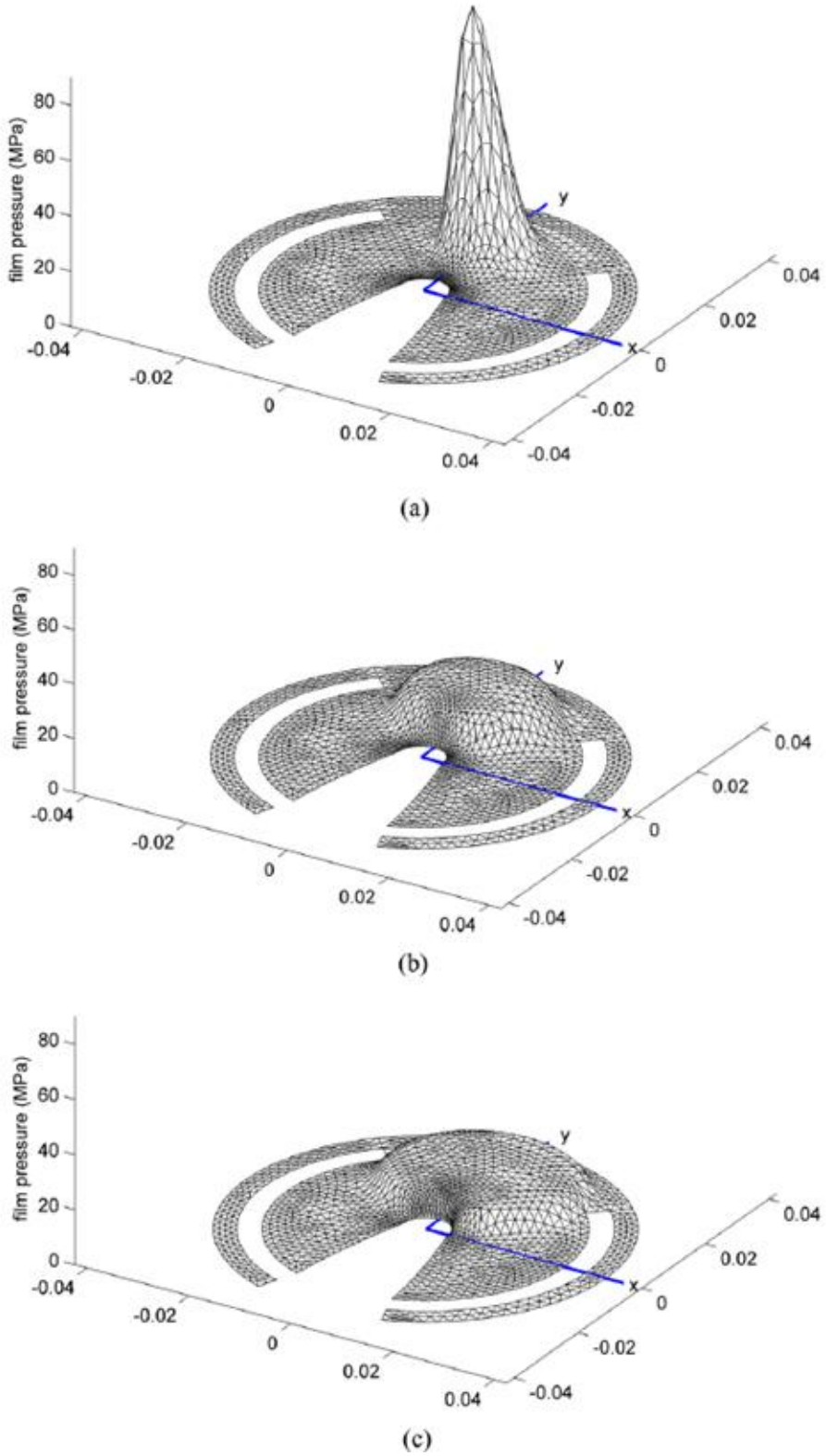

Figure 3.2: Pressure distributions at $t = 0.5s$; (a) $\delta = 30\mu m$, (b) $\delta = 40\mu m$, (c) $\delta = 50\mu m$ [24]

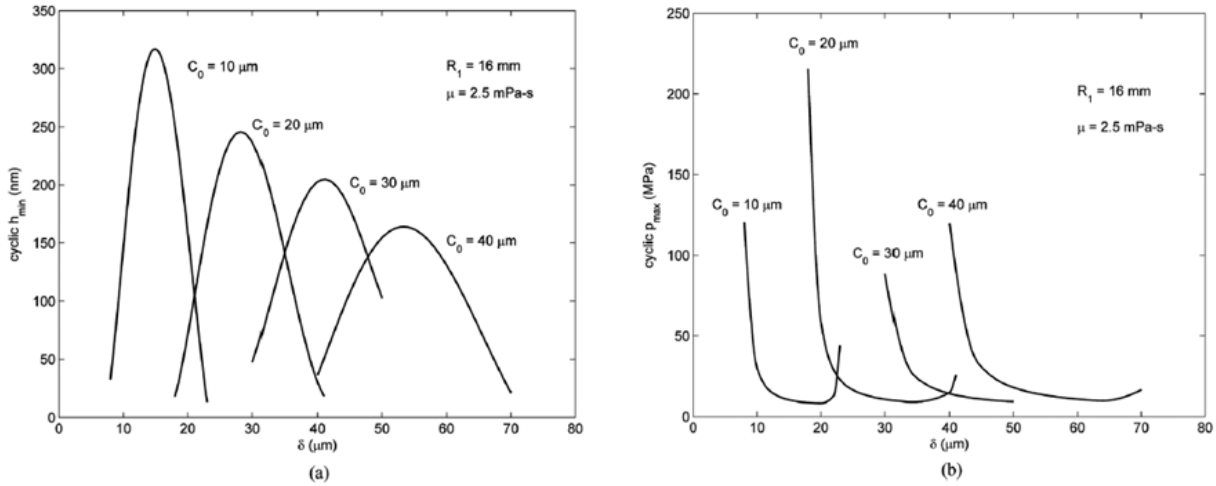

Figure 3.3: Effect of ellipticity on bearing performance [24]

The observed flatness of the curves indicates that large ellipticity variations from the optimal value can be tolerated, making manufacturing issues more manageable. As is the case with Figures 3.1 and 3.2, the results for this study show that optimal ellipticity values are consistently greater than the selected nominal clearance. This supports a line contact approach to the design of spheroidal bearings under the conditions seen in the human hip.

In addition to the results presented by Boedo and Booker [24], an additional study is simulated in this work relating to the kinematics associated with the gait cycle. By employing a design which promotes squeeze-film action over wedge-film action, it is expected that the kinematics (rotation) of the ball have a less pronounced effect on the lubrication of the bearing in the novel configuration. Figure 3.4 shows the comparison of minimum film thickness with the full ISO standard loading and kinematic conditions used for the results elsewhere in this section and the ISO standard without any rotational kinematics of the ball. The figure displays the progression of minimum film thickness h_{min} and maximum film pressure p_{max} over the stance phase for the 16mm geometry. A nominal radial clearance C_0 of 30μm is used to analyze three ellipticity values: $\delta = 30$μm, 40μm, and 50μm.

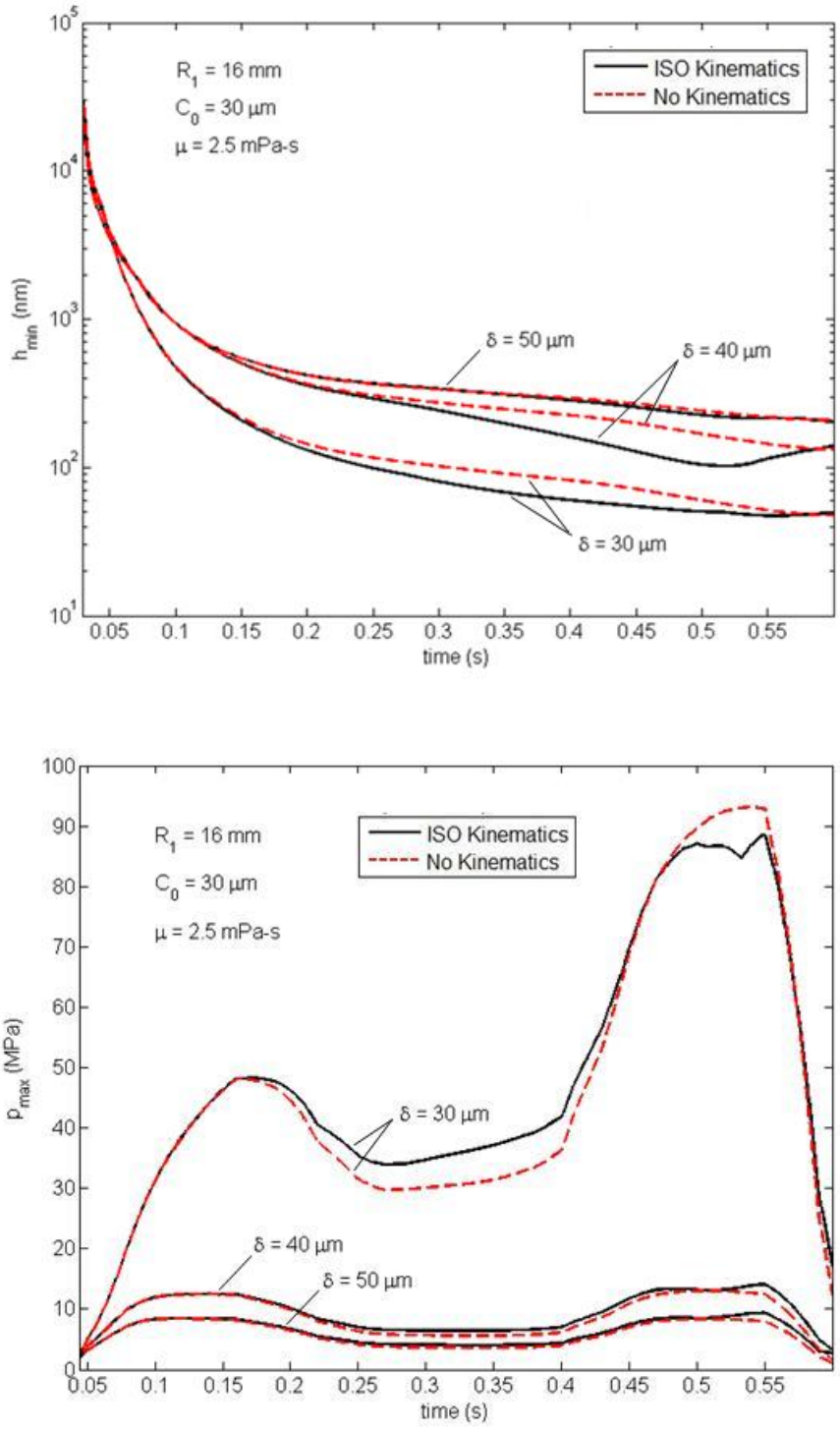

Figure 3.4: Comparison of results simulated with and without ISO 14242 rotational kinematics

The results show that simulating the novel design without rotational kinematics gives very similar results to the simulations employing the ISO 14242 kinematics. The shape of the minimum film thickness curves show the greatest deviations between 0.25 and 0.50s of the stance phase but converge to nearly the same value at the completion of the stance phase. These results show that the kinematics used during simulation for the novel design employing an elastic load and elliptical cup surface negligibly affect the evolution of minimum film thickness and minimum film pressure over the stance phase of the gait cycle.

A more comprehensive study associated with the lateral design configuration is given by Boedo and Booker [24] including the effects of the radial slot, viscosity values and initial conditions. These results are presented in this thesis for comparison with the lubrication analysis of the in-line design configuration (Section 3.3).

3.3 Dimensional results – in-line design configuration

The results presented in this section are representative of the in-line configuration and use the fluid-film meshes shown in Section 2.1.2. The assumptions and methodology for this analysis are identical to the ones applied to the lateral design provided by Boedo and Booker [24], with the following exceptions: (1) an explicit variable-step numerical integration routine is used as opposed to the more computationally expensive implicit integrator; (2) a time step of 0.0005s (0.0002s is used by Boedo and Booker [24]) is used for the in-line configuration; and (3) the boundary conditions are varied in this analysis due to the geometry. Validation of these modeling assumptions are provided in Appendix B.

For the lateral design simulations, ambient (zero gauge) pressure is applied to the boundary nodes. For the in-line configuration, the boundary nodes located on the edges are still prescribed an ambient pressure value, but the boundary conditions on nodes associated with the clearance hole located at the polar axis of the cup are varied. The first set of results in this section prescribe ambient pressure to these nodes which simulates unrestricted flow of lubricant through the clearance hole. Since the size of the clearance hole for this design is equivalent to the largest elastic column diameter simulated (4mm), a boundary condition that prescribes zero flow in/out of the hole at these nodes is also simulated. This is representative of a perfectly sealed boundary between the rigid cup and the elastic element.

Figure 3.5 shows the evolution of minimum film thickness h_{min} and maximum film pressure p_{max} over the stance phase for the 16mm geometry simulating unrestricted flow at the boundary nodes of the clearance hole. Similarly to the lateral design simulations, a constant nominal radial clearance C_0 of 30μm is used to analyze three ellipticity values: $\delta = 30$μm, 40μm, and 50μm.

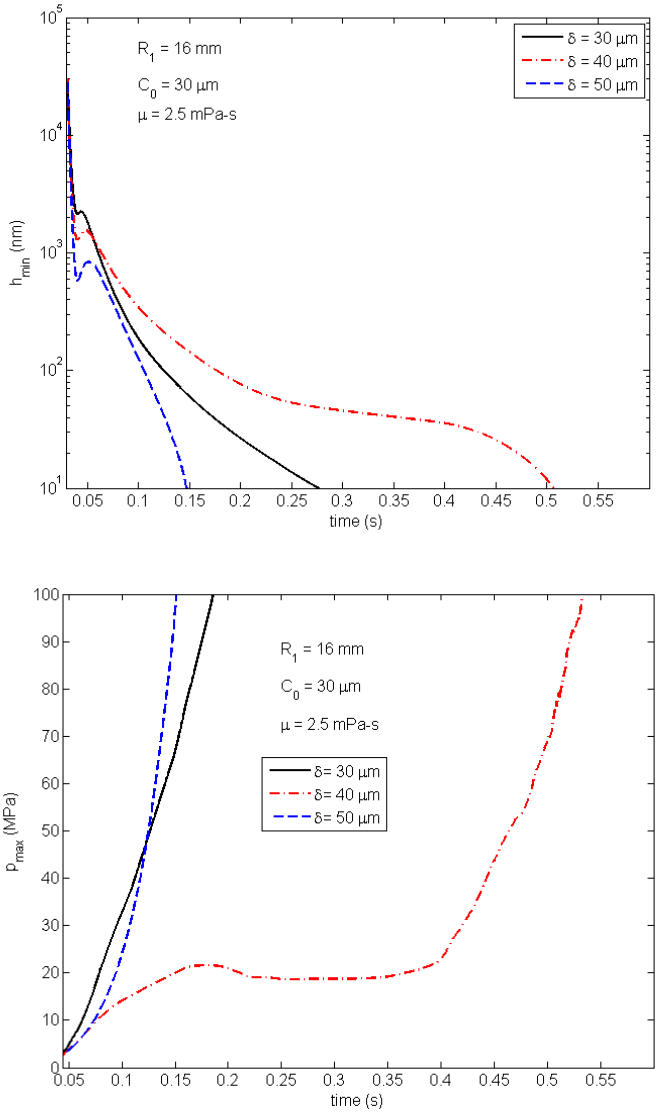

Figure 3.5: Effect of ellipticity on time histories of minimum film thickness and maximum film pressure, unrestricted flow through clearance hole

The results for this boundary condition are expectedly poor; the location of the clearance hole is in the center of the region of the lubricant film that carries the majority of the transmitted load. Since flow is unrestricted in this region, the film squeezes out and leads quickly to the approach of zero minimum film thickness prior to the end of the stance phase. The associated maximum film pressure in this region increases towards infinity, as a quickly shrinking film region is carrying the entire transmitted load. Due to the poor lubrication results for this boundary condition, further study of ellipticity and clearance effects are not pursued.

Figure 3.6 displays the same analysis for the case in which flow is completely restricted (sealed) at the boundary nodes of the clearance hole.

Since the lubricant is effectively sealed in the region of the clearance hole in this case, the lubrication results are considerably better. When compared with the results for the lateral design, the film thickness at the end of the stance phase is comparable, though the minor oscillation at ~0.05s is unique to the in-line simulations. The film pressure curves are comparable in both shape and magnitude for the two novel design configurations.

Figure 3.7 shows spatial distributions of film pressure at $t = 0.5s$ for the three ellipticity cases analyzed in Figure 3.5.

Figure 3.8 displays extrema values of minimum film thickness and maximum film pressure over a similar range of nominal radial clearances and ellipticity values applied to the lateral design configuration. The selected parameter values fall within current manufacturing ranges for MOM implants.

Both the cyclic minimum film thickness and cyclic maximum film pressure curves are similar in shape and magnitude to those simulated for the lateral design configuration. Optimal ellipticity values are consistently greater than the associated nominal clearance. The ellipticity ranges that provide optimal results are smaller for the tighter clearances ($C_0 = 10\mu m$, $20\mu m$) and comparable for the larger clearances ($C_0 = 30\mu m$, $40\mu m$) compared with the lateral design results.

Assuming completely restricted flow through the clearance hole, the in-line results show agreement with the predictions found by Boedo and Booker [24] for the lateral novel design. The results for the unrestricted flow case show that the bearing will squeeze out, as the clearance hole is located in the center of the load-carrying region of the film. The clearance hole should

therefore be nominally the same size as the elastic element or slightly smaller (press-fit) to ensure a sealed boundary around the edge of the clearance hole.

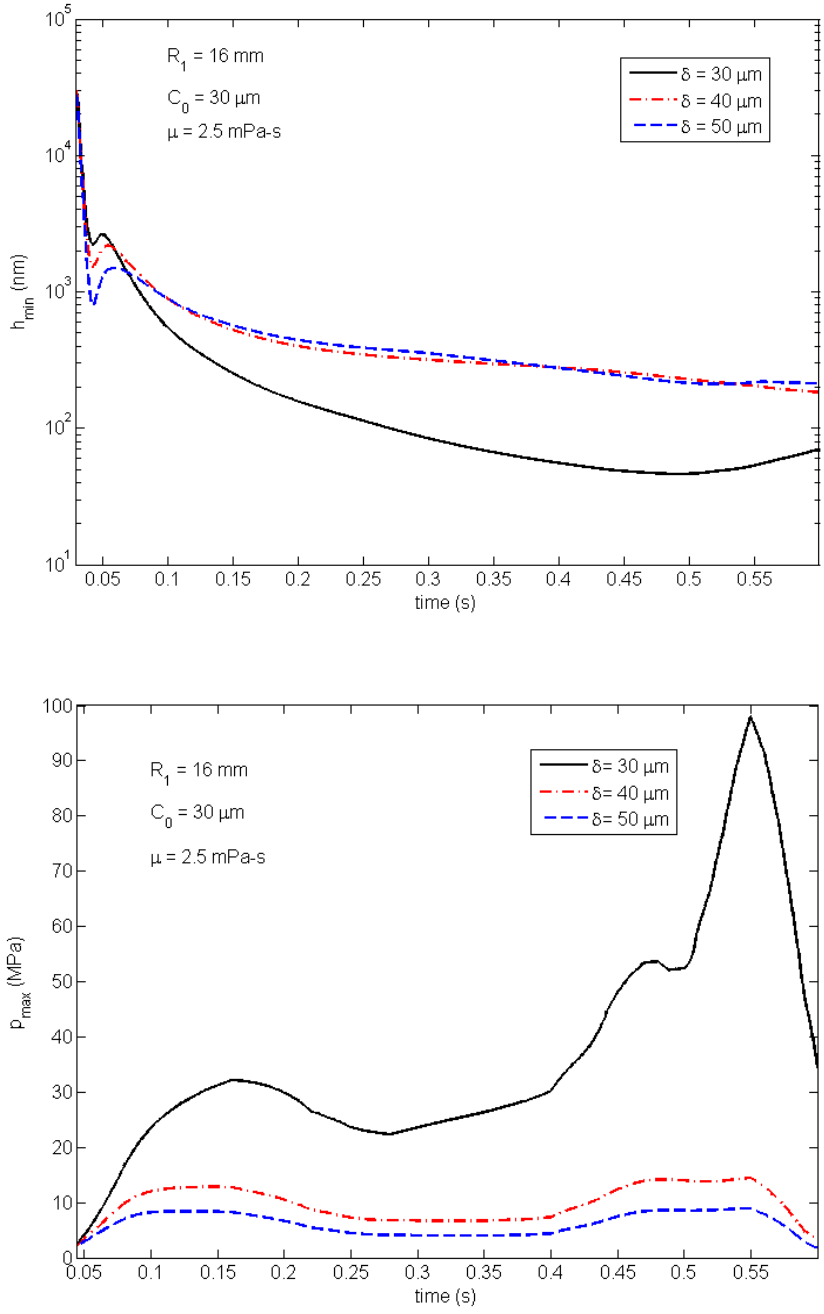

Figure 3.6: Effect of ellipticity on time histories of minimum film thickness and maximum film pressure, completely restricted flow through clearance hole

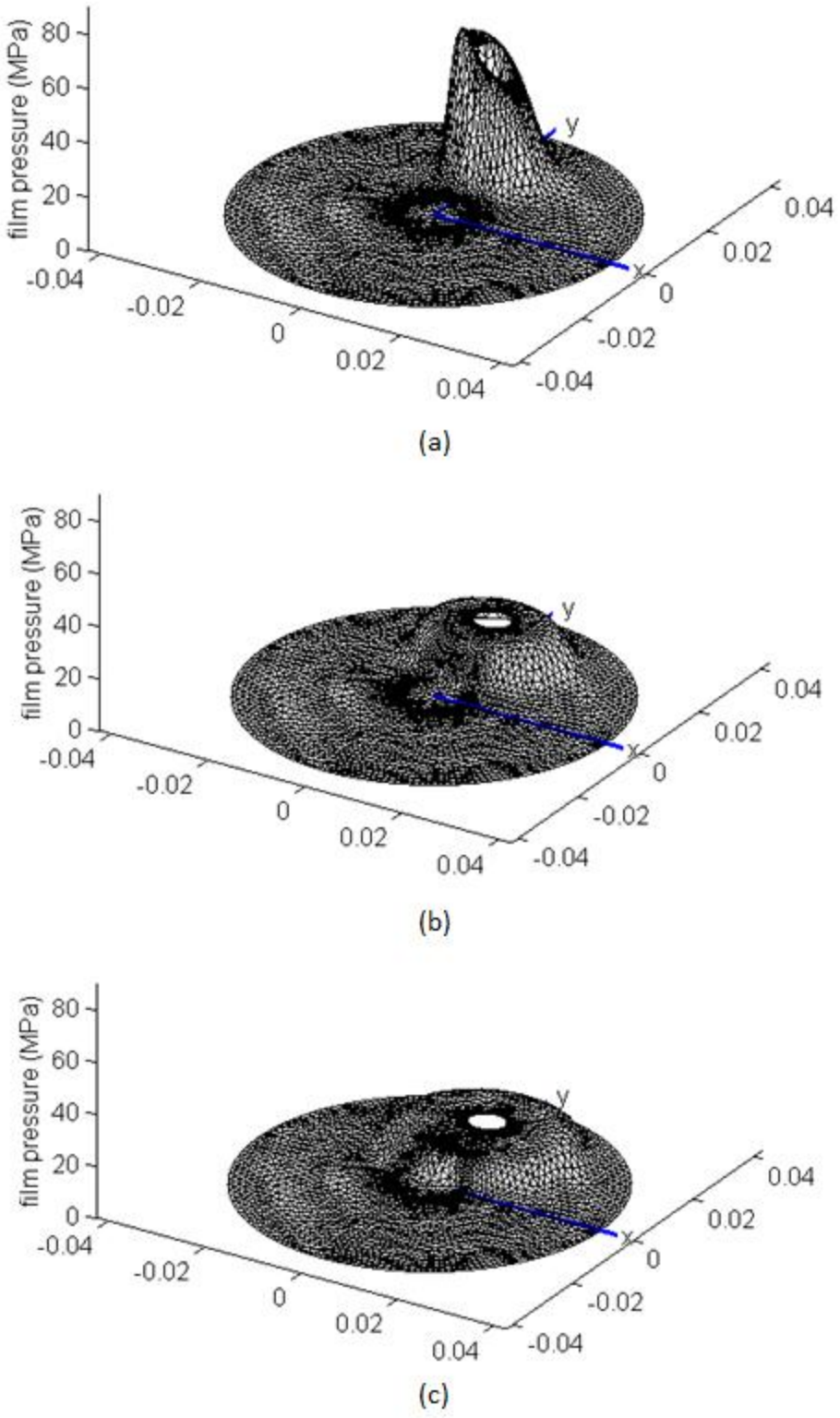

Figure 3.7: Pressure distributions at $t = 0.5s$, completely restricted flow through clearance hole; (a) $\delta = 30\mu m$, (b) $\delta = 40\mu m$, (c) $\delta = 50\mu m$

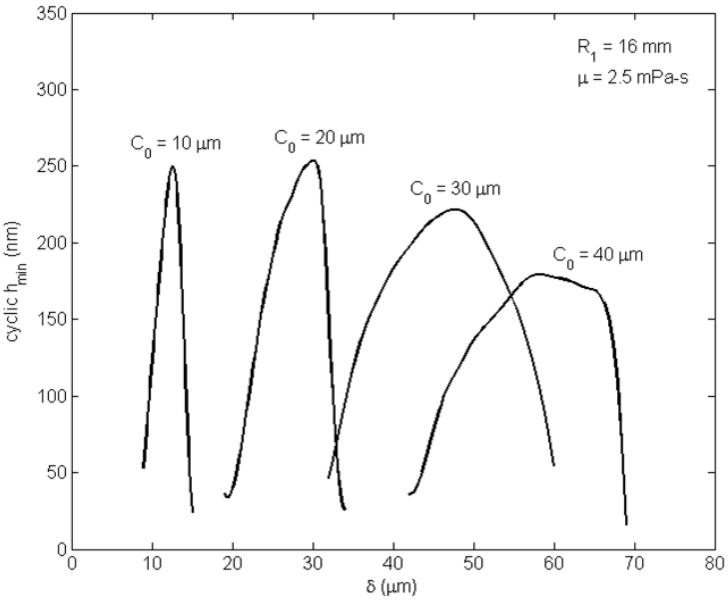

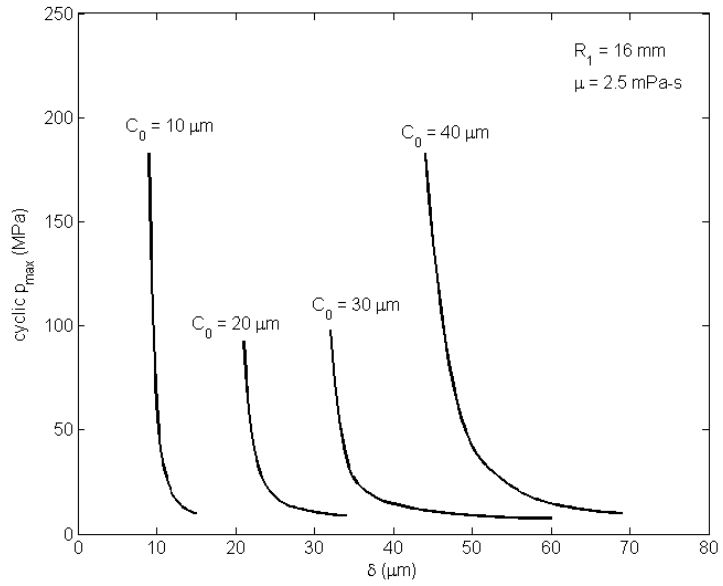

Figure 3.8: Effect of ellipticity on bearing performance, completely restricted flow through clearance hole

Chapter 4: Lubrication Analysis – Swing Phase

4.1 Modeling assumptions

The following section is largely taken from Boedo *et al.* [25] and is included here for completeness. The assumptions associated with the swing phase analysis are specific to this analysis and differ somewhat from the assumptions listed in Chapter 3.

The swing phase analysis applies a similar mass-conserving FE cavitation algorithm to the stance phase analysis. An opposite approach is taken, however, to simulate the swing phase cases; the ball kinematics are prescribed (that is, the eccentricity and velocity components) in order to evaluate the dynamics of cavitation formation and fluid-film reformation. The nodal pressures and net force on the ball are the outputs for this lubrication algorithm.

Applying the ISO 14242 gait conditions (including angular velocity of the ball), the swing phase is defined as the period of time in which $F^Z - F^Z{}_{elast} < 0$, where F^Z is the external vertical load applied to the ball and $F^Z{}_{elast}$ is the reaction force due to the elastic elements (set at 350N). The swing phase begins at 0.63s and ends at the start of the next gait cycle at 1.03s and is characterized by a constant, low-magnitude load of 300N upwards in the vertical (Z) direction. The implant geometries and FE meshes are identical to those simulated for the stance phase in Chapter 3.

Under conditions of normal separation, the motion of the ball along the vertical (Z) axis is given by:

$$e^X(t) = 0 \tag{4.1}$$

$$e^Y(t) = 0 \tag{4.2}$$

$$e^Z(t) = e_s + v(t - t_s) \tag{4.3}$$

$$\frac{de^X}{dt} = 0 \tag{4.4}$$

$$\frac{de^Y}{dt} = 0 \tag{4.5}$$

$$\frac{de^Z}{dt} = v \tag{4.6}$$

where e^X, e^Y and e^Z are the components of eccentricity of the ball and de^X/dt, de^Y/dt and de^Z/dt are the associated components of rate of change of eccentricity (velocity); e_s is the position of the ball at the start of the swing phase ($t = t_s$); and v is the prescribed constant ball linear velocity. Note that the motion is only prescribed in the direction of external load.

For ellipticity values δ that are greater than or equal to the nominal radial clearance C_0 and a specified initial minimum film thickness h_s, the initial position of the ball is given by:

$$e_s = 2(\delta/C_0)^{1/2}(1 - h_s/C_0)^{1/2} \tag{4.7}$$

At a given time t, the ball kinematics are now prescribed. The lubrication algorithm therefore finds the set of nodal density rates $d\{\rho\}/dt$ that satisfies

$$d\{\rho\}/dt = g(\{\rho\}, \boldsymbol{e}, d\boldsymbol{e}/dt\,, t) \tag{4.8}$$

with initial state

$$\{\rho(t = t_s)\} = \{\rho\}_0 \tag{4.9}$$

Similarly to the stance phase simulations, ambient (zero gauge) pressure and lubricant density (in this case, 850 kg/m^3) conditions are prescribed to the nodes located on the mesh boundary. The lubricant is assumed to have isoviscous qualities and a prescribed viscosity of 2.5 mPa-s. The cavitation threshold value p_{cav} is considerably more important during the swing phase and is specified as the generally-accepted lower bound of -101kPa for the basic studies. The inclination angle of the acetabular cup is set at 45°, and the results displayed in this section are representative of only the 16mm cup geometry.

It should be noted that ball velocity v is set to a reference value $v_0 = -C_0/T$, where T is the duration of the swing phase (0.4s). The prescribed velocity is an important parameter during the swing phase and is discussed in further detail in Section 4.2.

4.2 Dimensional results – lateral design configuration

The purpose of the swing phase lubrication analysis is to investigate the formation of the cavitation region within the implant during normal separate of ball and cup and its subsequent collapse (or 'refilling'). Complete collapse of the cavitation region is required before the end of the swing phase so that a full lubricant film is available between ball and cup for the relatively high loading during the stance phase. Figure 4.1 shows time sequence of spatial film pressure distributions for the case: C_0 = 30μm, δ = 40μm, h_s = 50nm, and p_{cav} = -101kPa. Ball velocity is prescribed as $v = v_0$ for this simulation.

A large cavitation region immediately forms over the load-carrying region of the film at the start of the swing phase (t = 0.63s). Reformation of the complete lubricant film occurs at t = 0.873s, or t_r = 0.243s. For this particular geometry, reformation of the film occurs before the start of the stance phase. Complete reformation is indicated by film pressures which are everywhere greater than p_{cav}.

Figure 4.2 investigates the effect of cavitation threshold pressure on the refill time t_r over the range of ellipticity values simulated in the stance phase portion of this research [24]. The cavitation threshold pressure p_{cav} ranges from the lower bound of -101kPa to -35kPa in this study.

Refill time is relatively insensitive to changes in ellipticity but is strongly dependent on the prescribed cavitation threshold pressure. Figure 4.3 investigates effect of ball velocity on refill time at two cavitation threshold pressures that span the range of possible p_{cav} values found in practice. Note that velocity is represented as a ratio of the prescribed velocity v over the reference velocity v_0. The ellipticity is held constant at δ = 40μm.

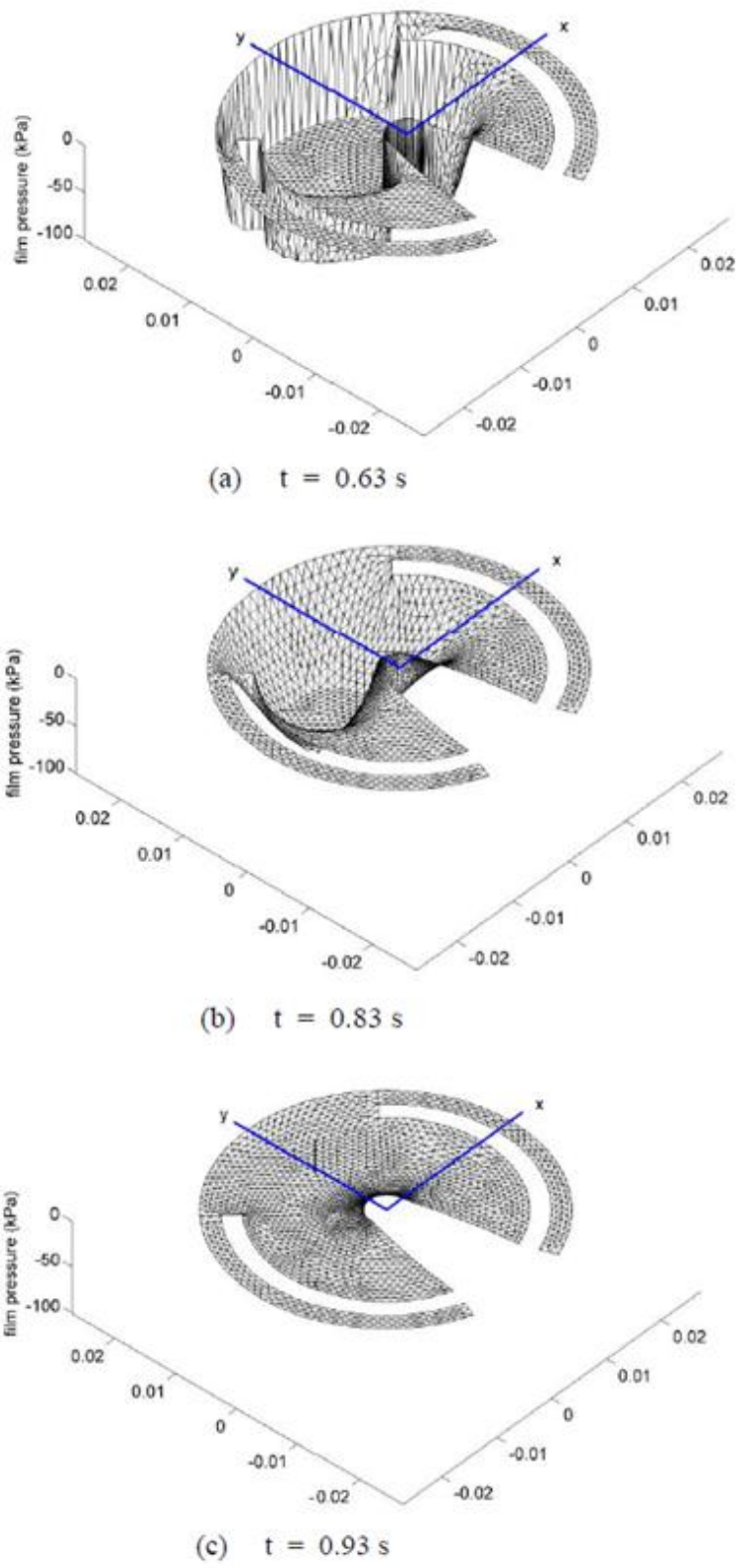

Figure 4.1: Swing phase pressure distributions: R_1 = 16mm, μ = 2.5 mPa-s, $v = v_0$ [25]

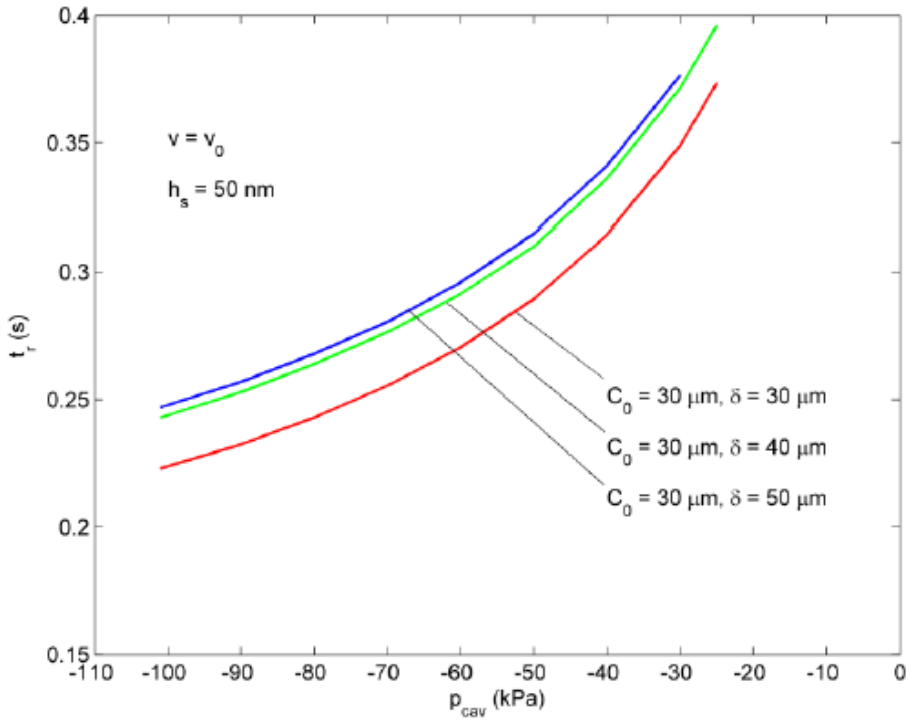

Figure 4.2: Effect of cavitation threshold pressure on refill time: R_1 = 16mm, μ = 2.5 mPa-s [25]

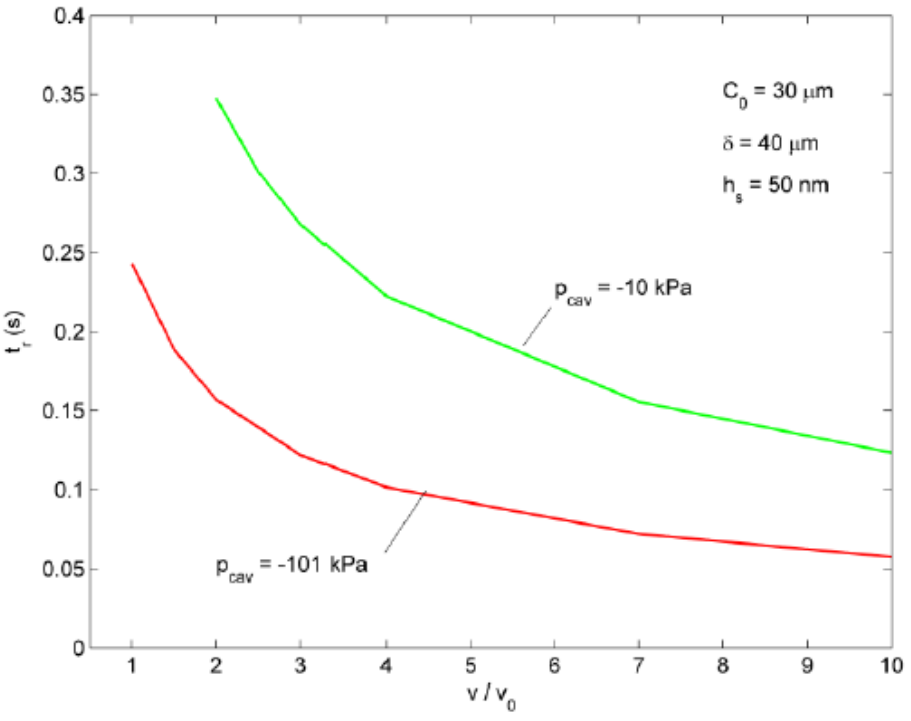

Figure 4.3: Effect of ball velocity on refill time: R_1 = 16mm, μ = 2.5 mPa-s [25]

Refill time is strongly dependent on ball velocity during the swing phase. It is interesting to note that full-film reformation can occur at near-ambient cavitation threshold pressures (specifically -10kPa) with minor increases in ball velocity over the reference velocity.

The results presented in Boedo *et al.* [25] show that the reformation of a complete lubricant film during the swing phase is possible for the lateral novel design configuration over a significantly large range of linear ball velocities, cavitation pressures, and initial ball positions that are likely to be encountered in practice. Furthermore, these results show that ellipticity is of lesser importance during the swing phase than during the stance phase.

4.3 Dimensional results – in-line design configuration

The results presented in this section are representative of the in-line configuration and use the fluid-film meshes shown in Section 2.1.2. The validation of the fluid-film mesh is provided in Appendix B. The assumptions and methodology for this analysis are identical to the ones applied to the lateral design provided by Boedo and Booker [25], with the single exception that the boundary pressures are varied.

Similar to the stance phase simulation of the in-line design, two cases of boundary conditions are prescribed: (1) unrestricted flow, where the pressure at each node on the boundary of the clearance hole is set to zero, and (2) completely restricted flow (sealed boundary), where the flow at each node on the boundary of the clearance hole is set to zero. The unrestricted flow case is presented first; due to the poor lubrication results for the stance phase simulation of this condition, only the evolution of spatial film pressure is shown.

Figure 4.4 shows a time sequence of spatial film pressure distributions for the same case simulated in Figure 4.1 (that is, $v = v_0$, C_0 = 30μm, δ = 40μm, h_s = 50nm, and p_{cav} = -101kPa).

Complete reformation of the lubricant film occurs at t = 0.829s, or t_r = 0.199s. This refill time is shorter than for the lateral design and can be attributed to the boundary condition of zero ambient pressure at the edge of the clearance hole. This condition allows for unrestricted flow through the clearance hole which therefore permits lubricant to refill the cavitation region (located directly surrounding the clearance) more quickly.

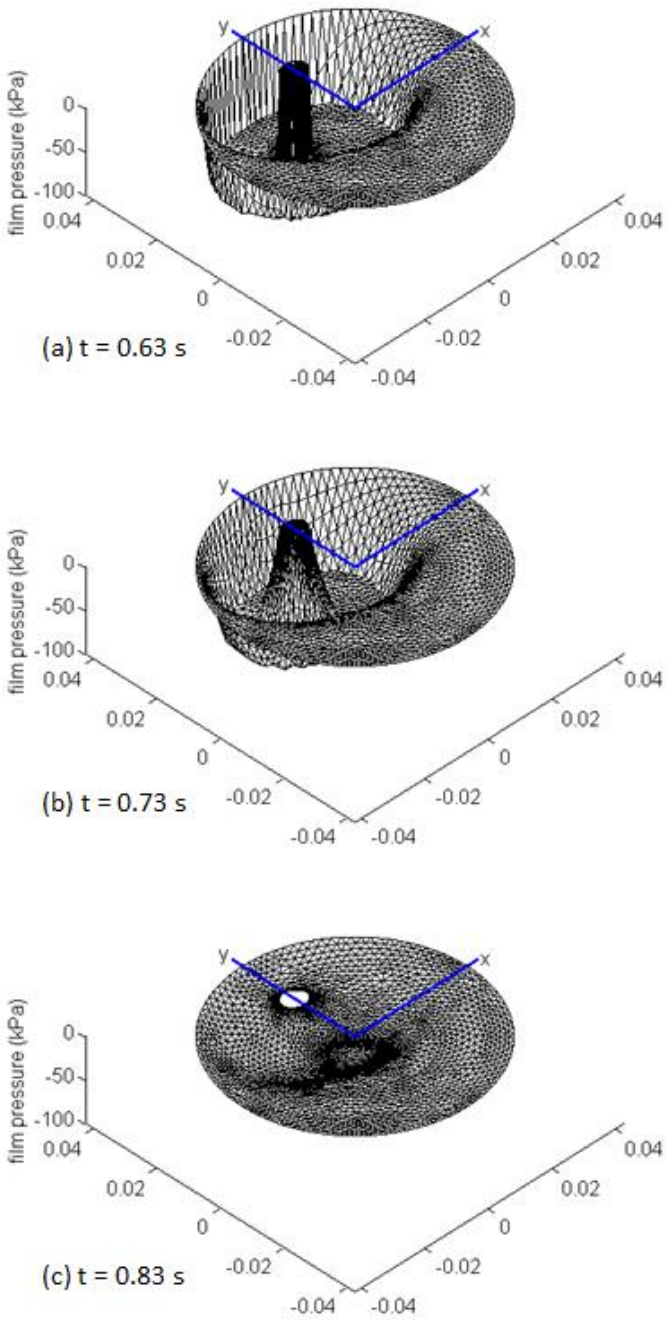

Figure 4.4: Swing phase pressure distributions, unrestricted flow through clearance hole; $v = v_0$

Figure 4.5 shows the spatial distributions of film pressure for the completely restricted flow case under the same conditions.

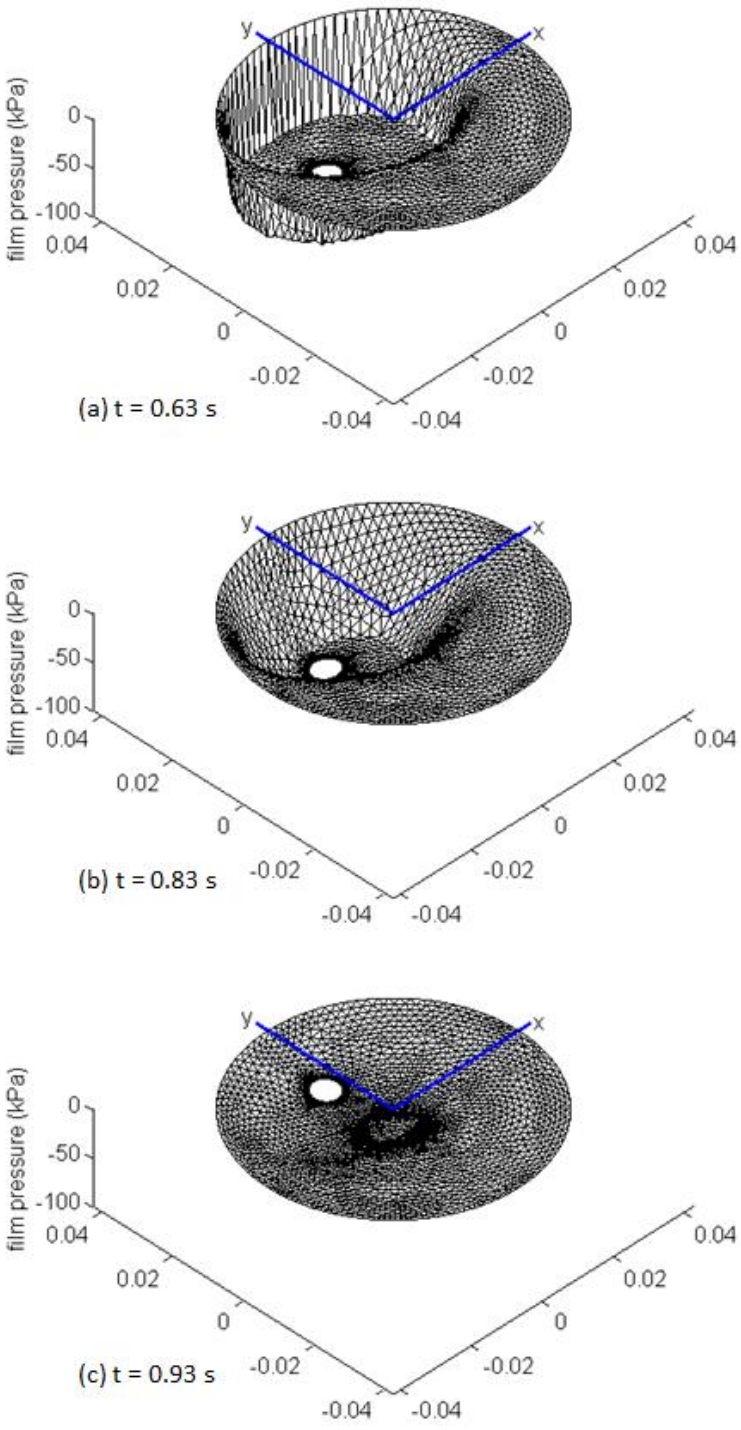

Figure 4.5: Swing phase pressure distributions, completely restricted flow through clearance hole; $v = v_0$

Complete reformation of the lubricant film occurs at t = 0.919s, or t_r = 0.289s. This refill time is slightly longer than for the lateral design under the same conditions but still occurs well before the end of the swing phase. Figure 4.6 investigates the effect of cavitation threshold pressure on the refill time t_r.

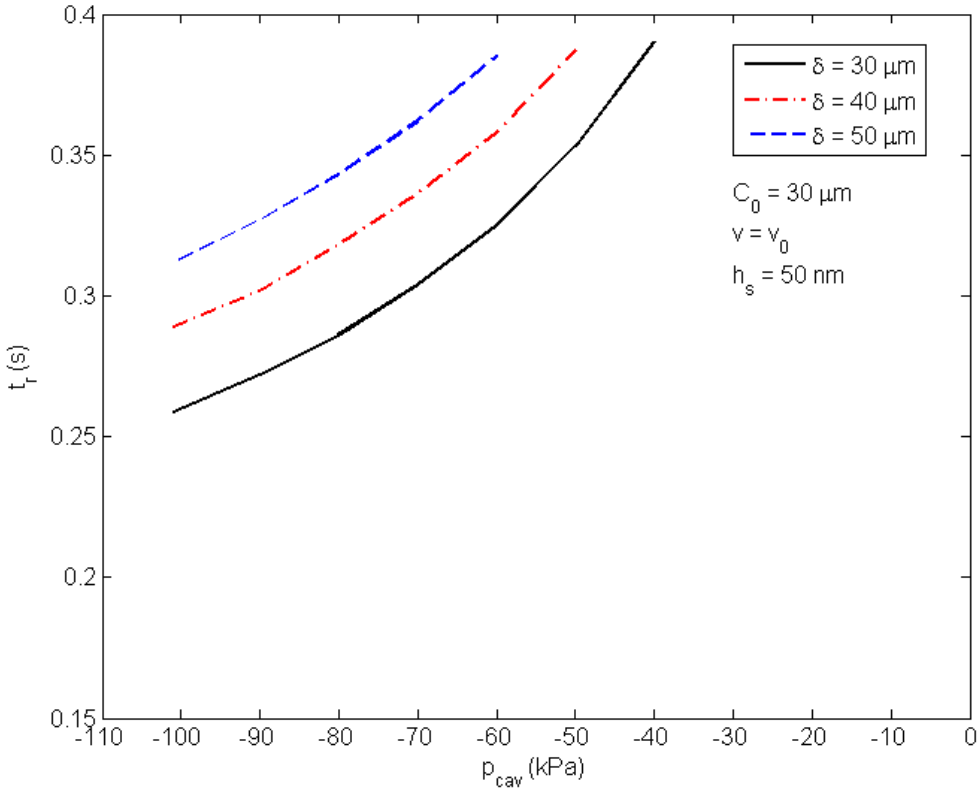

Figure 4.6: Effect of cavitation threshold pressure on refill time, completely restricted flow through clearance hole

Refill time is more sensitive to changes in ellipticity for the in-line design configuration. Similarly to the lateral design, these results also show a strong dependency on the prescribed cavitation threshold pressure. Furthermore, the range of p_{cav} values at which complete reformation occurs is smaller for the in-line design than for the lateral design.

Figure 4.7 investigates effect of ball velocity on refill time at two cavitation threshold pressures that span the range of possible p_{cav} values found in practice. Note that velocity is

represented as a ratio of the prescribed velocity v over the reference velocity v_0. The ellipticity is held constant at $\delta = 40\mu m$.

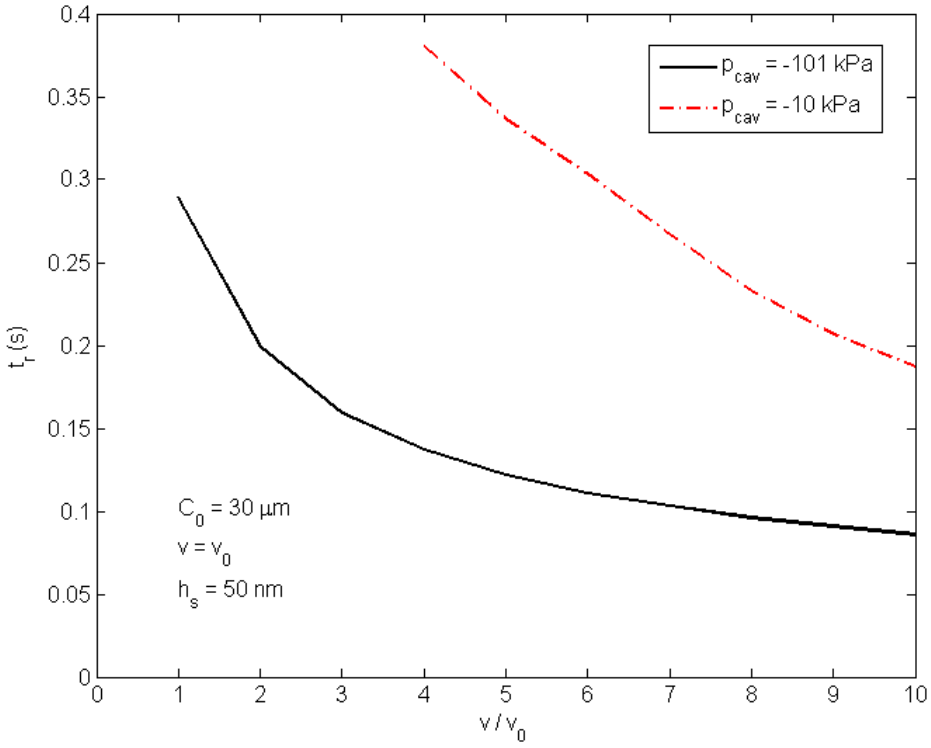

Figure 4.7: Effect of ball velocity on refill time, completely restricted flow through clearance hole

These results show that refill time is strongly dependent on ball velocity during the swing phase for the in-line configuration. Full-film reformation does occur at near-ambient cavitation threshold pressures (-10kPa) with marginal increases in ball velocity over the reference velocity.

The results presented in this section for the in-line design configuration show that the reformation of a complete lubricant film during the swing phase is possible (assuming a sealed boundary at the clearance hole for the elastic element) under the same conditions simulated for the lateral design in Boedo and Booker [25]. The refill times are slightly longer for the in-line design than for the lateral configuration, but the simulations do predict full-film reformation of the cavitation region prior to the start of the next stance phase.

Chapter 5: Wear Studies

5.1 Introduction

The purpose of this chapter is to present and discuss the wear characteristics of the implant designs described in Chapter 2. Section 5.2 discusses the method applied for contact analysis (using ANSYS), and Section 5.3 describes the wear formulation and its application to the wear studies completed in this chapter. Furthermore, the wear results are organized into three primary sections: the conventional design models, the lateral design models, and the in-line design models. There is an additional section that discusses the effects of friction, radial clearance, and ellipticity of the cup on wear rates.

The wear formulation detailed in Section 5.3 is applied universally to all designs. The conventional models in this work act as controls for comparison purposes; further results showing the validation of these models are discussed in Appendix A. Clinical wear data is also displayed in this section. Clinical wear rates traditionally are highly variable between patients and therefore span large ranges of values. As such, this data is used to show that the simulated results fall reasonably within accepted wear ranges.

5.2 Contact analysis

All FE contact analysis is performed using the nonlinear contact features in ANSYS 14.0. 10-node SOLID186 tetrahedral elements are used to model each design. TARGE170 and CONTA174 elements are assigned to the contact surfaces using the built-in Contact Wizard, choosing the surface-to-surface contact option. The 'Target' elements are consistently applied to the cobalt-chrome ball surface, while the softer UHMWPE material is prescribed as the 'Contact' surface. In simple cases (sphere-on-plane geometries, for example) contact pressures and distributions are not affected by the denotation of Contact and Target surfaces; in models where more complex geometries are analyzed, ANSYS recommends that the significantly stiffer material is prescribed as the Target surface for accuracy and convergence reasons.

The default Augmented Lagrangian contact algorithm is used for this work; this method is an iterative approach that employs a contact 'spring' to establish a relationship between the

surfaces (known as the 'penalty' method) and generally leads to better conditioning and lower sensitivity to stiffness parameters than the standard penalty approach. As such, a default value of 1.0 was used for contact stiffness parameters FKN and FKT; since compression dominates the deformation of the surfaces, the default values are recommended (for bending-dominated analyses, lower values are recommended). Additionally, the 'Standard' surface behavior option is chosen in each case, which assumes unilateral contact (sliding is included) between surfaces and most closely represents actual material surface interaction in the designs.

There are two main techniques applied to solve nonlinear contact problems in ANSYS: Load Control and Displacement Control. Load Control is the conventional approach in ANSYS, where the prescribed Contact and Target surfaces are moved into an initial contact position (or overlap of the two surfaces) and the loads are subsequently applied to the model. The loading causes the displacement of the contact surfaces to solve for penetration depth and consequently a contact pressure distribution. This is the most efficient method for solving FE models with prescribed loading driving the contact between surfaces. Displacement Control instead moves the surfaces together with a user-defined displacement and calculates the resulting contact pressures and net reaction forces to the prescribed displacement of one surface into another.

For more complicated geometries and contact situations, both methods may need to be applied using multiple Load Steps to achieve convergence. Displacement Control is first used (as Load Step 1) to initiate contact between the surfaces. Load Step 2 is a null step that transitions the analysis from displacement control to load control through the use of the LDREAD command in ANSYS, which 'reads in' the results (*i.e.* reaction forces, node locations) of the displacement analysis and allows the model to 'settle-in'. Load Control is then applied in Load Step 3 to provide the final contact results for the given model and loading conditions. This Displacement-Load Control method is longer (sometimes significantly, as there are two full contact analyses solved as opposed to one) but leads to better convergence in complicated problems. Furthermore, use of transient analysis options coupled with ramped loading means that this method can be used to solve nearly any contact problem in ANSYS, provided the machine being used has sufficient computing power.

The loading and kinematic conditions applied to the FE models are taken from the generally accepted ISO 14242 standard [20] that is employed in hip simulator wear testing. Though these particular gait conditions may not be representative of all hip implant patients, it is

a widely used duty cycle for lubrication and wear analyses in this field. The ISO 14242 loading F^Z (from ball to cup) is unidirectional along the positive Z axis and shows a relatively high double-peak load of 3000N in the stance-phase of the gait cycle (until ~0.62 seconds). The swing-phase (from ~0.62 to 1.0 seconds) is characterized by a low but still positive load of 300N. The kinematics (ω^Y) correspond to rotation only about the flexion-extension (Y) axis of the implant and are not applied to the FE models directly but rather to the wear program run after contact pressures are extracted from ANSYS.

In the case of the novel design models, Displacement Control is used to simulate contact between the ball and elastic columns. For example, the lateral design is modeled so that the ball is centered on the X_N-Y_N-Z_N frame initially; at this point the contact surfaces are in the 'just-touching' position. The elastic elements are designed to displace an 'offset' distance e_0 to a position where the ball and cup are concentric, providing a net 350N reaction force in the $-Z_N$-direction. When the ball and cup are concentric, the ball can only physically move an additional distance equivalent to the radial clearance between the bearing surfaces. As the clearances recommended by Boedo and Booker [24] are considerably smaller than the e_0 value (C varies between 10 and 40μm), the spring load increases only a small percentage above the predicted 350N load and affects wear rates negligibly. As such, it is assumed in this work that the ball remains at a position generally concentric to the cup during the entire gait cycle, providing a constant contact stress distribution. Displacement Control is therefore used to prescribe a position along the $+Z_N$ axis for the ball equivalent to e_0 and calculate contact pressures at this penetration depth.

The ISO 14242 load conditions are applied directly to the conventional models employing the combination of Displacement and Load Control discussed earlier in this section. The loads are applied in 21 instants of the gait cycle through Load Steps in a macro script written in the APDL language for ANSYS. Each successive Load Step is ramped from the previous instance, allowing convergence in 2-6 instances. It should be noted that the conventional model (16mm radius) is also simulated under the load conditions used by Maxian *et al.* [30], taken experimentally by Brand *et al.* [44]. This gait cycle is simulated so that the results found in this work can be validated with published results using the same methods and these results can be found in Appendix A. Furthermore, this duty cycle is characterized by load components in all three directions (X_C, Y_C and Z_C), though the peak values are relatively smaller than the ISO

14242 loads. As such, the ball is allowed freedom to move within the cup (there are no displacement constraints applied to the ball geometry in the FE model) which allows the contact region to move depending on the load components in the X_C- and Y_C-directions.

5.3 Wear formulation

This work applies a sliding-distance-coupled wear algorithm adapted from Maxian *et al.* [30] that is based on Archard's wear law:

$$h = k * P * S \tag{5.1}$$

where h is linear wear depth; k is a material and surface dependent wear coefficient; P is the contact stress, evaluated in this work by utilizing the nonlinear contact features in ANSYS 14.0; and S is the sliding distance associated with a point on the contact surface. This equation is evaluated locally at each node site in the FE model, and a global wear matrix W given by

$$W(\theta, \phi) = \sum_{i=1}^{N} k * \sigma_i(\theta, \phi, t) * s_i(\theta, \phi, t) \tag{5.2}$$

is formed for the entire contact surface. Here, N is the total number of loading/kinematic instances applied to the FE model; $\sigma_i(\theta, \phi, t)$ is the contact stress distribution at each instance; and $s_i(\theta, \phi, t)$ is the sliding distance between each instance, which is defined as

$$s_i(\theta, \phi, t) = \Delta n_i(t) * r(\theta, \phi) \tag{5.3}$$

where $\Delta n_i(t)$ is the change in flexion/extension angle between successive instances and $r(\theta, \phi)$ is the perpendicular distance between the node and the flexion/extension axis of rotation. Only flexion/extension kinematics are applied to the wear model to simplify the sliding distance calculation. This assumption is common in wear analyses since flexion/extension rotation dominates the kinematic behavior of the joint.

The wear coefficient chosen for analysis has a large impact on wear results. Since k is dependent on the material, surface characteristics, lubrication and contact pressure, it is not possible to prescribe a single value to this coefficient for *in vivo* conditions [19]. As such, different wear models use conflicting values for k, as there is not sufficient experimental data to

adopt a single value. This work assumes k = 10.656E-07 $mm^3\ N^{-1}\ m^{-1}$ for MOP designs – the value used by Maxian *et al.* [30] extrapolated from Streicher and Schoen [56] – and k = 0.5E-08 $mm^3\ N^{-1}\ m^{-1}$ for MOM designs [57].

This wear formulation is applied to both the novel and conventional models through a combination of APDL and Matlab macros. After the contact analysis is completed in ANSYS, two APDL macros are run to output critical information to text files. The first writes 'Preprocessor' nodal coordinate values (and their corresponding node numbers from the model) into 'nodalareas.dat' for *all* Contact surface nodes present in the given model. The second macro writes 'Preprocessor' nodal coordinate values and 'Postprocessor' contact pressures and contact status values into 'contactdataX.dat' after selecting *only* nodes that are considered 'in contact' in the model, where X denotes the results for a particular Load Step. Due to the element type selected (SOLID186) and the associated behavior of mid-size nodes for each contact element, not every node on the Contact surface is analyzed for contact during the ANSYS analysis. This leaves nodes within the contact region without contact pressure or contact status simply due to the fact that ANSYS does not calculate those results at every node in the element. Due to this phenomenon, a secondary Matlab operation is required to sort the elements and provide an accurate value for contact area.

At this point, two text files exist that contain the information needed to predict wear for the given contact analysis. The normal distance between a specified contact node j and the Y_N rotation axis r is calculated by Eqns. 5.4 and 5.5 for the novel and conventional designs, respectively:

$$r_j^N = \sqrt{{X_{N,j}}^2 + {Z_{N,j}}^2} \tag{5.4}$$

$$r_j^C = \sqrt{{X_{C,j}}^2 + {Z_{C,j}}^2} \tag{5.5}$$

Since the kinematic data is given in terms of angular velocity ω^Y by ISO 14242, elementary kinematic equations are applied to calculate the change in rotation angle Δn between each instance i:

$$\Delta n_i = abs\left[\frac{1}{2} * (\omega_{i-1}^Y + \omega_i^Y) * \Delta t_i\right] \tag{5.6}$$

where $\Delta n_i = n_i - n_{i-1}$; ω^Y refers to the angular velocity given by the ISO 14242 standard at the specified instance, and Δt_i is the change in time between successive instances. It is assumed in this calculation that the angular velocity changes linearly between instances.

Due to the assumptions regarding contact pressure made for each design type, a separate wear calculation program is used for each design. For the novel designs, the single contact pressure distribution (contactdata.dat) is applied to each instance of the gait cycle over the Δn vector, which is a separate text file. For the conventional design, a separate linear wear rate is calculated for each instance (or Load Step) of the ANSYS analysis. A total of 21 contactdataX.dat files are created, each corresponding to a separate contact analysis with different loading conditions. A linear wear rate is calculated for each node at each instance and then the values for each instance are summed to provide a cyclic linear wear rate for each node location. Keeping consistent with most wear predictions, it is assumed that the implant undergoes $1x10^6$ cycles per year [30, 32, 34]. At this point, the maximum annual linear wear rate can be selected from the linear wear vector.

The calculation of volumetric wear is slightly more complicated, as 'nodal areas' need to be calculated for each node that is considered 'in contact'. Moreover, the fact that not every node on the Contact surface is analyzed for contact means that built-in nodal area calculators for ANSYS (such as the ARNODE function) cannot be used because they will underestimate the area of the contact region. This necessitates that the two sets of nodes (*all* contact nodes in nodalareas.dat and *only* nodes with contact status in contactdataX.dat) be interpolated over identical meshes so that a true ratio can be calculated between node sets. To accomplish this, a uniform mesh is created to be used for both node sets of 500x500 nodes using the 'meshdata' command. The contact status of each node for the contactdataX.dat node set (if status is greater than or equal to 2 in ANSYS the node is considered in contact) is then interpolated over this mesh using the 'griddata' command. Likewise, the nodalareas.dat node set is interpolated over the same mesh, allowing a ratio to be formed. This true ratio relates the number of interpolated contact nodes ${CN_i}^{interp}$ to the total number of interpolated nodes on the Contact surface ${TN_i}^{interp}$ and is used to calculate the nodal area ${A_i}^{node}$ of each node with contact status:

$$ {A_i}^{node} = \left(\frac{{CN_i}^{interp}}{{TN_i}^{interp}} * SA \right) * \frac{1}{{CN_i}^{actual}} \tag{5.7} $$

where SA is the surface area of the Contact surface in the FE model and CN_i^{actual} is the actual number of contact nodes from the ANSYS model. Calculated for each instance of the gait cycle, this nodal area value is then multiplied by the linear wear depth at each node and summed to provide a volumetric wear rate per cycle. An annual rate can be calculated by multiplying this value by $1x10^6$ cycles per year.

5.4 Wear results for the conventional models

As discussed in Section 2.3, there are two types of conventional models simulated in this work: metal-on-plastic (MOP) and metal-on-metal (MOM). Both model types are necessary for comparison against the novel designs, as both MOP and MOM contact are expected depending on whether coatings are applied to the elastic elements. A non-zero friction coefficient is required for the conventional models so that the contact algorithm converges. It is shown in Section 5.7.1 that wear results are insensitive to the friction coefficient chosen (less than 0.065). As such, a coefficient of friction of 0.01 is used for the conventional models. A nominal radial clearance of C_0 = 40μm is used for the conventional models presented in this section. The conventional wear results are presented first so that comparisons can be readily made to the novel designs in the sections that follow.

5.4.1 Metal-on-Plastic (MOP)

The contact pressure distribution changes at each instance of the ISO14242 duty cycle due to the variable load transmitted in the implant. Since the contact pressure distribution has a direct effect on linear wear rate, it is important to understand the variation in the contact region across the entire gait cycle. Figure 5.1 shows the evolution of the contact region for the 16mm radius MOP model. Note that the time between each successive instance is 0.05s.

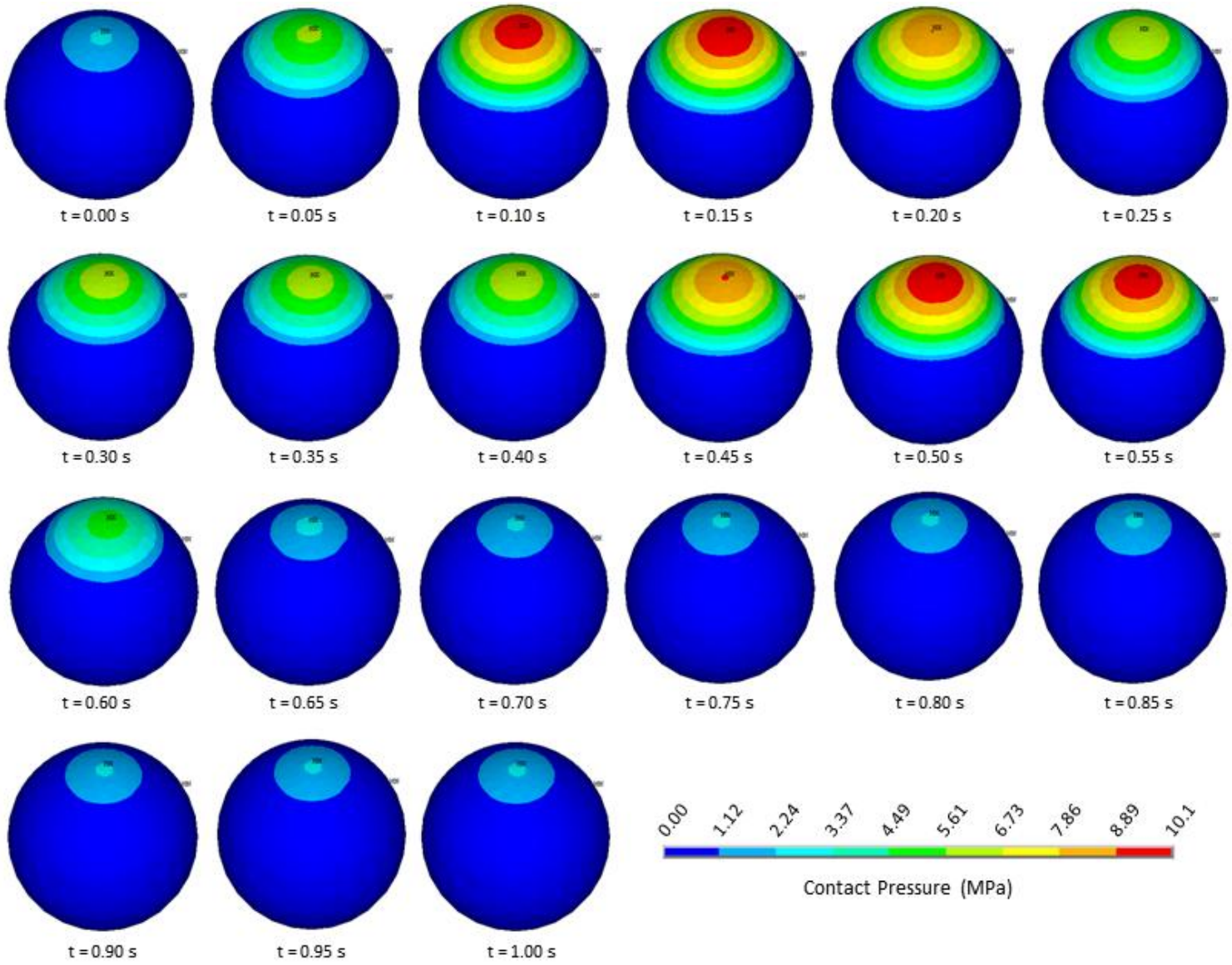

Figure 5.1: Evolution of contact region, 16mm MOP conventional model

Figure 5.2 displays the linear wear distribution for the conventional MOP design accumulated over the entire gait cycle. Figure 5.2(a) shows the 16mm radius model, while Figure 5.2(b) shows the 25mm radius model. Table 5.1 lists the wear results for the conventional MOP designs compared with clinical data, taken from Maxian *et al.* [30]. There is no clinical data available for the 25mm radius conventional design, as most MOP implants are in the 11mm to 16mm radius size range [19].

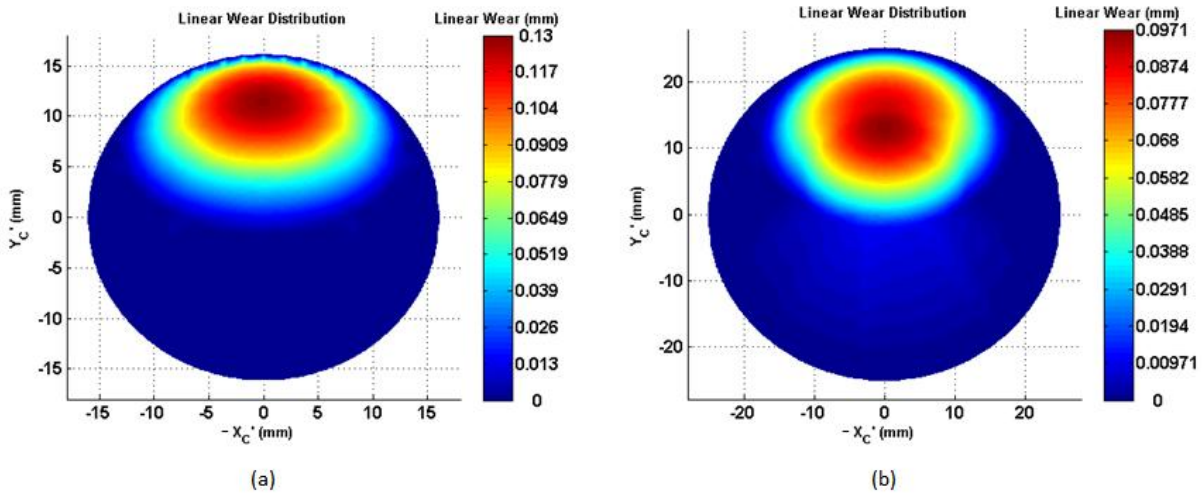

Figure 5.2: Linear wear distribution; (a) 16mm, (b) 25mm

Radius	Simulated Results		Clinical Data	
	Linear Wear Rate	**Volumetric Wear Rate**	**Linear Wear Rate**	**Volumetric Wear Rate**
Units	mm/year	mm^3/year	mm/year	mm^3/year
16mm	0.1298	46.20	0.10 ± 0.06	3 to 256
25mm	0.0971	80.47	-	-

Table 5.1: Summary of wear results, MOP conventional models

5.4.2 Metal-on-Metal (MOM)

The MOM conventional models are required for direct comparison with the novel designs that employ a high-modulus coating on the contact surface, as this contact is metal-on-metal in nature. The MOM models have the same geometry as the MOP models; however the cup insert has the same material properties of the cobalt-chrome ball and backing. Figure 5.3 shows the evolution of the contact region for the 16mm radius MOM model.

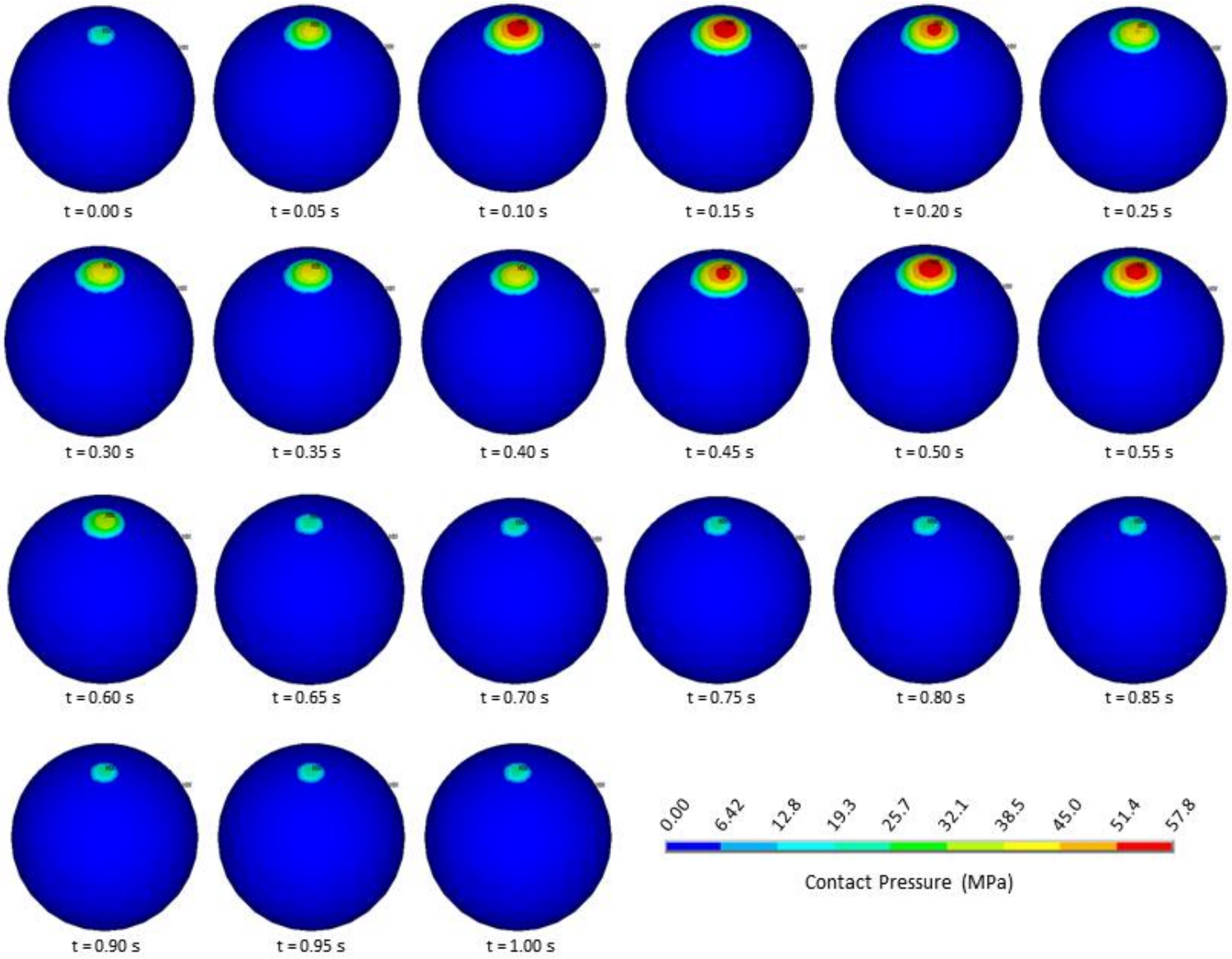

Figure 5.3: Evolution of contact region, 16mm MOM conventional model

Figure 5.4 displays the linear wear distribution for the MOM design. Figure 5.4(a) shows the 16mm radius model, while Figure 5.4(b) shows the 25mm radius model. Table 5.2 lists the wear results for the MOM conventional designs compared with clinical data. Note that the clinical data for MOM designs is taken from a much smaller sample size than exists for MOP implants. The clinical linear wear rates listed are a range of mean values from multiple studies of explanted MOM implants after *in vivo* use between 1 and 73 months post-surgery [26, 27, 29]. The clinical volumetric wear rate is taken from Morlock *et al.* [28] and is a range taken from explanted implants in which no edge loading was found. Edge loading is a separate issue that can cause an order of magnitude increase in volumetric wear in certain patients and is not representative of the simulations in this work. There is no clinical data available for the 16mm radius conventional design, as most MOM designs are approximately 25mm in radius.

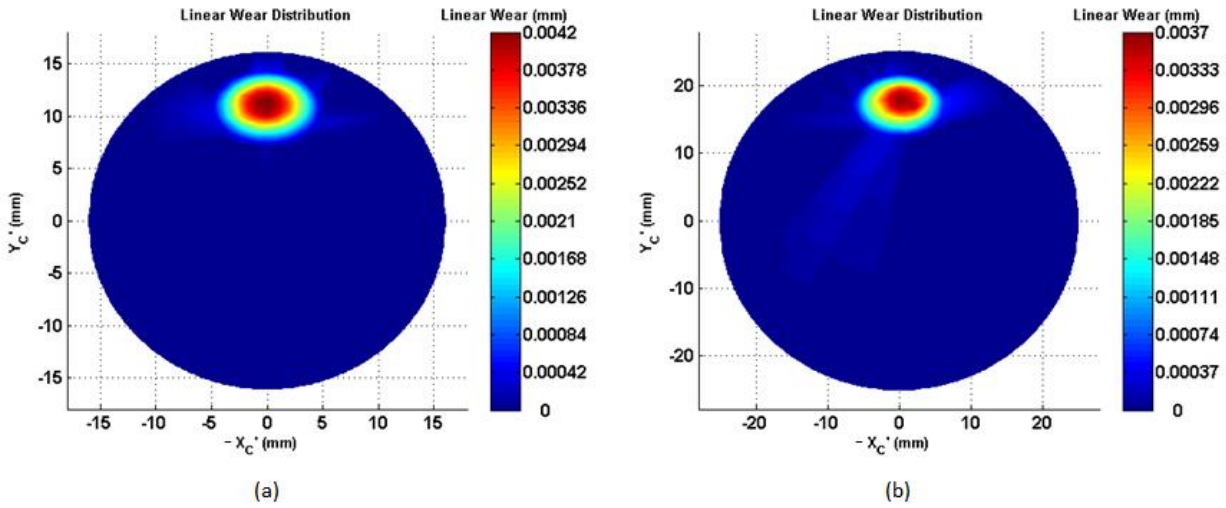

Figure 5.4: MOM linear wear distribution; (a) 16mm, (b) 25mm

Radius	Simulated Results		Clinical Data	
	Linear Wear Rate	Volumetric Wear Rate	Linear Wear Rate	Volumetric Wear Rate
Units	mm/year	mm^3/year	mm/year	mm^3/year
16mm	0.0042	0.271	-	-
25mm	0.0037	0.420	0.0039 to 0.0090	0 to 4.9

Table 5.2: Summary of wear results, MOM conventional models

5.4.3 Discussion

The results for the conventional models show expected contact regions and reasonable wear rates that fall within clinical wear ranges. The contact regions are centered near the 'top' of the cup – where the $+Z_C$ axis passes through the cup-backing assembly – due to the unidirectional loading of the ISO 14242 Standard. The contact pressure plots (Figures 5.1 and 5.3) show the double peak of the stance phase loading at 0.15s and 0.50s, while the constant swing phase loading is evident in the final 8 instances (greater than 0.62s). The location of the contact regions in these figures correspond to the location and size of the linear wear distributions plotted in Figures 5.2 and 5.4. It should be noted that significantly higher volumetric wear rates are found at the 25mm radius models, as the larger contact surfaces lead to larger contact regions and therefore a larger distribution of linear wear, even though the maximum linear wear rates are somewhat lower for the 25mm radius models.

More specifically, the MOP models are characterized by relatively large contact regions compared with the radii of the contacting surfaces; this can be attributed to the similar radii of the surfaces (small clearances), the conformal nature of the bearing, and the fact that the high-modulus ball surface significantly deforms the surface of the low-modulus cup due to the large difference in elastic moduli. These results reinforce claims made by Mattei *et al.* [19, 32, 57] that Hertzian contact theory cannot be effectively applied to MOP implants. With respect to clinical wear data, the simulated results fall well within the expected wear ranges for both linear and volumetric wear.

The MOM models are characterized by relatively small contact regions due to the identical elastic moduli of the bearing surfaces. As such, the simulated contact pressures are significantly higher than the MOP models. Due to the significantly smaller wear coefficient used for MOM contact, linear wear rates in these models are similarly significantly lower than the MOP models, which is to be expected. The simulated results compare reasonably well with clinical wear data.

5.5 Wear results for the lateral design models

This section presents the results for the novel lateral design models described in Section 2.1.1. The wear results are separated into two segments: models with elastic elements that are *not* coated and models employing elastic elements *with* coatings. Each novel design type is further compared against its corresponding conventional model (MOP for uncoated elements, MOM for coated elements) for consistency. As discussed in Section 5.2, the contact pressure distribution for these models is assumed to be constant at each instance of the gait cycle.

The results for the novel design models show 'Peak Contact Pressure' and 'Net Reaction Force' in addition to the linear and volumetric wear results for two reasons: first, it is important to understand the effect of these parameters when the initial offset e_0 is varied; and second, the reaction force (which is inherently related to contact pressure) created by the elastic elements is an integral component of design functionality and should be tracked to verify that the elastic elements are providing a reaction force that is reasonably close to the predicted value for a particular design. Volumetric wear for these models is calculated for both elastic columns.

5.5.1 Load variation study

The purpose of the elastic elements in the lateral design configuration is to provide a reaction force to the ball that causes separation of the bearing surfaces during the swing-phase of the gait cycle. Due to large variations in gait cycle loading conditions between patients, it is difficult to specify a singular value for swing-phase loading of the implant and therefore difficult to predict a sufficient reaction load required for the novel design. Taking into account the uncertainty surrounding the swing-phasing loading, this load variation study provides a range of designs that can be effective for swing-phase loads between 0 and 300N (in $+Z_N$-direction). Since the ISO 14242 standard is generally considered to be a conservative gait cycle prediction, the specified swing-phase loading of 300N is assumed to be the worst-case (high-end) loading condition. As such, novel designs that predict net reaction forces of 50 to 350N are simulated in this section at increments of 50N to provide a range of implant designs that apply to a variety of swing-phase loading conditions.

Figure 5.5 shows the linear wear distributions on the surface of the uncoated elastic elements for the 350N reaction load case. Figures 5.6 and 5.7 provide the linear wear distributions for the load variation study for the 16mm and 25mm radius models, respectively. The predicted (theoretical) reaction load for each case is displayed below its associated wear plot. Note that the color/wear scheme remains constant in each plot (applying the range used for the 350N case) so that the linear wear distributions for each design can be compared directly.

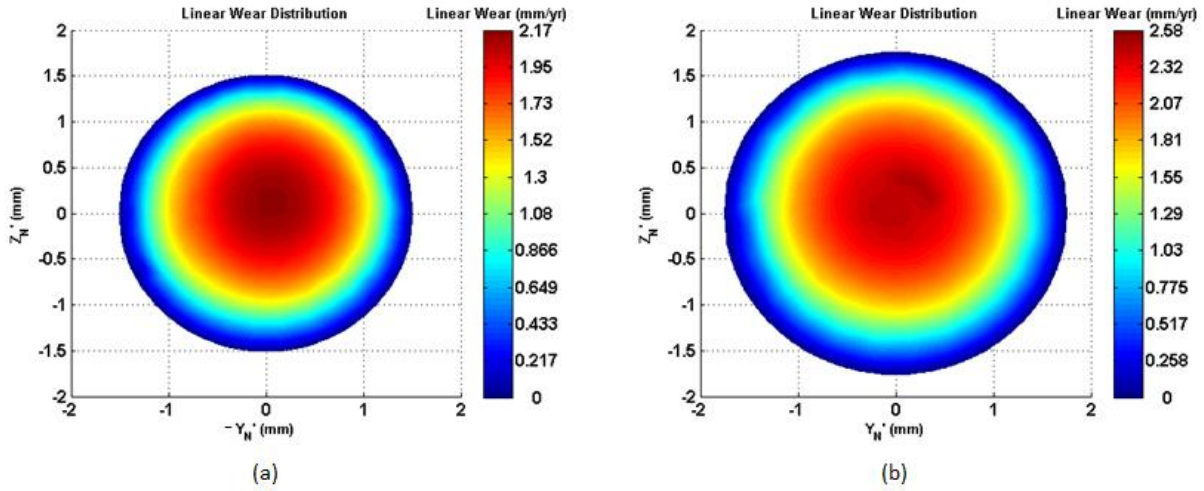

Figure 5.5: Linear wear distributions on uncoated elastic surface, F_z = 350N; (a) 16mm, (b) 25mm

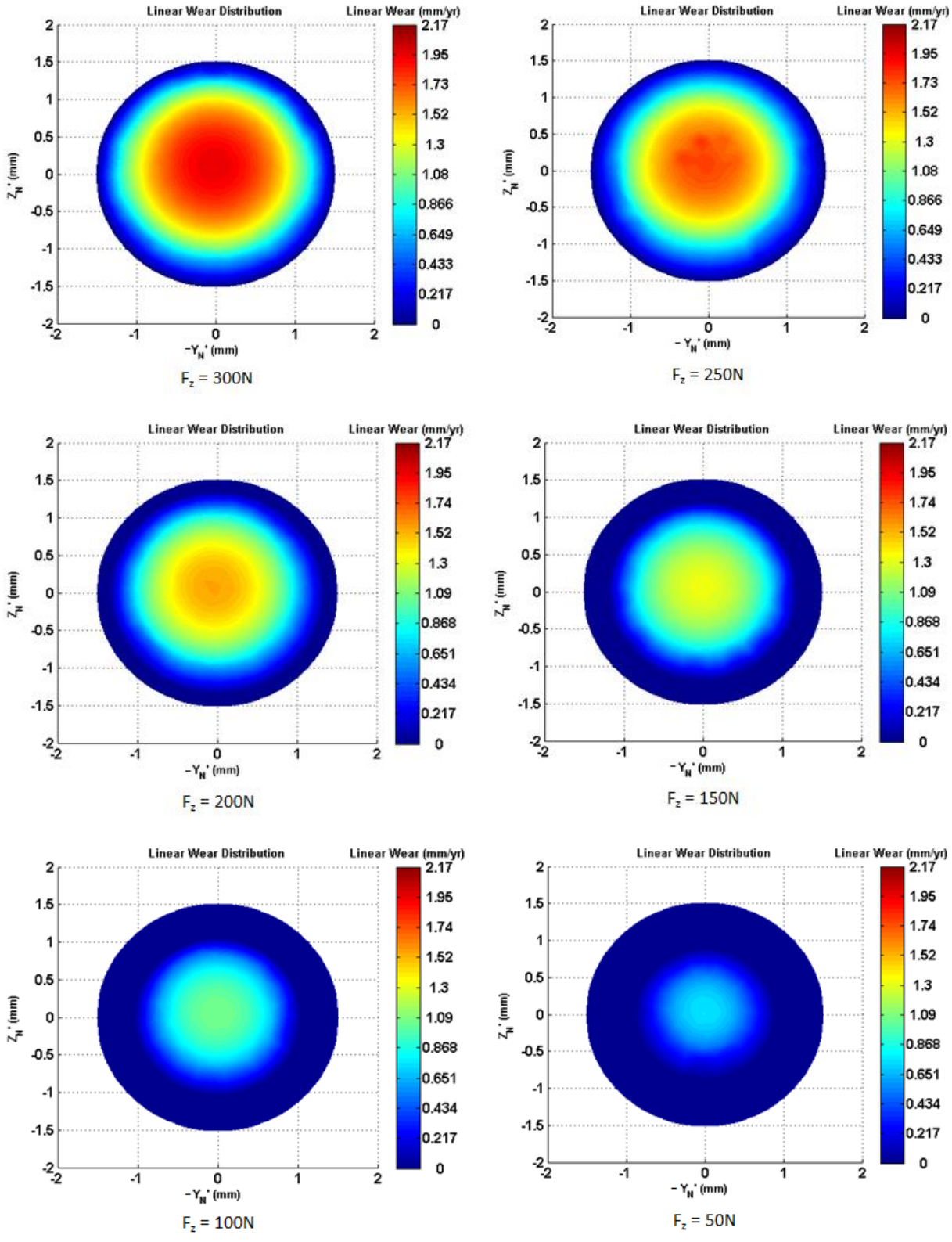

Figure 5.6: Linear wear distributions on uncoated elastic surface, 16mm load variation study

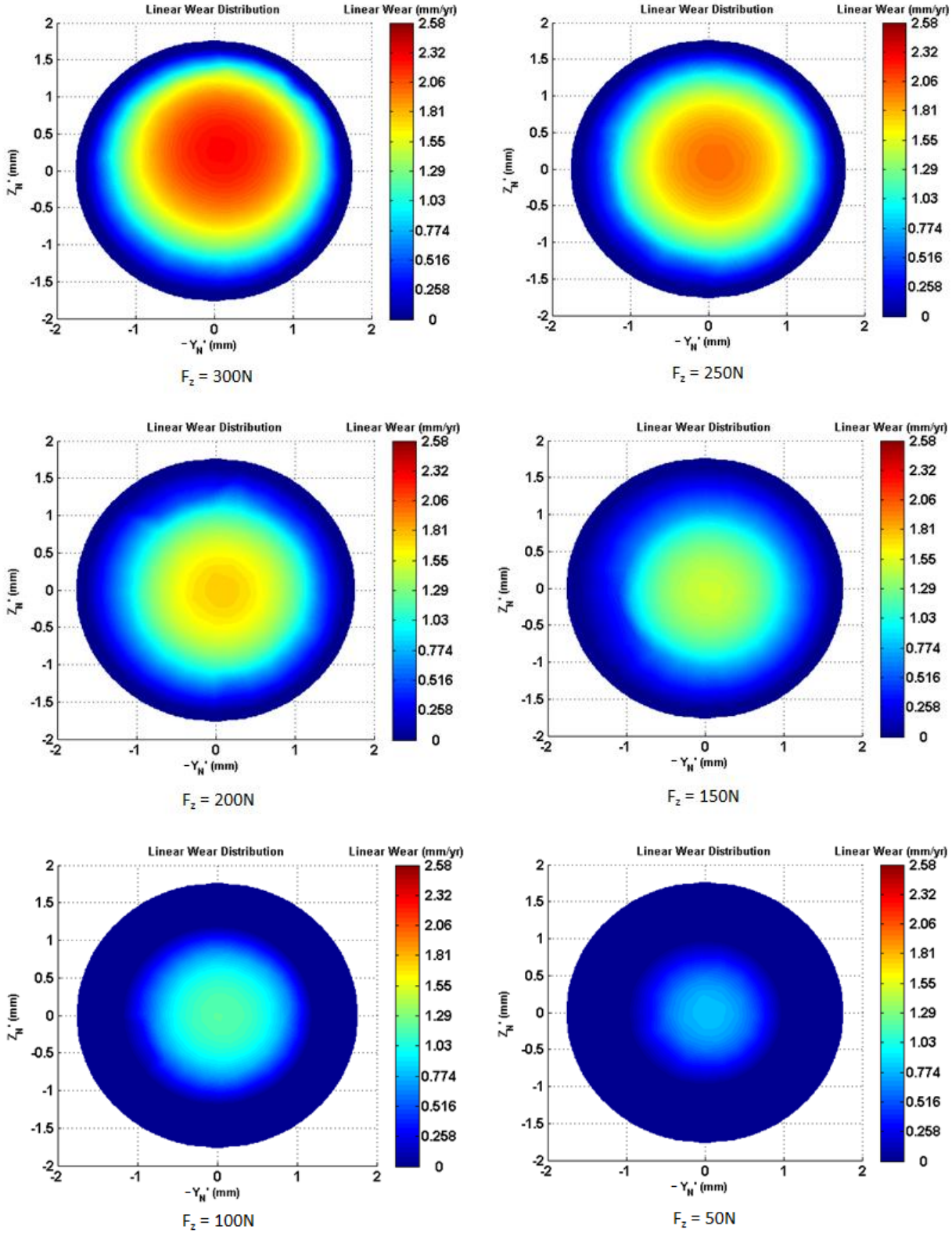

Figure 5.7: Linear wear distributions on uncoated elastic surface, 25mm load variation study

Tables 5.3 and 5.4 display the contact and wear results for the 16mm and 25mm radius models, respectively. The diameters of the columns are fixed for each size (3.0mm for 16mm model and 3.5mm for 25mm model) allowing the desired reaction force F_z to be calculated by varying the initial vertical offset e_0.

F_z	**e_0**	**Peak Contact Pressure**	**Net Reaction Force**	**Linear Wear Rate**	**Volumetric Wear Rate**
N	mm	MPa	N	mm/year	mm^3/year
350	-0.648	91.2	306.39	2.165	14.26
300	-0.556	83.2	258.25	1.976	12.11
250	-0.463	76.6	209.76	1.821	9.58
200	-0.370	67.0	161.55	1.591	7.41
150	-0.278	56.8	114.63	1.350	5.24
100	-0.185	45.9	68.83	1.089	2.96
50	-0.093	30.2	27.76	0.780	1.13

Table 5.3: Load variation study results, 16mm model

F_z	**e_0**	**Peak Contact Pressure**	**Net Reaction Force**	**Linear Wear Rate**	**Volumetric Wear Rate**
N	mm	MPa	N	mm/year	mm^3/year
350	-0.476	69.6	304.52	2.583	22.68
300	-0.408	61.8	254.49	2.294	18.41
250	-0.340	54.4	204.98	2.120	14.79
200	-0.272	47.6	156.28	1.765	11.17
150	-0.204	40.6	109.07	1.507	7.29
100	-0.136	32.7	64.64	1.211	4.10
50	-0.068	22.5	25.30	0.836	1.44

Table 5.4: Load variation study results, 16mm model

5.5.2 Models with high-modulus coatings

Due to relatively high linear wear rates of the low-modulus elastic elements compared with the total length of the columns, high-modulus coatings are applied to the contact surfaces of the elastic elements in an effort to decrease linear wear. As discussed in Section 2.1.1, coating thicknesses of 200µm and 400µm are simulated for the novel design orientation while keeping the geometric parameters the same. The same initial offset e_0 is used for the coated models as well; the validation of this effective spring stiffness is detailed in Appendix A.

Figures 5.8 and 5.9 show the linear wear distributions for the 200µm and 400µm coating thicknesses, respectively. Note the 'ring' of higher contact pressure around a circular region of lower contact pressure in the 200µm case; this phenomenon is not seen for the 400µm thickness, presumably because of the increased amount of high-modulus material between the ball and low-modulus column.

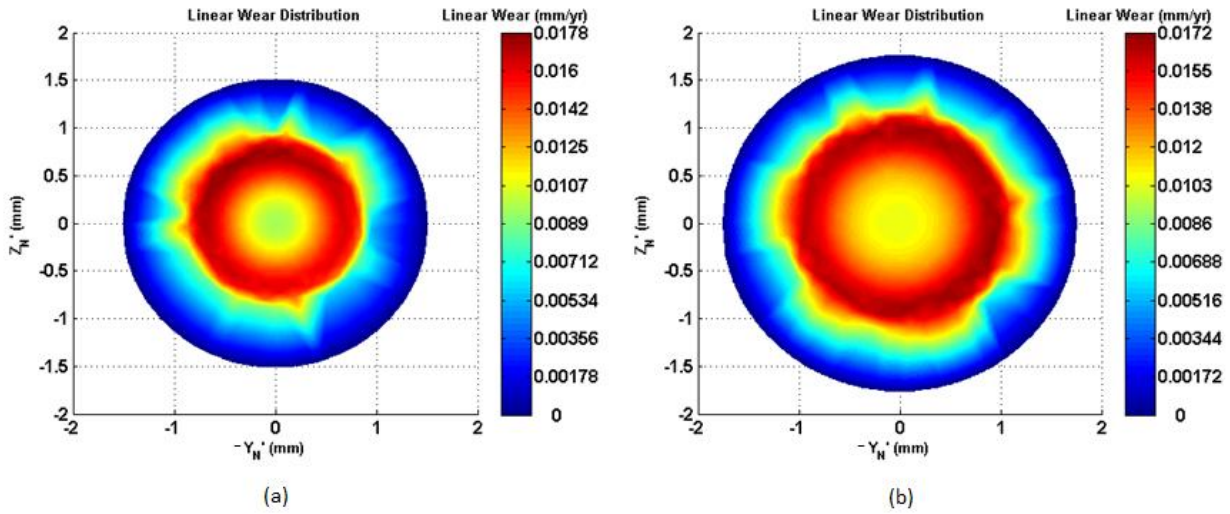

Figure 5.8: Linear wear distributions, 200µm coating; (a) 16mm, (b) 25mm

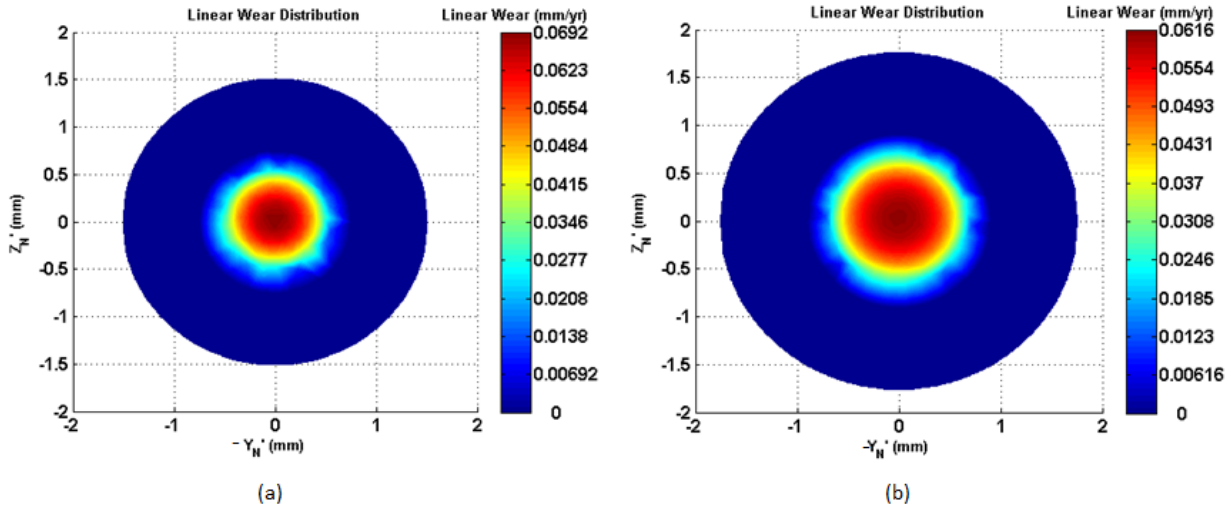

Figure 5.9: Linear wear distributions, 400μm coating; (a) 16mm, (b) 25mm

Table 5.5 displays the contact and wear results for the high-modulus coated models. Again, the diameters of the columns are fixed for each size (3.0mm for 16mm model and 3.5mm for 25mm model). These models are simulated with e_0 values that correspond to a predicted 350N reaction force on the ball.

Radius	**e_0**	**Coating Thickness**	**Peak Contact Pressure**	**Net Reaction Force**	**Linear Wear Rate**	**Volumetric Wear Rate**
mm	mm	μm	MPa	N	mm/year	mm^3/year
16	-0.648	200	159.0	327.99	0.0178	0.069
		400	621.0	350.70	0.0692	0.070
25	-0.476	200	98.8	324.02	0.0172	0.112
		400	354.0	348.25	0.0616	0.114

Table 5.5: Summary of wear results, lateral configuration with coatings

5.5.3 Comparison with conventional models

Table 5.6 presents the results from Sections 5.5.1 and 5.5.2 compared against the wear results from the conventional models. The 'No Coating' designation signifies the predicted 350N reaction load case presented in Section 5.5.1. Furthermore, the 'No Coating' case is compared directly against the MOP results for the conventional design, while the 200μm and 400μm cases are compared directly against the MOM results. Though linear wear rates between the 200μm and 400μm cases are significantly different (the 400μm case predicts 3.88 times more wear than the 200μm case), the volumetric wear rates are nearly identical. This can be attributed to the coating thickness; a thicker coating distributes the wear over a significantly smaller area than a thinner coating due to the additional high-modulus material between the contact surface and the low-modulus column. Since the contact region is significantly smaller for the 400μm case and the load being transmitted is identical in each case, the peak contact pressure is significantly larger for the 400μm model, even though the distributions of linear wear lead to very similar volumetric wear rates.

Radius	**Coating Thickness**	**Lateral Design Models**		**Conventional Models**	
		Linear Wear Rate	**Volumetric Wear Rate**	**Linear Wear Rate**	**Volumetric Wear Rate**
Units	μm	mm/year	mm^3/year	mm/year	mm^3/year
16mm	No Coating	2.165	14.26	0.1298	46.20
	200	0.0178	0.069	0.0042	0.271
	400	0.0692	0.070		
25mm	No Coating	2.583	22.68	0.0971	80.47
	200	0.0172	0.112	0.0037	0.420
	400	0.0616	0.114		

Table 5.6: Comparison with conventional models

5.5.4 Discussion

The results for the low-modulus elastic elements subjected to the load variation study show that this orientation and material selection is characterized by relatively high contact pressures due to the nature of the flat surface of the column being contacted by the spherical

surface of the ball. Similarly, linear wear rates for these designs are also relatively high, especially when compared with the overall length of the column. At the 350N predicted load case, 43.3% and 51.7% (16mm and 25mm radius, respectively) of the elastic column will wear away each year in the nodal location of peak contact pressure. Volumetric wear improves for this design – by 69.1% and 71.8% for the 16mm and 25mm radius models – when compared with the conventional model, but that is because there is significantly less contact area to distribution the pressure.

The load variation study shows that these linear wear rates will decrease to some extent by using smaller e_0 magnitudes to predict lower reaction loads. Specifically, for the 16mm radius model the linear and volumetric wear rates decrease by 64.0% and 88.5%, respectively, between the highest and lowest predicted reaction loads. Yet even at best-case (F_z = 50N), the linear wear rates are higher than desired. This study also shows that the predicted load F_z is directly proportional to linear wear rate (see Figure 5.10).

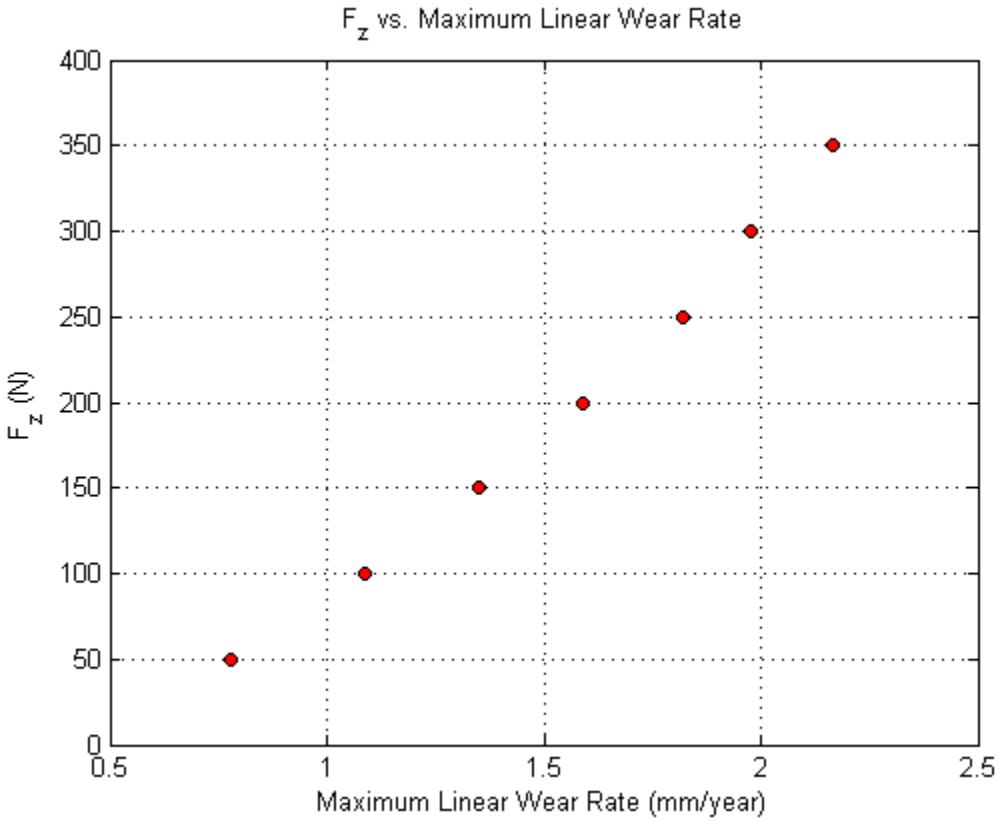

Figure 5.10: Relationship between predicted reaction load F_z and maximum linear wear rate, uncoated elastic surface

In an effort to decrease linear wear rates while keeping the geometry of the design largely unchanged, high-modulus coatings were applied to the contact surfaces of the columns. Marked by a significantly lower wear coefficient k, the coatings decrease linear and volumetric wear rates significantly when compared with the uncoated models. The 200μm coating shows the best combination of low volumetric wear and reasonable linear wear when compared with conventional models. Linear wear rate is somewhat higher for the novel design; however this coating thickness distributes the contact pressure in a way that keeps the peak pressure reasonable. For the 16mm model, the linear wear rates are 4.24 and 16.5 times greater than the MOM conventional design for the 200μm and 400μm coatings, respectively. For the 25mm model, the linear wear rates are 4.65 and 16.6 times greater than the conventional design for the 200μm and 400μm coatings, respectively.

However, the volumetric wear rates for the coated models show significant improvement over the conventional designs. The volumetric wear rates are 74.5% and 74.2% lower than the 16mm MOM conventional design for the 200μm and 400μm coatings and are 73.3% and 72.9% lower than the 25mm MOM conventional design for the 200μm and 400μm coatings, respectively. These improvements are fairly consistent with the uncoated design.

A useful metric for comparing linear wear rates for the coated and uncoated models is the predicted lifetime of the coating, listed in Table 5.7. It is assumed that the contact pressure distribution remains unchanged for the life of the coating so that its worst-case lifetime can be estimated by dividing the coating thickness by the maximum linear wear rate.

Radius	**Coating Thickness**	**Estimated Lifetime**
mm	μm	Years
16	200	11.2
	400	5.8
25	200	11.6
	400	6.5

Table 5.7: Estimated lifetime of the high-modulus coatings

The 200μm coating predicts a lifetime that is nearly twice as long as the 400μm coating. These estimated lifetime values correspond to the period of time in which the elastic elements will be effective in providing the desired reaction force to the ball. Note that these estimates are

very conservative, as the contact pressure distribution will likely change as the ball 'wears in' to the coating surface. Adaptive meshing has shown that wear rates are initially high in implants and then decrease significantly after the bearing has worn in [33, 34]. It is therefore likely that these coatings will have lifetimes greater than the estimates in Table 5.7.

5.6 Wear results for the in-line design models

This section presents the results for the in-line design. A single low-modulus column is centered to contact the top of the ball and to provide the reaction force in the implant. As with the lateral design models, the wear results for this section are separated into two segments: models with elastic elements that are *not* coated and models employing elastic elements *with* coatings. Furthermore, each design type is further compared against its corresponding conventional model (MOP for uncoated elements, MOM for coated elements) for consistency.

5.6.1 Diameter variation study

A diameter $d_v$variation study is performed on this design in an effort to characterize the effect of d_v on the net reaction force provided by the elastic element. The in-line design is developed in this thesis and is not limited by the geometry of the cup, unlike the lateral design orientation. Moreover, the theory presented in Section 2.1.2 predicting e_0 for this design type assumes uniform compressive pressure on the column, which is not absolutely true for this sphere-on-flat contact. Since this design is not limited by cup geometry, the results of this study allow the selection of a d_v that provides the closest net reaction force to the predicted value of 350N. Note that these models are simulated without coatings.

Figures 5.11 and 5.12 display the linear wear distributions for the three d_v values simulated at both the 16mm and 25mm implant sizes, respectively. The diameter of each design is displayed below its respective plot. Note that the color/wear scheme remains constant in each figure (applying the range used for the d_v = 3.0mm case) so that the linear wear distributions for each implant size can be compared directly. Table 5.8 displays the contact and wear results for the diameter variation study. Each design assumes a predicted reaction force of 350N.

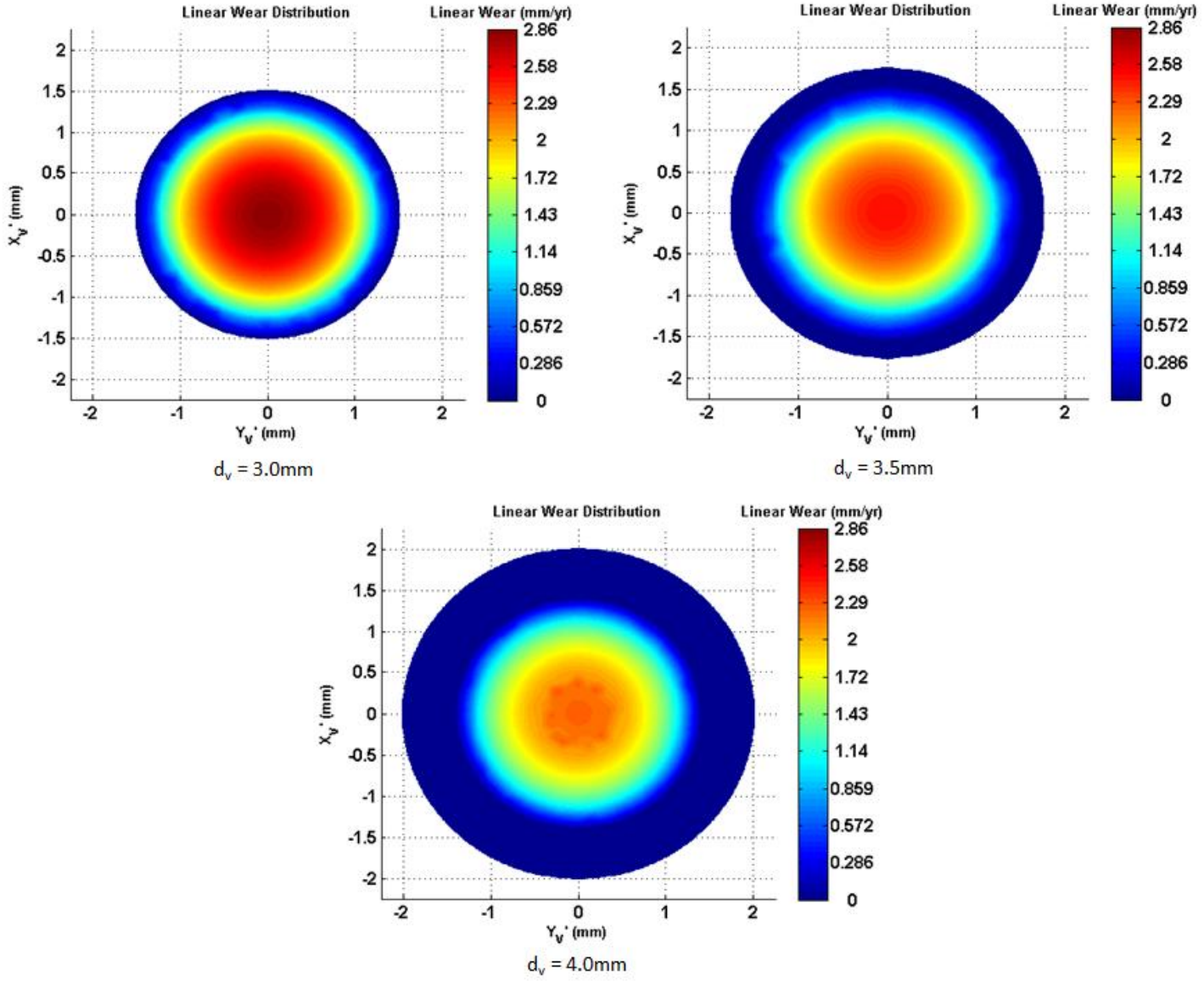

Figure 5.11: Linear wear distribution, in-line design configuration, 16mm

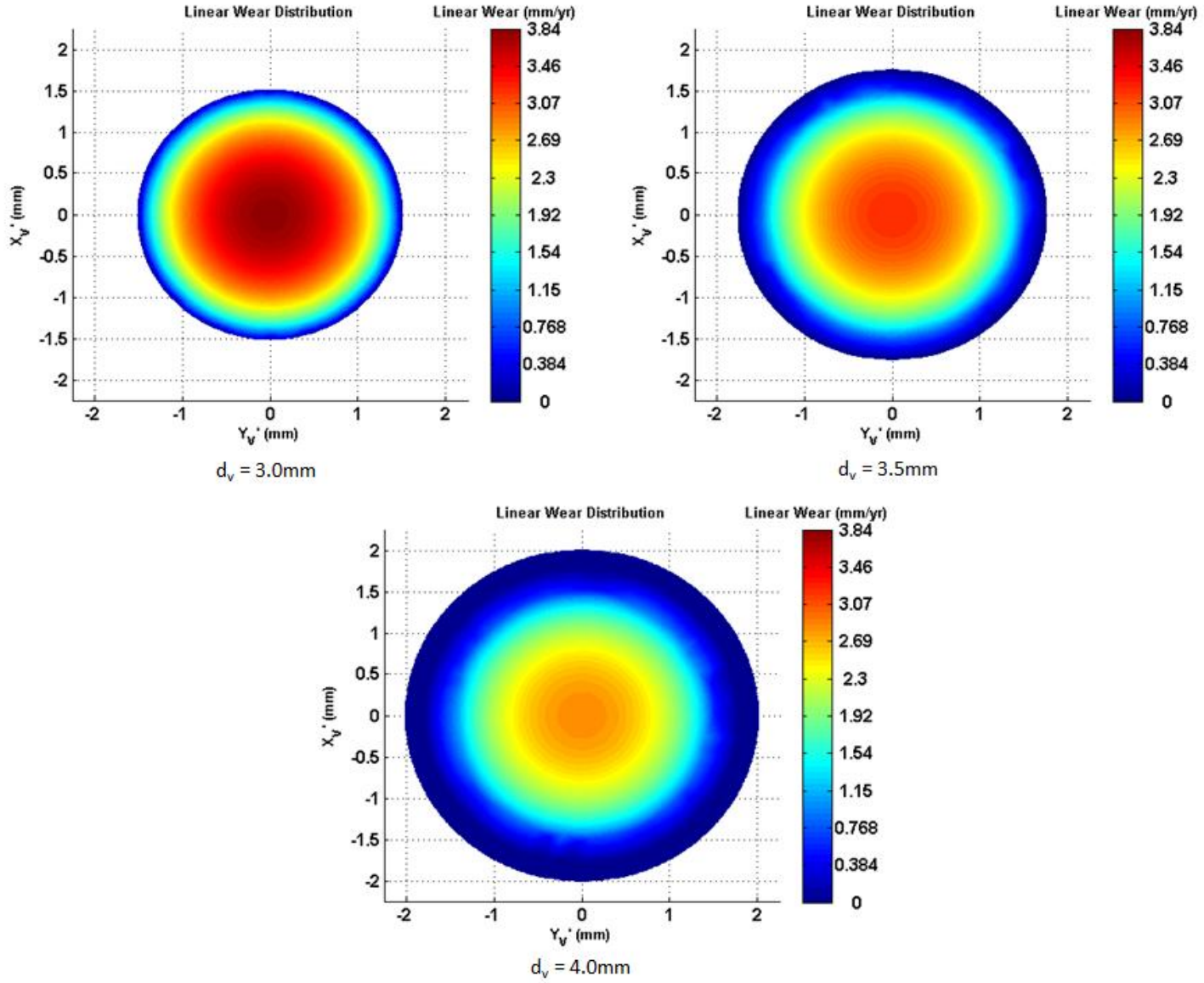

Figure 5.12: Linear wear distribution, in-line design configuration, 25mm

Radius	d_v	e_0	Peak Contact Pressure	Net Reaction Force	Linear Wear Rate	Volumetric Wear Rate
mm	mm	mm	MPa	N	mm/year	mm^3/year
16	3.0	-0.248	121.0	435.08	2.862	6.51
	3.5	-0.182	106.0	385.95	2.511	5.62
	4.0	-0.139	96.2	329.24	2.285	4.77
25	3.0	-0.248	104.0	460.60	3.840	16.24
	3.5	-0.182	87.8	425.41	3.257	14.81
	4.0	-0.139	77.7	375.42	2.883	13.57

Table 5.8: Diameter variation study results, uncoated elastic element

5.6.2 Models with high-modulus coatings

To keep consistent with the lateral orientation results, the best-case geometry is chosen from the diameter variation study to be simulated with high-modulus coatings. The 4.0mm diameter elastic element shows the closest agreement in terms of net reaction force with the predicted value of 350N. Additionally, this geometry performs better than the 3.0mm and 3.5mm diameter models in terms of linear and volumetric wear. Therefore the 4.0mm diameter model is further simulated with coating thicknesses of 200μm and 400μm.

Figures 5.13 and 5.14 show the linear wear distributions for the 200μm and 400μm coating thicknesses, respectively. Note that the 'ring' of higher contact pressure seen at the 200μm thickness for the lateral orientation is also present for this configuration. Table 5.9 displays the contact and wear results for the high-modulus coated models.

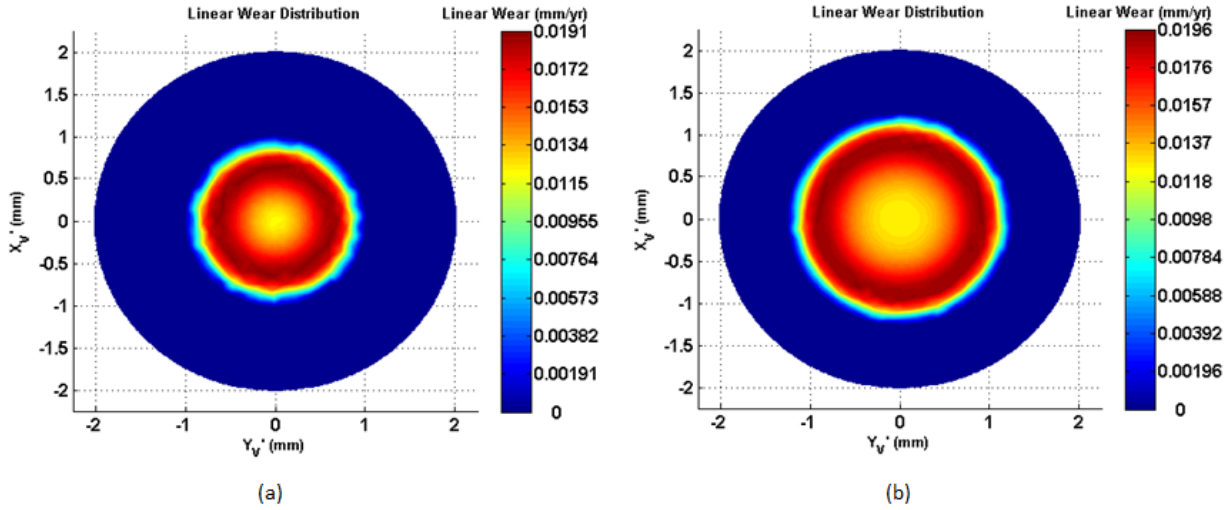

Figure 5.13: Linear wear distributions, 200µm coating; (a) 16mm, (b) 25mm

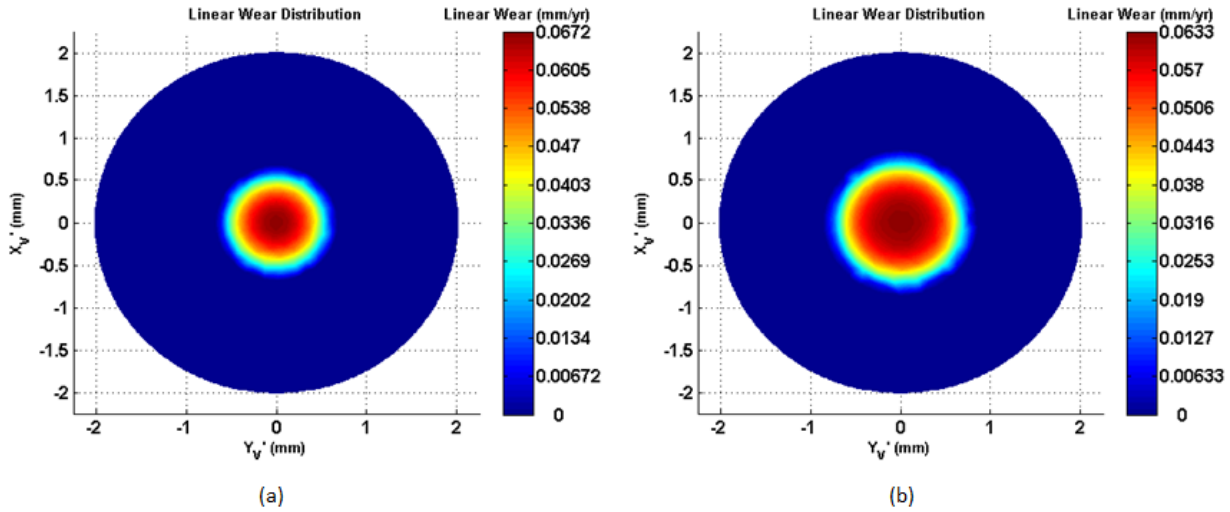

Figure 5.14: Linear wear distributions, 400µm coating; (a) 16mm, (b) 25mm

Radius	e_0	Coating Thickness	Peak Contact Pressure	Net Reaction Force	Linear Wear Rate	Volumetric Wear Rate
mm	mm	µm	MPa	N	mm/year	mm^3/year
16	-0.139	200	171.0	351.87	0.0191	0.036
		400	603.0	426.90	0.0672	0.043
25	-0.139	200	112.0	390.92	0.0196	0.064
		400	364.0	441.43	0.0633	0.070

Table 5.9: Summary of wear results, in-line configuration with coatings

5.6.3 Comparison with conventional models

Table 5.10 presents the results from Sections 5.6.1 and 5.6.2 compared against the wear results from the conventional models. The 'No Coating' designation signifies the 4.0mm diameter elastic element geometry presented in Section 5.6.1, meaning that each design in this comparison employs a 4.0mm diameter column and a predicted reaction force of 350N. Furthermore, the 'No Coating' case is compared directly against the MOP results for the conventional design, while the 200μm and 400μm cases are compared directly against the MOM results.

Radius	**Coating Thickness**	**In-line Design Models**		**Conventional Models**	
		Linear Wear Rate	**Volumetric Wear Rate**	**Linear Wear Rate**	**Volumetric Wear Rate**
Units	μm	mm/year	mm^3/year	mm/year	mm^3/year
16mm	No Coating	2.285	4.77	0.1298	46.20
	200	0.0191	0.036	0.0042	0.271
	400	0.0672	0.043		
25mm	No Coating	2.883	13.57	0.0971	80.47
	200	0.0196	0.064	0.0037	0.420
	400	0.0633	0.070		

Table 5.10: Comparison with conventional models

5.6.4 Comparison with lateral design models

It is also important to gauge the results of the in-line design against the results of the lateral design. The in-line orientation has the benefit of easier manufacturability and a simpler setup, but it also has only one elastic element to provide the reaction force, meaning less surface area is available to distribute contact pressure. Table 5.11 compares the wear results for the lateral and in-line novel designs.

Radius	Coating Thickness	In-line Configuration		Lateral Configuration	
		Linear Wear Rate	Volumetric Wear Rate	Linear Wear Rate	Volumetric Wear Rate
Units	μm	mm/year	mm^3/year	mm/year	mm^3/year
16mm	No Coating	2.285	4.77	2.165	14.26
	200	0.0191	0.036	0.0178	0.069
	400	0.0672	0.043	0.0692	0.070
25mm	No Coating	2.883	13.57	2.583	22.68
	200	0.0196	0.064	0.0172	0.112
	400	0.0633	0.070	0.0616	0.114

Table 5.11: Comparison with lateral design orientation

5.6.5 Discussion

The results for the uncoated low-modulus in-line design subjected to the diameter variation study show similar results to the lateral orientation: relatively high linear wear rates (when compared with the overall length of the columns) and somewhat lower volumetric wear rates compared with conventional models. The diameter variation study shows that these linear wear rates will decrease to some extent by using higher d_v values. Moreover, higher d_v values also result in net reaction loads that agree more favorably with the predicted value of 350N. Specifically, for the 16mm radius model the linear and volumetric wear rates decrease by 20.2% and 26.7%, respectively, between the 3.0mm and 4.0mm diameter models. The linear wear rates, however, are too large for extended life of the elastic column.

The in-line models that employ coatings show significantly improved linear and volumetric wear rates over the corresponding uncoated models. Similarly to the lateral orientation, the 200μm coating shows the best combination of low volumetric wear and reasonable linear wear when compared with conventional models. Linear wear rate is somewhat higher for this design compared with conventional models, but this coating thickness distributes the contact pressure in a unique 'ring' that keeps the peak pressures reasonable. For the 16mm model, the linear wear rates are 4.55 and 16.0 times greater than the MOM conventional design for the 200μm and 400μm coatings, respectively. For the 25mm model, the linear wear rates are 5.30 and 17.1 times greater than the conventional design for the 200μm and 400μm coatings,

respectively. The linear wear rates for this design are, however, comparable to those found using the lateral design (within 14.0% of each other for the 200µm coating and within 2.9% of each other for the 400µm coating).

The volumetric wear rates for the coated models show significant improvement over the conventional designs. The volumetric wear rates are 86.7% and 84.1% lower than the 16mm MOM conventional design for the 200µm and 400µm coatings and are 84.8% and 83.3% lower than the 25mm MOM conventional design for the 200µm and 400µm coatings, respectively. These wear rates are also lower than the lateral element orientation, primarily because there is only one elastic column in the in-line configuration. For the 16mm model, the volumetric wear rates are 47.8% and 38.6% lower than the lateral design orientation for the 200µm and 400µm coatings and are 42.9% and 38.6% lower than the 25mm lateral design for the 200µm and 400µm coatings, respectively.

Table 5.12 displays the estimated lifetime of the coatings for the in-line designs. The same assumptions regarding linear wear distribution made in Section 3.3.4 are also applied to these estimates.

Radius	**Coating Thickness**	**Estimated Lifetime**
mm	µm	years
16	200	10.5
	400	6.0
25	200	10.2
	400	6.3

Table 5.12: Estimated lifetime of the high-modulus coatings

The 200µm coating predicts a lifetime that is nearly twice as long as the 400µm coating, which is characteristic of the significantly higher contact pressures seen in the 400µm models. Since the linear wear rates are slightly higher for the in-line design than the lateral design, the estimated coating lifetimes are marginally shorter.

The in-line models with high-modulus coatings show measureable improvement over the conventional design, particularly in the level of volumetric wear per year. The wear results for these models are, however, very comparable to the results for the lateral design orientation. Linear wear rates are nearly identical, while volumetric wear improves for the in-line models

since there is only one elastic element. Furthermore, this configuration is less complex geometrically and would be easier and less expensive to manufacture.

5.7 Supplemental studies

5.7.1 Effect of friction

Generally frictional effects are ignored in Archard-based wear predictions. Surfaces are assumed to have a coefficient of friction of zero, which simplifies the wear formulation. Mattei *et al.* [57] recently published a MOM formulation that includes the effects of friction, though this approach is tied directly to the wear calculation itself. As this approach can complicate the wear prediction significantly, a simpler method is investigated in this work.

Using the built-in friction capabilities in ANSYS, the conventional and novel designs are simulated at a range of friction coefficients typically found in MOP implants. Brockett *et al.* [58] define this range between 0 and 0.065. The approach used in this work only characterizes the effect of friction on the contact pressure distribution (and its associated linear and volumetric wear rates), as the wear formulation is not changed to include friction. For the conventional designs, μ is varied between 0.01 and 0.065, as a nonzero coefficient of friction is required in these models for convergence. The novel designs (lateral configuration with no coating) are simulated through the full range with the exception of the $\mu = 0.065$ case for the 16mm radius model, where convergence could not be obtained. Tables 5.13 and 5.14 display the results of the friction study for the conventional and novel designs, respectively.

Radius	μ	Linear Wear Rate	Volumetric Wear Rate
16	0.010	0.1298	46.20
	0.020	0.1286	46.21
	0.040	0.1282	46.91
	0.065	0.1278	45.74
25	0.010	0.0971	80.47
	0.020	0.0970	80.08
	0.040	0.0971	80.02
	0.065	0.0970	79.74

Table 5.13: Effect of friction, conventional models; C_0 = 40μm

Radius	μ	Peak Contact Pressure	Net Reaction Force	Linear Wear Rate	Volumetric Wear Rate
mm	-	MPa	N	mm/year	mm^3/year
16	0.000	91.2	306.39	2.165	14.26
	0.010	92.1	312.76	2.187	14.34
	0.020	94.5	318.85	2.244	14.69
	0.040	93.5	339.22	2.221	14.47
	0.065	-	-	-	-
25	0.000	69.6	304.52	2.583	22.68
	0.010	67.3	310.65	2.498	23.02
	0.020	69.2	316.45	2.568	23.57
	0.040	69.8	329.42	2.589	23.44
	0.065	71.3	346.29	2.644	23.51

Table 5.14: Effect of friction, lateral design models with no coating

The results for both the conventional and novel designs show that linear and volumetric wear rates are insensitive to the coefficient of friction chosen with the stated range. The net reaction force calculated by ANSYS for the novel design models increases as the coefficient of friction increases, as there is a greater shear component on the elastic elements due to friction as μ becomes larger. Otherwise, this study shows that frictional effects can be safely neglected when approached in this manner.

5.7.2 Effect of radial clearance

The effect of radial clearance on conventional implant designs has been studied more extensively than friction. In wear studies where adaptive meshing is applied to the FE models, long-term linear and volumetric wear are shown to be insensitive to radial clearance values less than 500μm in MOP implants [33, 34]. Initial wear rates, however, are shown to be higher for designs with larger clearances until the bearing has worn in and these wear rates become comparable.

Applying a similar range of clearances studied by Maxian *et al.* [33], Table 5.15 summarizes the results of this study. As the meshes are not updated based on wear results in this work, the results are expected to mirror the trends seen for the initial wear rates in the adaptive wear papers. Note that this study is only applied to the 16mm radius MOP design.

Radial Clearance	**Linear Wear Rate**	**Volumetric Wear Rate**
μm	mm/year	mm^3/year
40	0.1298	46.20
100	0.1820	48.57
200	0.2523	49.06

Table 5.15: Effect of radial clearance, conventional design

The results show that linear wear rate increase as the radial clearance becomes larger in the bearing. This is consistent with the initial wear rates published by Maxian *et al.* [33] and Kang *et al.* [34]. It is interesting that the volumetric wear rates show only a slight increase over the same range. This can be explained through the contact pressure distribution: the contact region is larger at smaller clearances and therefore characterized by a lower peak contact pressure; however, the contact region is smaller at the larger clearance values, leading to a higher peak contact pressure distributed over a smaller area. This characteristic is shown in Figure 5.15, which displays the contact distributions for each clearance at the peak loading condition. Although the peak pressures (and subsequently the linear wear rates) are significantly higher for the larger clearances, the volumetric wear rates stay largely unaffected because the distribution of contact pressure reflects the loading of the implant, which remains unchanged between cases.

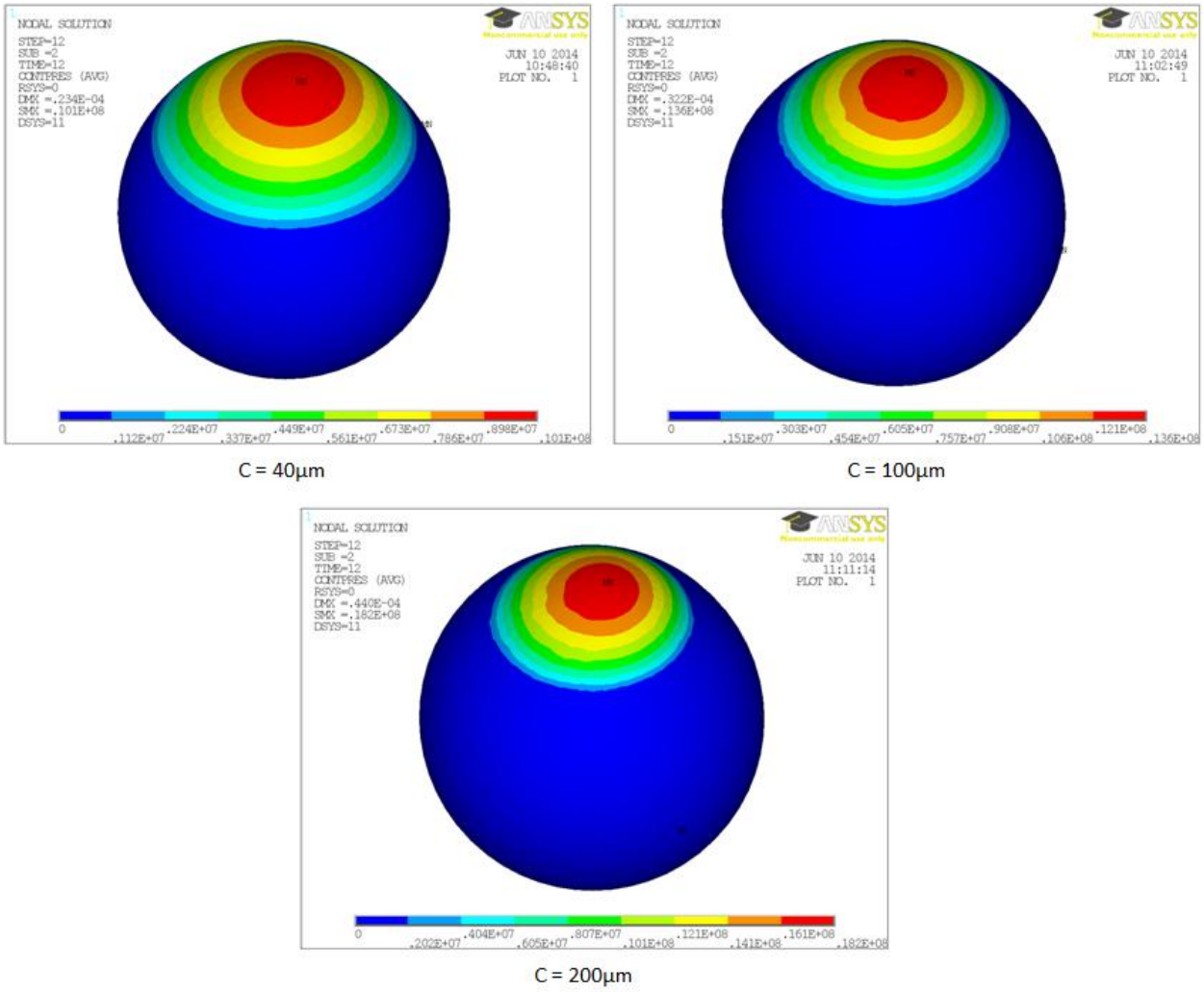

Figure 5.15: Contact pressure distributions, conventional models

5.7.3 Effect of ellipticity

The effect of cup ellipticity on the wear of hip implants has not been studied, though research characterizing the lubrication behavior in nonspherical implants has been published [11-13]. The specific application of ellipticity in the novel design – where the major axis of the ellipsoid of revolution is oriented in the +Z-direction – is unique and warrants further characterization from a wear perspective. This study quantifies the effect that the ellipticity parameter δ has on linear and volumetric wear rates and compares these results with the conventional models presented in Section 5.4.

Two ellipticity values are simulated – 40μm and 100μm – for both MOP and MOM models at the 16mm radius size. These models employ the same geometric parameters as the conventional models with the exception that they have an ellipsoidal cup and use a radial clearance value that matches their respective ellipticity parameter. Table 5.16 displays the wear results for the ellipticity study. Furthermore, Figures 5.16 and 5.17 show the linear wear distributions for the MOP and MOM models, respectively. Note that the results for the δ = 0μm case are taken from the conventional model results presented in Section 5.4.

Model Type	**Ellipticity**	**Nominal Radial Clearance**	**Linear Wear Rate**	**Volumetric Wear Rate**
Units	μm	μm	mm/year	mm^3/year
MOP	0	40	0.1298	46.20
	40	40	0.1227	52.85
	100	100	0.1647	52.19
MOM	0	40	0.0042	0.271
	40	40	0.0027	0.260
	100	100	0.0047	0.252

Table 5.16: Effect of ellipticity, 16mm radius

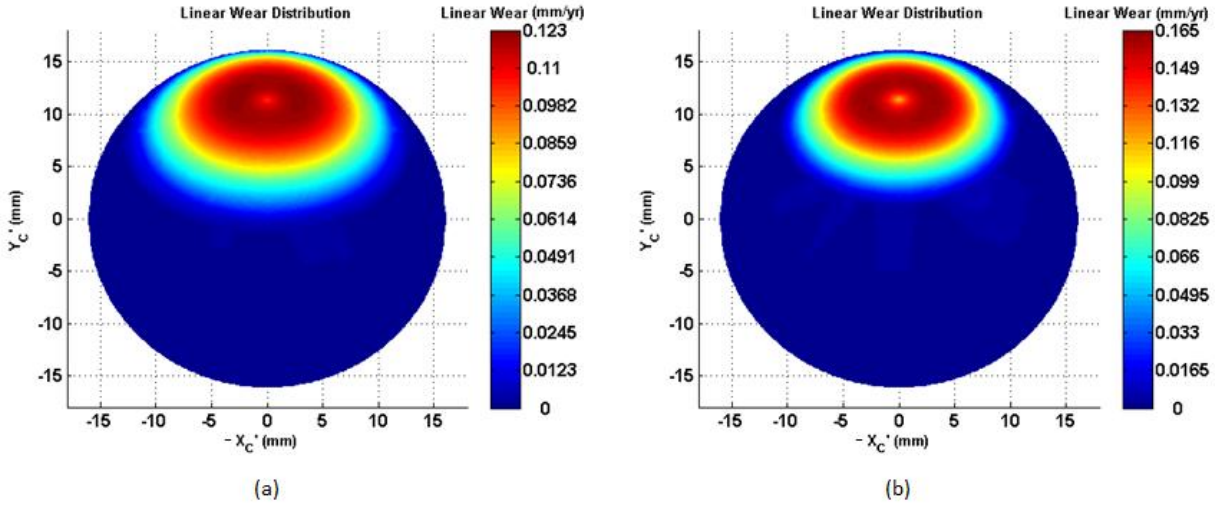

Figure 5.16: Linear wear distribution, MOP ellipticity study; (a) δ = 40μm, (b) δ = 100μm

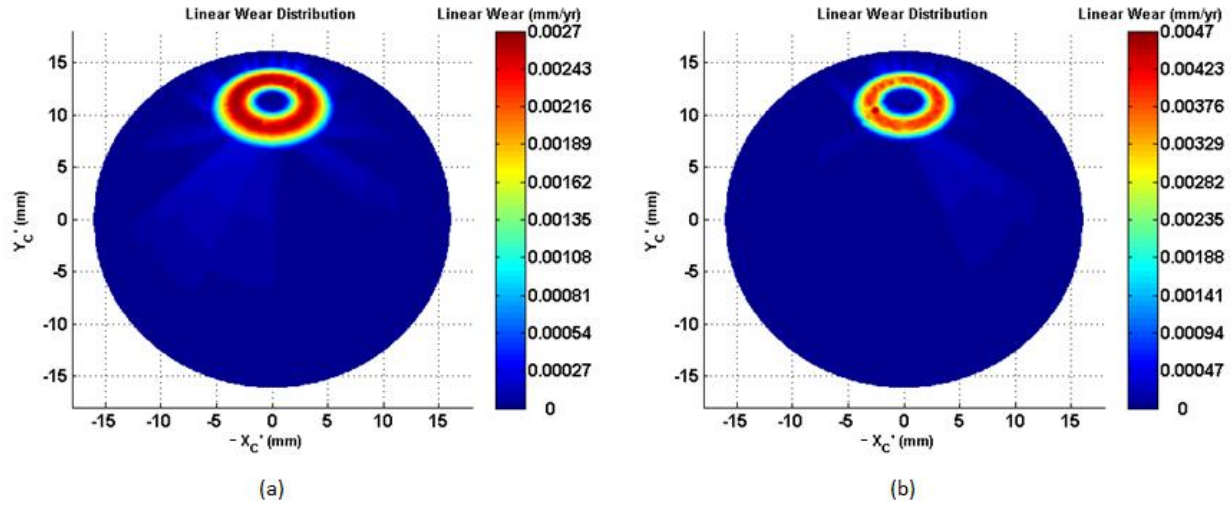

Figure 5.17: Linear wear distribution, MOM ellipticity study; (a) δ = 40μm, (b) δ = 100μm

The results for this study are characteristic of the line contact approach to design employed by Boedo and Booker [24]. An annular ring of higher linear wear surrounds an area at the pole (location of maximum ellipticity) with lower linear wear. This phenomenon is decidedly more pronounced for the MOM models, as the cup material does not deform to distribute the contact pressure over a greater area as is seen for the MOP models.

The linear wear results for the δ = 40μm case are expectedly lower than for the δ = 100μm, as there is more pronounced line contact in the model employing larger ellipticity. It is interesting to note that the volumetric wear rates are very comparable for both ellipticity values. The same loading (according to the ISO 14242 standard) is applied to both model types, it is just distributed differently in each case. As such, the volumetric wear rates should be expected to be similar in magnitude. The ellipsoidal cup simulations show comparable wear rates to the conventional designs presented in Section 5.4. There is a slight decrease in linear wear rates for the δ = 40μm cases and a slight increase in linear wear rates for the δ = 100μm. Volumetric wear rates are comparable for both ellipticity values to the conventional design.

This study shows that an ellipsoidal cup geometry significantly affects the contact region by producing an annular ring of increased linear wear that is characteristic of the line contact design strategy applied by Boedo and Booker [24]. A larger contact region as seen for the ellipsoidal models may be preferred to a point contact design (perfectly spherical implant), as linear wear rates can be lower for certain ellipticity values and volumetric rates are similar.

Chapter 6: Summary and Conclusions

This thesis has presented an investigation of the lubrication behavior and wear characteristics of a novel total hip replacement design. The key features of the novel design include a mechanical means of providing an elastic load to enact separation of ball and cup and an ellipsoidal cup geometry that promotes squeeze-film action over wedge-film action. Two implant design configurations were analyzed: the lateral design, which employs two elastic elements that contact the ball through a set of slots machined into the cup; and the in-line design, which employs a single elastic element oriented vertically through a clearance hole in the cup.

It has been found that the lubrication behavior for the lateral design configuration shows significant improvement over conventional implant designs; significantly larger minimum film thicknesses and significantly smaller maximum film pressures were predicted for the lateral design over the stance phase portion of the gait cycle. Similarly favorable results were predicted for the in-line design configuration if a sealed boundary (no flow) is assumed between the clearance hole and the elastic element. Optimal design specifications for the stance phase portion of the gait cycle are characterized by ellipticity values that are greater than the nominal radial clearance of the implant (to promote circular line contact over point contact) and nominal clearance values that are much larger than those employed in conventional designs.

Of similar importance is the lubrication behavior during the swing phase, in which the elastic elements provide a reaction force to the ball to enact separation of the bearing surfaces. After a cavitation region is formed at the start of the swing phase, it has been found that the reformation of a complete lubricant film is possible before the start of the stance phase. The analysis of the lateral design configuration shows full-film reformation over a significantly large range of ball velocities, cavitation threshold pressures, and initial ball positions that are likely to occur in practice. Though refill times were marginally longer for the in-line design (assuming a sealed boundary condition) than the lateral design, full-film reformation was also predicted over a similarly significant range of implant conditions. While the ellipticity value has a substantial effect on the stance phase bearing performance, it is of lesser importance during the swing phase.

This thesis employed a well-documented sliding-distance-coupled wear formulation to characterize the wear of the elastic elements during the gait cycle. Significant improvement in volumetric wear rates over conventional designs was predicted for both the lateral and in-line

design configurations employing low-modulus elastic columns. Linear wear rates, however, were large compared with the length of the elastic columns and would cause deterioration of design functionality over the life of the implant. As such, an investigation of high-modulus coatings coupled with low-modulus elastic elements has shown significant improvement in volumetric wear rates over conventional designs while predicting manageable linear wear rates that allow for extended life of the implant.

Further work on this subject will include a more comprehensive study of coating thicknesses and coating materials with the current design configurations to better understand the unique contact regions predicted for the coated models. On a related note, additional designs employing elastic action should be investigated; especially ones that marginally increase contact area between the ball and elastic elements and provide additional mechanical stability to the implant. Specifically, designs that employ more than two elastic columns in a similar orientation to the lateral configuration would provide a practical balance of improved distribution of contact pressures and enhanced stability. Furthermore, it may be desirable to modify the orientation of the elastic elements to allow easier access specifically to these columns; a minimally invasive revision surgery to replace these components of the design would prevent the need for full revision of the implant and could allow extended life beyond the predictions in this thesis.

Additional investigation of lubrication behavior and wear characteristics over a wider range of gait cycle conditions may be necessary; the ISO 14242 standard is widely accepted and specifies a conservative gait cycle, but it is not representative of all hip replacement patients. Further work may also include the adoption of adaptive-meshing contact algorithms that more accurately capture contact mechanics by updating the bearing surfaces to reflect the changes in conformity that occur during the wearing-in of the implant.

This thesis presents a feasible alternative to conventional designs with considerable improvement in lubrication characteristics and a reduction in wear rates. Future prototyping and wear testing of the presented designs are a logical extension of this research and will be necessary for the future acceptance of this design concept in the biomedical community.

Appendix A

A.1 Finite element models

To validate the finite element methods, contact options, and wear programs, a variety of analyses are performed and compared with published results in literature. A logical progression of validation is followed: first, simplified finite element geometries are compared with the Hertzian model for contact stress to validate the method of analyzing contact stresses; second, more complex implant geometries are analyzed and compared with published results for similar and/or identical cases; and third, wear results for these complex implant geometries are compared with published results to validate the wear program used. The following section describes the step-wise validation progression in its entirety, including the procedure for mesh generation and refinement.

A.1.1 Sphere-on-plane

Figure A.1 shows the FE model used to analyze the sphere-on-plane case. The material of the ball is assumed to be identical to that of the ball used in the novel and conventional implant designs, while the material of the planar volume is assumed to be identical to that of the polyethylene used in the MOP conventional geometries. The Z_{A1} axis passes through the center of the planar volume.

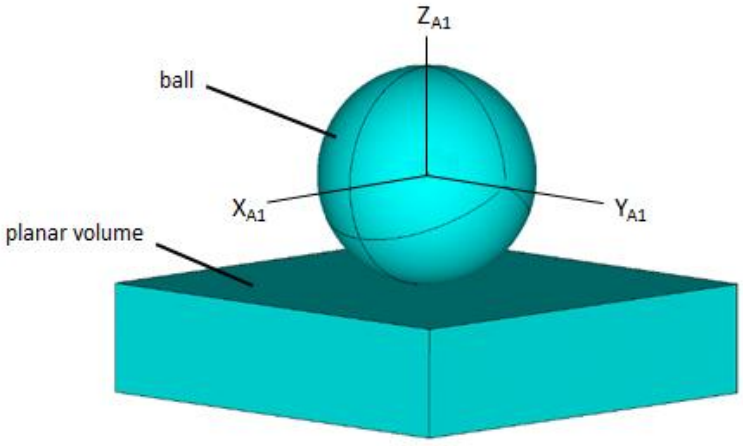

Figure A.1: Sphere-on-plane FE model

It is now appropriate to briefly outline the Hertzian contact theory applied in this work. There are number of assumptions that need to be made for spherical Hertzian contact: (1) the strains must be small and within the elastic limit of the materials; (2) the contact surfaces must be continuous and non-conforming; (3) each solid must be considered an infinite half-space; and (4) both surfaces must be considered frictionless. Assumptions (1), (2) and (3) can be synthesized to a single principle: the contact radius a must be much smaller than the effective radius of curvature R^* of the contact surfaces. As such, pure Hertzian contact theory is somewhat limited in its application to real-world geometries, though it does prove an important tool for comparison when these conditions are generally met.

The Hertzian contact radius a is represented by:

$$a = \left[\frac{3PR^*}{4E^*}\right]^{1/3} \tag{A.1}$$

where P is a constant, normal load applied to the surfaces; R^* is the effective radius of curvature of the contact surfaces described as Equation A.2; and E^* is the effective modulus of elasticity of the contact surfaces described as Equation A.3.

$$R^* = \left[\frac{1}{R_1} - \frac{1}{R_2}\right]^{-1} \tag{A.2}$$

$$E^* = \left[\frac{1-{\nu_1}^2}{E_1} - \frac{1-{\nu_2}^2}{E_2}\right]^{-1} \tag{A.3}$$

where R_1 and R_2 are the respective radii of the contact surfaces; ν_1 and ν_2 are the respective Poisson's ratios; and E_1 and E_2 are the respective moduli of elasticity. Using the solution for contact radius a, expressions can be found for contact penetration δ and contact pressure p_0:

$$\delta = \frac{a^2}{R^*} \tag{A.4}$$

$$p_0 = \frac{3P}{2\pi a^2} \tag{A.5}$$

The following contact options are used for all three-dimensional (3D) contact analyses in this Appendix, unless otherwise specified. 10-node SOLID186 tetrahedral elements are used to mesh the geometry, while CONTA174 and TARGE170 are used for the Contact and Target surfaces respectively. The default Augmented Lagrangian convergence algorithm is chosen, where the ball surface is consistently chosen as the Contact and the cup surface is consistently chosen as the Target. Default values for surface stiffness (FKN and FKT) are chosen. The procedure for the formation of the FE mesh is discussed in Section A.1.5 and is applied consistently to each geometry.

It should be noted that the FE model used for this sphere-on-plane validation does not assume infinite half-spaces for the contact regions. Specifically, the planar volume has a finite thickness t_{plane} of 8mm and side length S_{plane} of 32mm, which is a major reason for any discrepancies between the theory and FE analysis. For planar contact surfaces, the radius of curvature is set to infinity in the Hertzian calculation. The bottom area of the planar volume is considered fixed and the load P is applied in the $-Z_{A1}$-direction on the center of the ball, allowing displacement only in the Z_{A1}-direction. The meshes used for the contact regions are shown in Figure A2, while the geometric parameters for this model are listed in Table A.1.

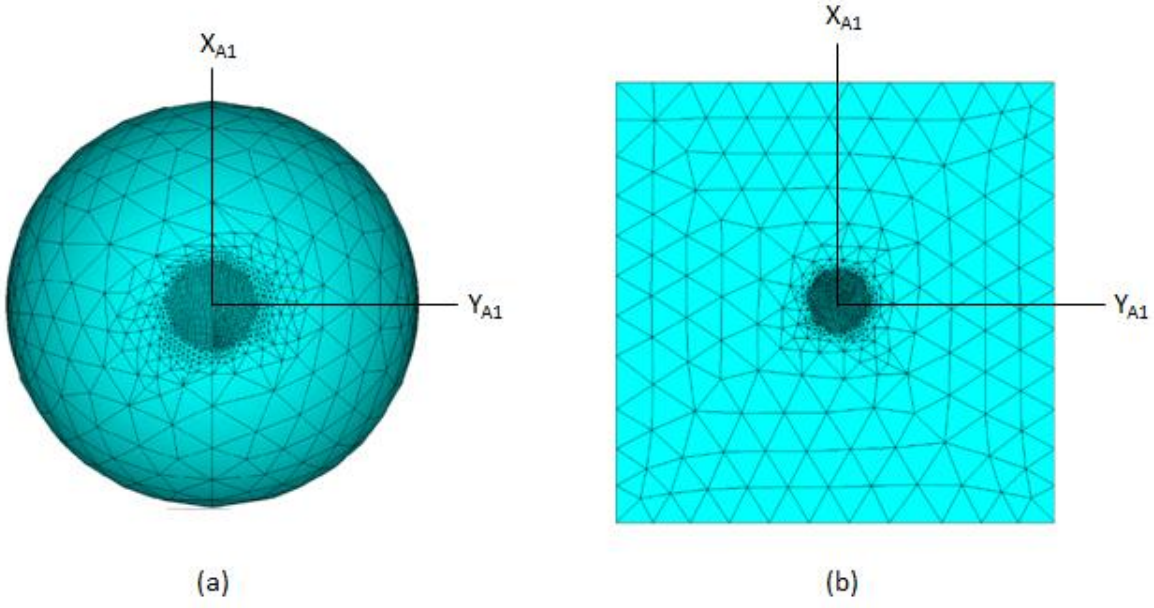

Figure A.2: FE meshes for sphere-on-plane model

Parameter	R_{sphere}	R_{plane}	S_{plane}	t_{plane}	E_{sphere}	E_{plane}	ν_{sphere}	ν_{plane}	P
Units	m	m	m	m	GPa	GPa	-	-	N
Value	0.016	∞	0.032	0.008	210	1.4	0.31	0.46	1000

Table A.1: Geometric parameters for sphere-on-plane FE model

Table A.2 lists the comparison between FE results and Hertzian theory. There is general agreement in the results, validating that the contact options used in the FE model (in which mesh density plays an important role) can be applied to more complex geometries. It should also be noted that using Load Control (LC) and the combination Displacement-Load Control (DLC) methods for solving contact problems provide nearly identical results. Standard, Bonded and Rough surface behavior options are also simulated and show agreement; the latter two options assume an infinite friction coefficient to prevent sliding of the surfaces and result in faster convergence. A representative plot of contact pressure distribution is shown in Figure A.3 for the Standard LC case.

Case	Method	Peak Contact Pressure	Maximum Penetration	Contact Radius
Units	-	MPa	μm	mm
Hertzian	Theoretical	132.9	224.5	1.90
Standard	LC	126.0	196.0	1.87
Standard	DLC	129.0	196.0	1.87
Bonded	DLC	129.0	196.0	1.87
Rough	DLC	129.0	196.0	1.87

Table A.2: Sphere-on-plane FE results compared with Hertzian theory

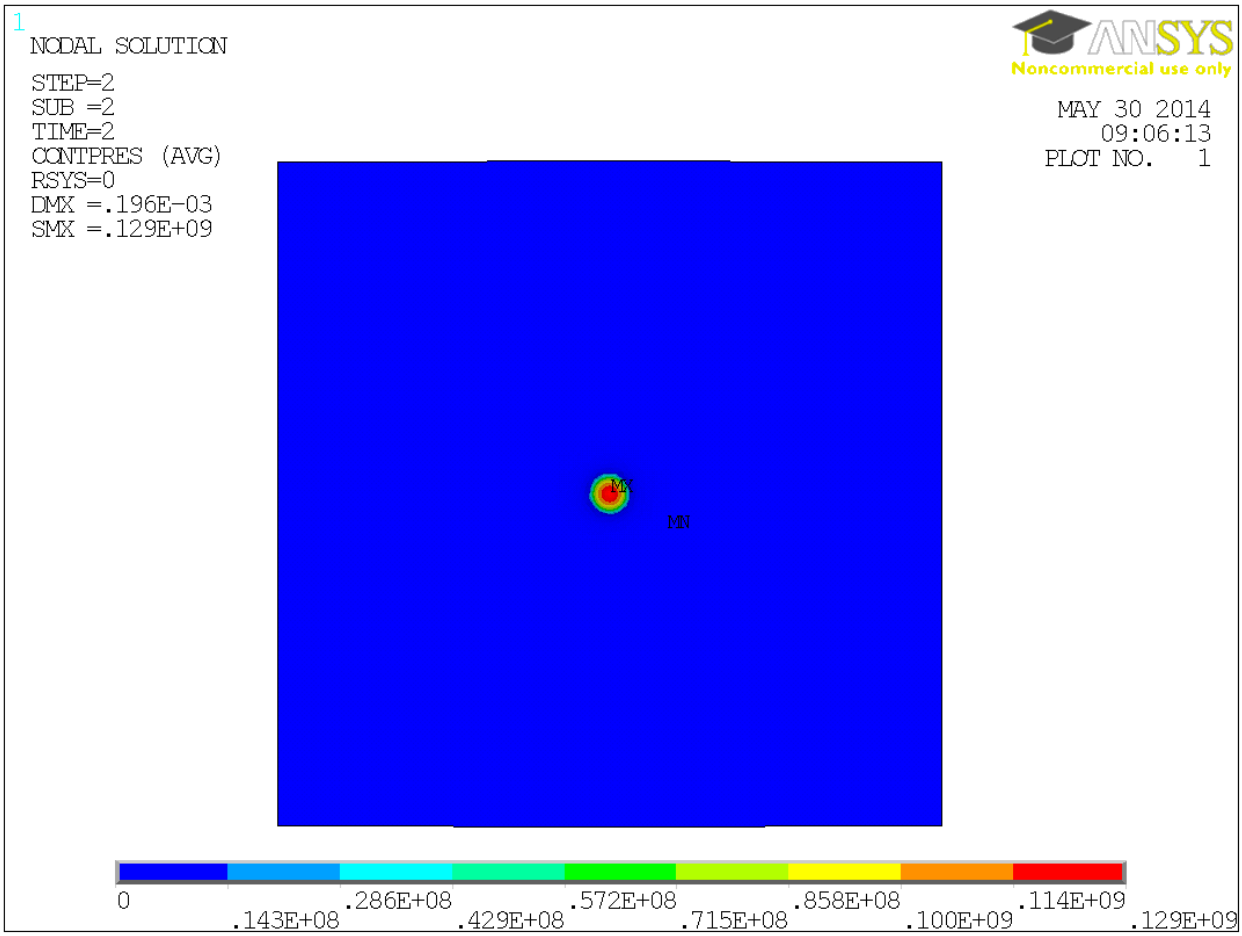

Figure A.3: Contact pressure distribution, Standard LC case

A.1.2 Sphere-on-cup

The second step in validation is to analyze a more complex geometry that is still generally Hertzian in nature. Figure A.4 shows the model used for this simulation and Figure A.5 shows the mesh density on the contact surfaces. Both the spherical ball and cup are assumed to have identical material properties that correspond to the cobalt-chrome material used elsewhere in this work. As both materials have generally high moduli of elasticity, the contact region remains small compared with the effective radius of curvature of the surfaces.

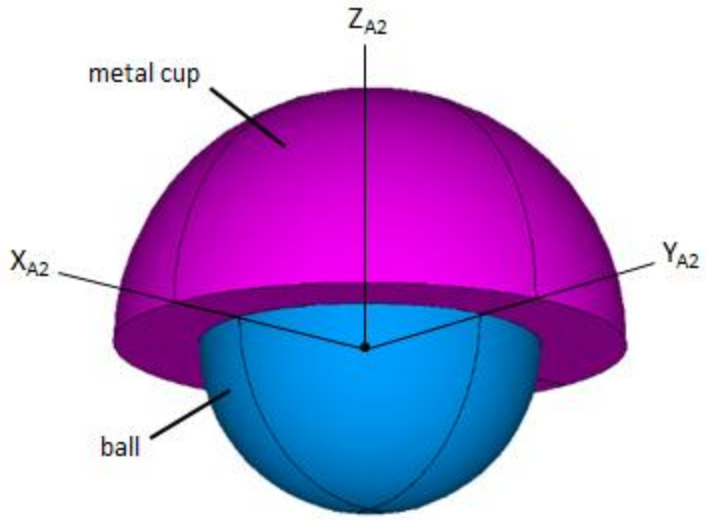

Figure A.4: Sphere-on-cup FE model

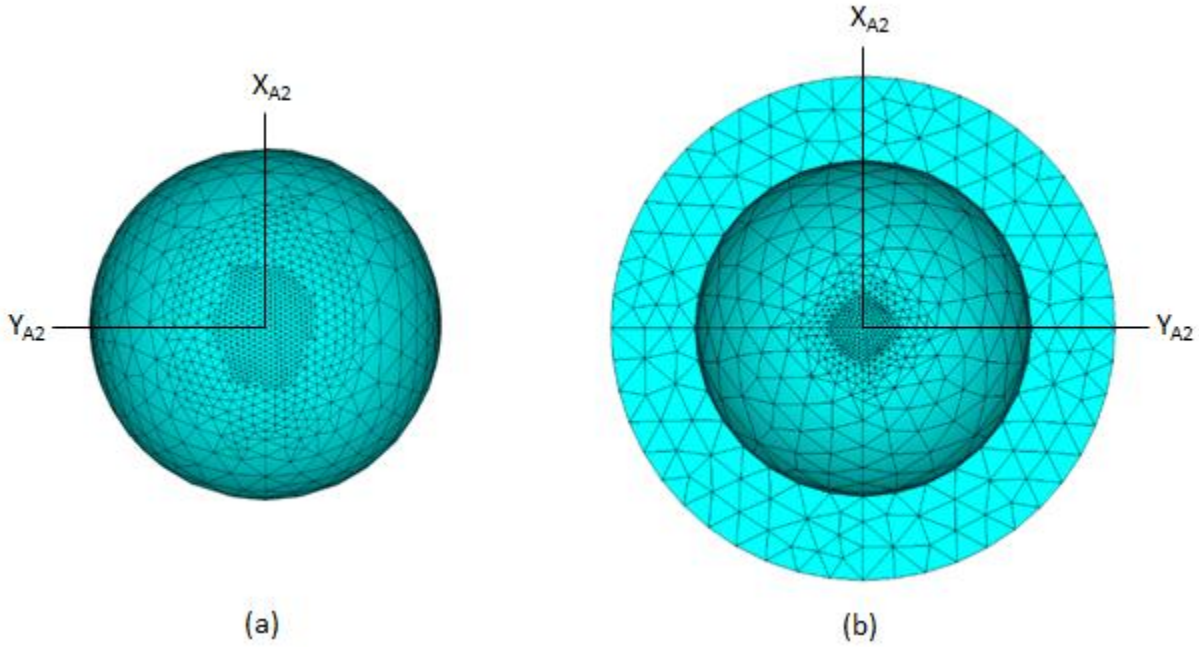

Figure A.5: FE meshes for sphere-on-cup model

As with the sphere-on-plane model, this simulation does not assume infinite half spaces. The inclination angle in this model is set to 0° in an effort to keep the problem as close to Hertzian as possible. As such, the Z_{A2} axis is oriented along the cup polar axis. The radial clearance C between the contact surfaces is 40μm. The back area of the cup is considered fixed

and the load P is applied in the $+Z_{A2}$-direction. It should be noted in Hertzian theory than a concave surface (such as the cup used in this model) is assumed to have a 'negative' radius of curvature R_{cup}. Table A.3 shows the parameters used for the FE model.

Parameter	**R_{sphere}**	**R_{cup}**	**C**	**t_{cup}**	**E**	**ν**	**P**
Units	mm	mm	μm	mm	GPa	-	N
Value	15.960	-16.000	40	8	210	0.31	1000

Table A.3: Geometric parameters for sphere-on-cup FE model

The results of this validation study are recorded in Table A.4. Every simulation is completed using Displacement-Load Control, required due to the concave nature of the contact surfaces. The FE results show general agreement with the Hertzian approximation, with the most significant differences appearing in contact penetration. It is likely that these differences can be attributed the finite thickness of the cup surface. There is again little difference between Standard, Bonded and Rough surface behavior options. This study validates the chosen contact options and FE model development procedures when applied to Hertzian concave geometries similar to the conventional designs simulated in this work. A representative contact pressure distribution plot is shown in Figure A.6 for the Standard element case.

Case	**Method**	**Peak Contact Pressure**	**Maximum Penetration**	**Contact Radius**
Units	-	MPa	μm	mm
Hertzian	Theoretical	39.9	1.87	3.45
Standard	DLC	39.0	0.64	3.64
Bonded	DLC	39.0	0.64	3.40
Rough	DLC	38.9	0.64	3.33

Table A.4: Sphere-on-cup FE results compared with Hertzian theory

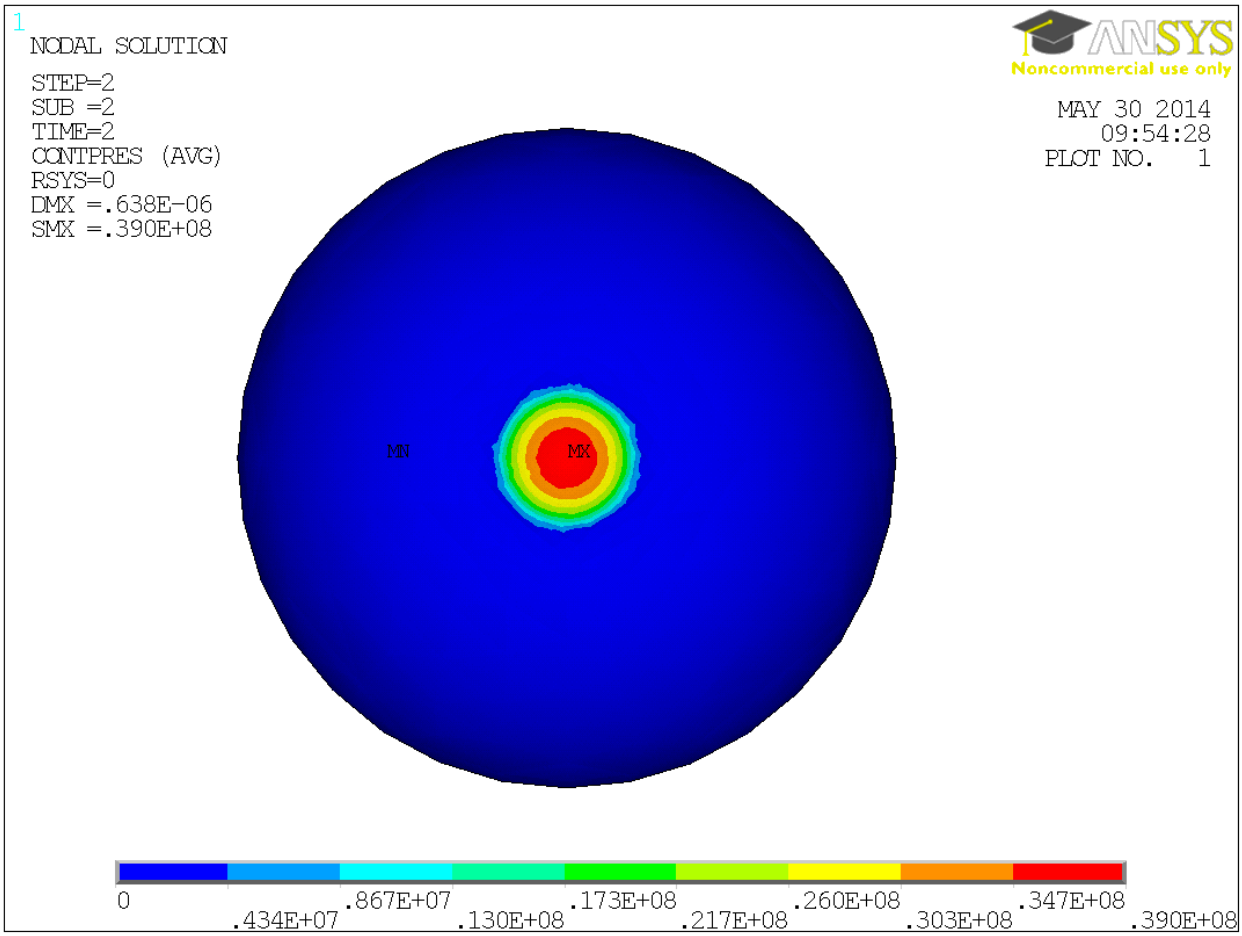

Figure A.6: Contact pressure distribution, Standard case

A.1.3 Axisymmetric models

Mattei *et al* recently published two papers regarding wear prediction in MOP [32] and MOM [57] implants. The former provides a detailed review of the FE procedure used to estimate contact pressures for the hip implant geometries in that work. The FE model is further used to create an analytic expression that can be applied to multiple geometries so that the authors do not have to analyze an FE model for each case. This section compares the approach used in this thesis with the methods applied by Mattei *et al*. [32, 57]

A simplified two-dimensional (2D) FE model is used in the MOP paper employing the axisymmetric element behavior option in ANSYS. This necessitates that only a quarter of the

implant is modeled. The external side of the cup is considered fixed and the load is applied as a pressure distributed on the mid-side surface of the ball. Furthermore, the cup is modeled with an inclination angle of 0° and frictionless contact is assumed for all simulations. This model is subsequently used to form an analytic expression relating contact pressure to location on the cup surface. It should be noted that this is a simplified approach to hip implant simulation that may not fully capture the more subtle effects of implant orientation and multi-directional loading but is extremely efficient from a computing standpoint. The geometric parameters used by Mattei *et al.* [32] and therefore in this validation study are listed in Table A.5, where the subscript *fh* refers to femoral head (ball) and parameter P_0 refers to the net load in the $+Y_{A3}$-direction due to the distributed pressure along the mid-side line of the ball.

Parameter	$\mathbf{R_{fh}}$	$\mathbf{R_{cup}}$	**C**	$\mathbf{t_{cup}}$	$\mathbf{E_{fh}}$	$\mathbf{E_{cup}}$	$\boldsymbol{\nu_{fh}}$	$\boldsymbol{\nu_{cup}}$
Units	mm	mm	μm	mm	GPa	GPa	-	-
Value	13.920	14.000	80	8	210	0.5	0.30	0.40

Table A.5: Geometric parameters for axisymmetric model

The FE model used in this work is shown in Figure A.7. Note that the external surface of the cup is fixed and the Y_{A3}-axis is aligned with the cup polar axis. The axisymmetric approach requires the axis of symmetry to be the Y-axis in the built-in coordinate frame in ANSYS. Three values are used for P_0 (1000N, 2000N and 3000N) within the range of values simulated in Mattei *et al.* [32]. Due to the nature of the 2D asymmetric approach, the 'line' pressure P is calculated by dividing the net load P_0 by the area of the mid-side of the femoral head, as this pressure is assumed to be revolved about the Y_{A3} axis during simulation:

$$P = \frac{P_0}{\pi {R_{fh}}^2} \tag{A.6}$$

Load Control is used to run the model, applicable because of the simple 2D geometry and fine mesh. Furthermore, a mesh sensitivity analysis shows that the mesh used agrees within 1.0% (for peak contact pressure and maximum penetration) of models with further mesh refinement.

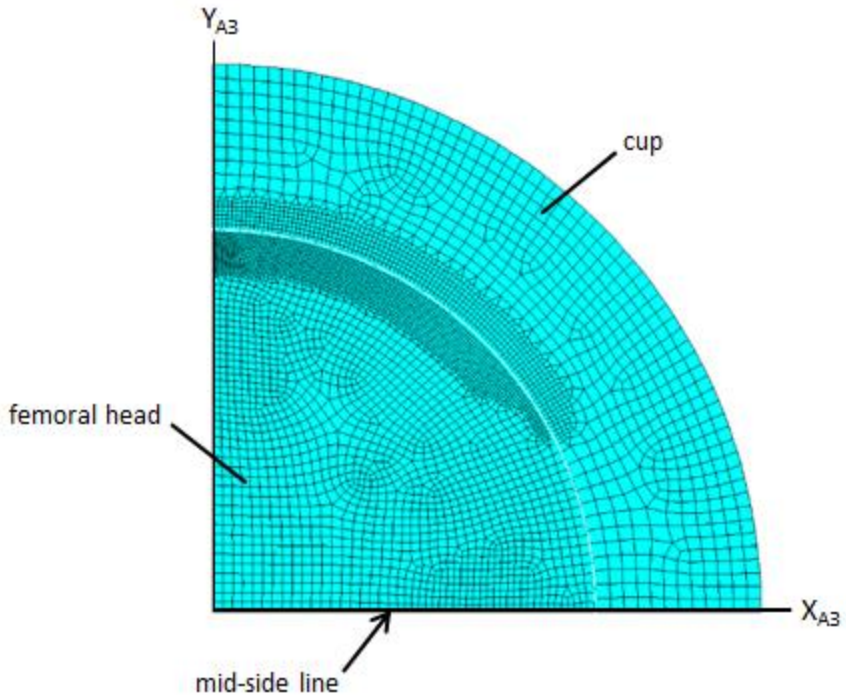

Figure A.7: Asymmetric FE model and mesh density

In addition to the axisymmetric simulations, a 3D model with the same geometric parameters is run to compare the axisymmetric approach with a full FE model. Figure A.8 shows the 3D model; note that the coordinate system is identical to that used in Figure A.5 for consistency. The Standard surface behavior option is chosen for these runs at the same three load values, though the load is applied as a point load in the $+Y_{A3}$-direction at the center of the ball due to convergence issues with 3D pressure loads. The mesh density applied for this model is shown in Figure A.9 and is created using the same procedure used to mesh the conventional models detailed in this work.

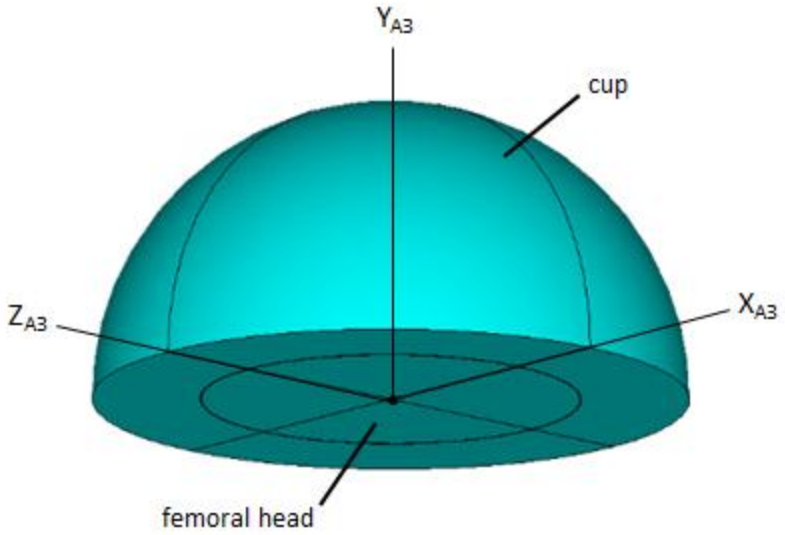

Figure A.8: 3D model for comparison with asymmetric simulations

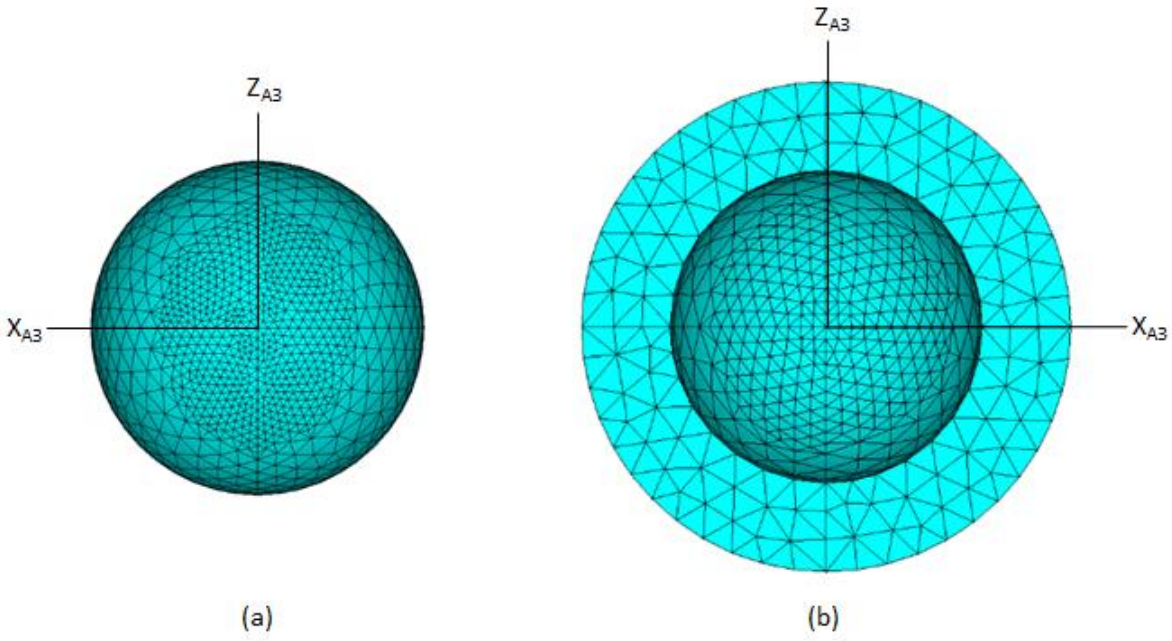

Figure A.9: FE meshes for 3D model

Table A.6 displays the results from both the 2D asymmetric and the 3D full model simulations and compares the peak contact pressures to the results provided by Mattei *et al.* [32]. The 2D results found in this study are slightly lower when compared with the results in the

paper, though the 2D and 3D results in this work show consistency with one another even with the difference in application of the loading. The slightly lower values found in this work can likely be attributed to differences in mesh density, initial penetration in the 2D model, and/or element type used, as the authors do not provide this information. Additionally, Figures A.10 and A.11 show the contact pressure distribution for the P_0 = 1000N case.

Parameter	**Units**	**P_0 = 1000N**		
		Mattei [32]	**2D Model**	**3D Model**
Peak Contact Pressure	MPa	6.5	5.20	4.84
Maximum Penetration	μm	-	41.7	38.8
Contact Radius	mm	-	10.20	10.66
Parameter	**Units**	**P_0 = 2000N**		
		Mattei [32]	**2D Model**	**3D Model**
Peak Contact Pressure	MPa	10.2	8.27	7.76
Maximum Penetration	μm	-	66.1	81.8
Contact Radius	mm	-	11.88	11.74
Parameter	**Units**	**P_0 = 3000N**		
		Mattei [32]	**2D Model**	**3D Model**
Peak Contact Pressure	MPa	13.0	11.0	10.4
Maximum Penetration	μm	-	88.1	116.0
Contact Radius	mm	-	12.32	12.10

Table A.6: Comparison of 2D and 3D results to [32]

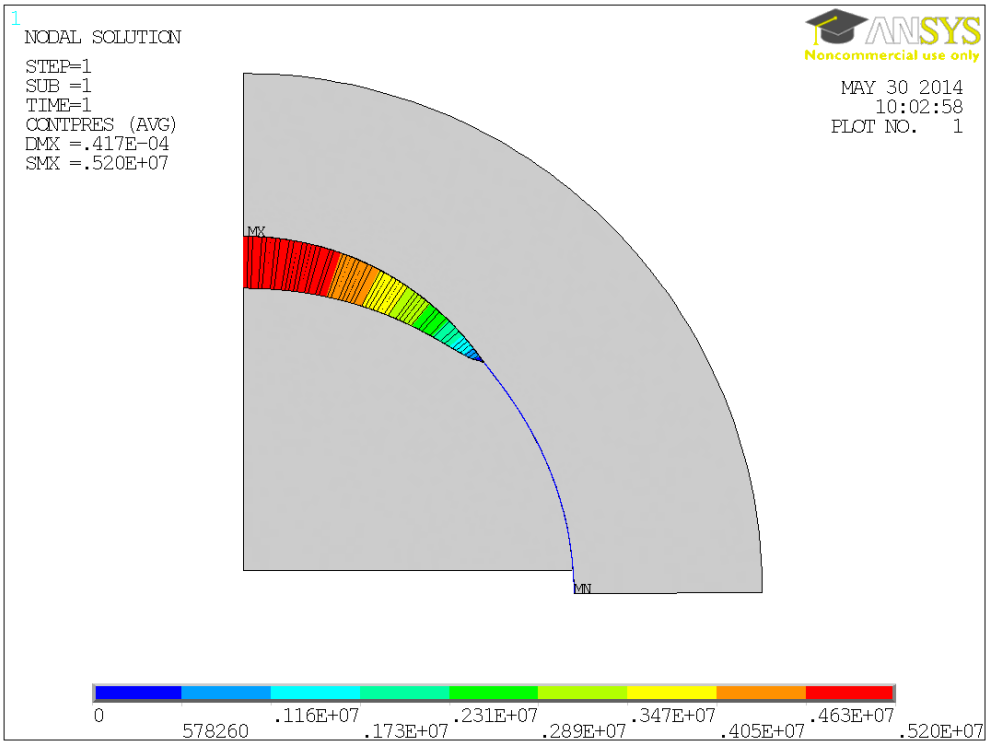

Figure A.10: Contact pressure distribution, 2D model

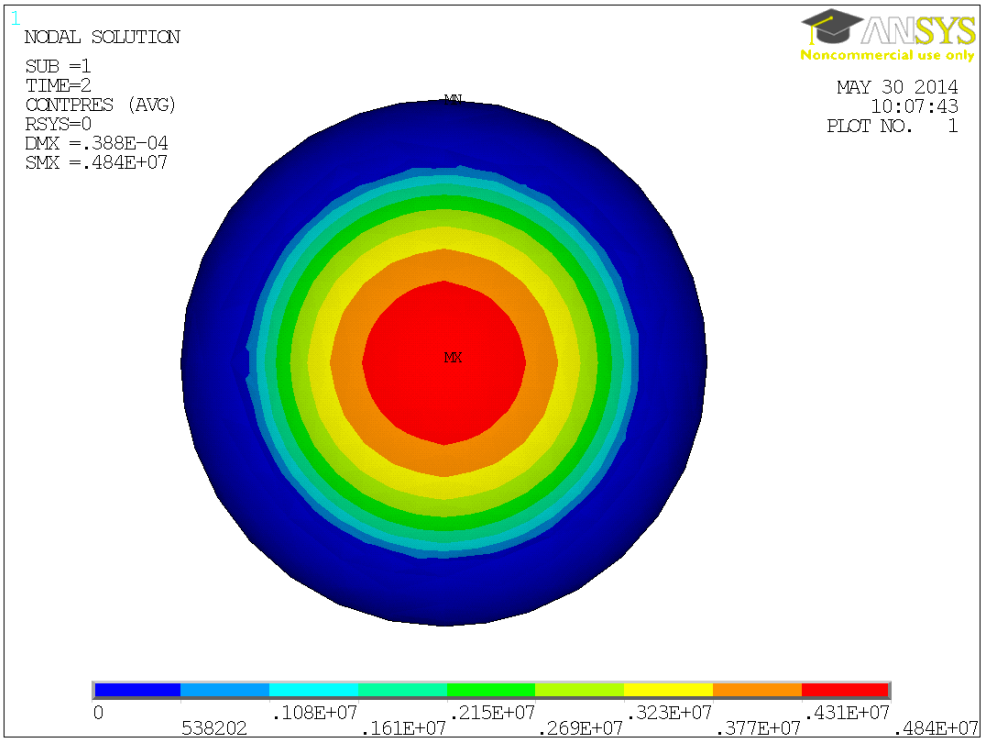

Figure A.11: Contact pressure distribution, 3D model

A similar approach is taken to compare the 2D asymmetric model to the sphere-on-cup model in Section A.1.2. A new 2D model is created using the parameters in Table A.3 and an identical procedure to the model in this section. Table A.7 displays the comparison of the 2D model with the full sphere-on-cup model (MOM). The results indicate that the 2D model likely overestimates peak contact pressure, maximum penetration and contact radius when compared with the 3D model and Hertzian theory. As such, the use of the 2D asymmetric model also overestimates the results in Table A.6.

Case	**Method**	**Peak Contact Pressure**	**Maximum Penetration**	**Contact Radius**
Units	-	MPa	μm	mm
Hertzian	Theoretical	39.9	1.87	3.45
Standard	DLC	39.0	0.65	3.64
2D Asymmetric	LC	43.1	3.45	5.10

Table A.7: Comparison of 2D asymmetric approach to sphere-on-cup model

Lastly, a 3D model is simulated that puts the acetabular cup at an inclination angle α of 45° to reflect the actual orientation of the hip implant *in vivo* and to mirror the orientation used elsewhere in this work. This simulation is run to provide an additional comparison between the 2D asymmetric modeling technique and related assumptions (primarily that the cup is modeled with an inclination angle of 0°) and a more anatomically realistic implant orientation using the same geometric parameters. The 3D model is shown in Figure A.12, where the loading P_0 is applied as a point load at the center of the ball in the $+Y_{A3}$' direction.

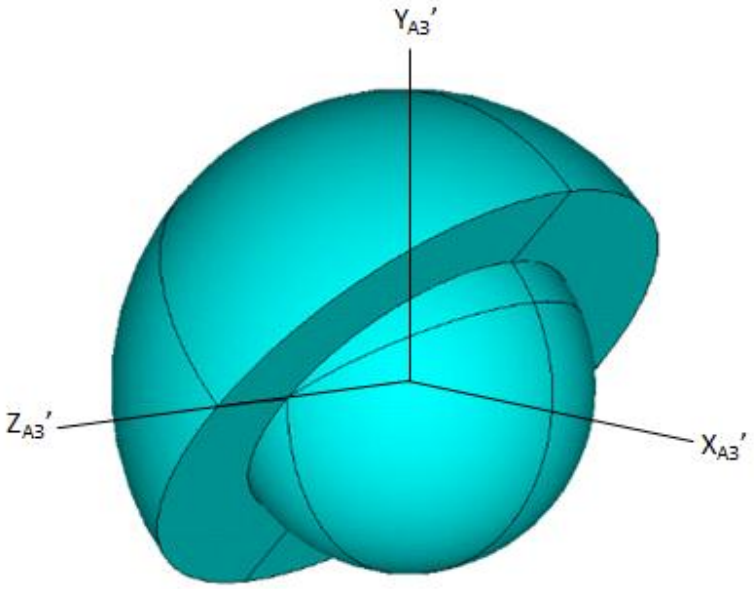

Figure A.12: 3D model (Mattei configuration) at inclination angle of 45°

The results in Table A.8 indicate that the addition of an inclination angle to the model also reduces the contact pressure on the cup surface. This further confirms that the 2D approach used by Mattei *et al.* [32] likely overestimates the contact pressures in the implant and therefore may overestimate linear wear rates to a certain degree.

Parameter	**Units**	**P_0 = 1000N**		
		Mattei [32]	**3D (α = 0°)**	**3D (α = 45°)**
Peak Contact Pressure	MPa	6.5	4.84	4.20
Parameter	**Units**	**P_0 = 2000N**		
		Mattei [32]	**3D (α = 0°)**	**3D (α = 45°)**
Peak Contact Pressure	MPa	10.2	7.76	6.30
Parameter	**Units**	**P_0 = 3000N**		
		Mattei [32]	**3D (α = 0°)**	**3D (α = 45°)**
Peak Contact Pressure	MPa	13.0	10.4	8.01

Table A.8: Effect of inclination angle on the model

This section focuses primarily on the validation of the 3D modeling technique used elsewhere in this work and attempts to compare this approach with published results. As such, the 2D and 3D models show reasonable consistency with one another, though both indicate

slightly lower peak contact pressures than the results shown in the paper. It is further shown that the 2D asymmetric approach may overestimate contact pressures, lending credence to the lower results found by applying the 3D modeling method.

A.1.4 Mesh development and refinement

The method of creating elements and their associated nodes is an integral component of FE analyses. Since there are a number of distinct designs and subtle geometric differences among the models of each design-type, a consistent method is used to mesh the volumes for each design-type. As such, consistent 3D element types and refinement principles are applied to each model.

10-node SOLID186 tetrahedral elements are used for each 3D model, allowing 3 degrees of freedom per node. Tetrahedral elements are used as opposed to 20-node 'brick' elements due to the spherical topology inherent in the models; specifically, meshing with brick-shaped elements is not applicable to spherical volumes due to the need for tetrahedral or pyramid elements along the polar axis of the volume and related element size errors along the external surfaces. As such, tetrahedral elements are applied to mesh the models. Figure A.13 shows a representative 10-node tetrahedral element used by ANSYS. Note that this element type employs mid-side nodes (A/B, Q, R, T, Y and Z).

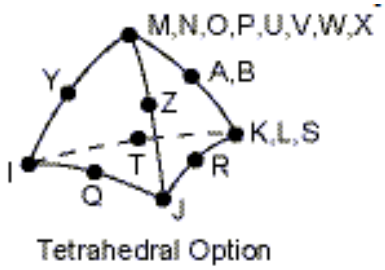

Figure A.13: 10-node SOLID186 tetrahedral element

'Free meshing' is used as opposed to 'mapped meshing' on all models, as the topology of the volumes prevent the mapped meshing approach from being used. As such, element size options are not available to apply to the volumes. This means that a constant element edge length cannot be prescribed to the tetrahedral elements. Furthermore, it is impossible to mesh spherical

volumes using elements of constant size (or volume, in this case). Free meshing, however, allows ANSYS the freedom to choose element edge sizes to accommodate the volume being meshed, resulting in a fairly uniform mesh that can be further refined.

Contact analysis in ANSYS requires the use of Contact and Target elements that are prescribed to the surface of the 3D meshed model. These elements take on the same geometric characteristics as the element that they are connected to (SOLID186, in this case), including the mid-side nodes. CONTA174 and TARGE170 are used in this work due to their compatibility with SOLID186 elements. Surface-to-surface contact is assumed between the contact surfaces, as the contact is often conformal in nature (*ie.* not point-contact or line-contact).

The nature of the application of CONTA174 and TARGE170 elements means that the method of prescribing Contact and Target designations to the meshed surfaces becomes an important matter to ensure consistency between models. ANSYS recommends that materials with relatively high elastic moduli be chosen as the Target and materials with relatively low elastic moduli be chosen as the Contact. As this is the case in the majority of the models simulated in this work, the external areas of the ball are consistently chosen as the Target surfaces. The Contact surface is consistently chosen as the surface of which the wear characteristics are desired; that is, the internal areas of the acetabular cup and the external (flat) areas of the elastic columns are chosen as the Contact surfaces for each model type. This allows the external wear programs to consistently pull contact results from the prescribed Contact surface, which is given a distinct element designation number in the ANSYS Preprocessor.

It is now appropriate to discuss the effect of mid-side nodes on the contact simulation. The mid-side nodes inherent to the SOLID186 element type are not subjected to the same contact analysis as the primary (corner) nodes. As such, the ANSYS results file does not include contact information for any mid-side nodes in the model. These nodes are used when plotting contact results, where the surrounding primary nodes are interpolated at the mid-side nodes to provide some average value. This phenomenon provides smooth contours on contact plots but can cause issues when exporting the results to the wear programs. Section 2.4 discusses in further detail the adjustments made to the wear programs to reflect the behavior of mid-side nodes.

The remainder of this section details the specific mesh characteristics for each design. The effect of mesh refinement on each model is discussed to ensure accuracy of contact results.

A.1.4.1 Conventional design models

The conventional models used in this work are described in full in Section 2.3. Free meshing is applied using a 'Smart Size' of 1. The Smart Size parameter can be set as any integer between 1 and 10, with 1 being the finest mesh obtainable before refinement. As such, these volumes are modeled at the finest setting before refinement.

The model used for this mesh refinement study is identical to that used by Maxian *et al*. [30]. The model parameters used in this study are listed in Table A.9, where the only parameter that may differ from the paper is the radial clearance C (as this value is not explicitly given in the paper). Maxian *et al.* use a 14mm radius cup for mesh refinement and settles on a mesh containing 181 'rigid surface' contact elements (IRS3 and IRS4 element types) using ABAQUS version 5.3 [30]. A constant vertical load P (in the $+Z_C$-direction) of 1000N is applied to the ball. The mesh refinement study is completed by checking not only the peak contact pressure at a constant loading but also the pressure distribution along a path through the center of the contact area located on the internal surface of the cup. Models with 65, 97, 181 and 401 contact elements are simulated before convergence is found between the last two values [30].

Parameter	$\mathbf{R_{cup}}$	$\mathbf{t_{UHMWPE}}$	$\mathbf{t_{backing}}$	**C**	$\mathbf{E_{ball}}$	$\mathbf{\nu_{ball}}$	$\mathbf{E_{plug}}$	$\mathbf{\nu_{plug}}$	**P**
Units	mm	mm	mm	μm	GPa	-	GPa	-	N
Value	14	8	3	40	210	0.31	1.4	0.46	1000

Table A.9: Geometric parameters for mesh refinement study

A very similar method is used in this work to ensure the level of refinement yields converged solutions when compared to denser meshes. Four meshes are simulated in this study and are designated M1 through M4, with M1 being the coarsest mesh analyzed. The method of mesh refinement is simple: first, the 'Refine at Elements' option in the MeshTool window is chosen; second, the elements most likely to be in contact with each other (generally, the center of the contact region is located between the $+Z_C$ and $+Z_C$' axes in the Y_C-Z_C plane) are selected; third, a 'Level of Refinement' of 1 is chosen (the minimal level) and the mesh is subsequently refined. To keep consistency, the same region is meshed each time using the previous mesh density (*ie.* M3 is refined from the M2 model and so on) and using the same Level of Refinement. Meshes M1 through M4 are shown in Figures A.14 through A.17.

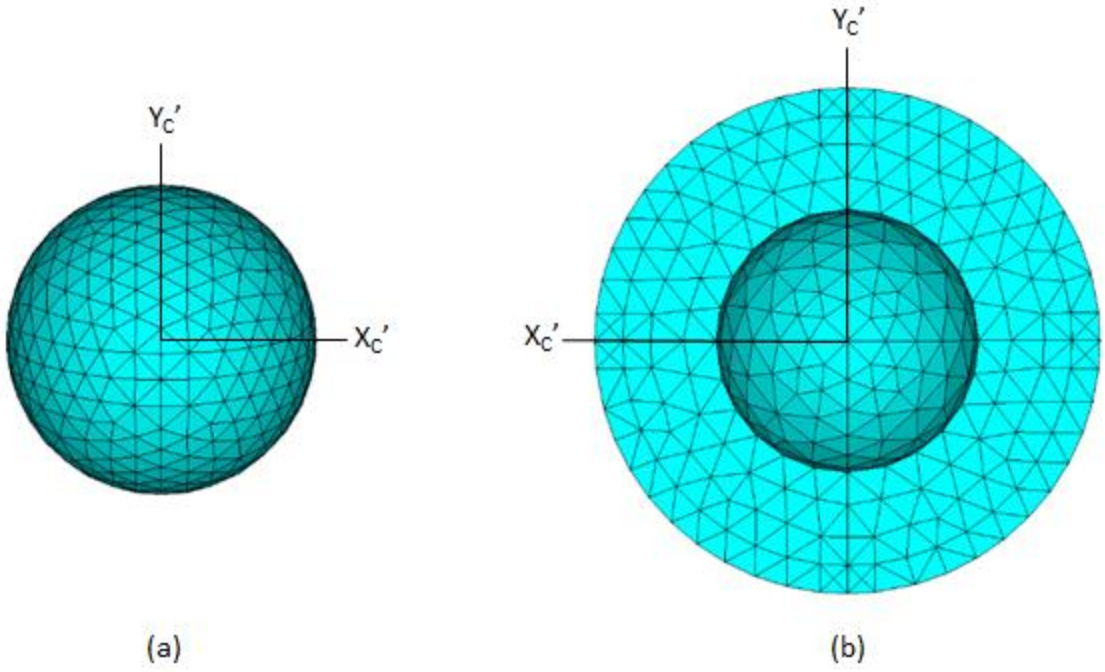

Figure A.14: M1 mesh, conventional model

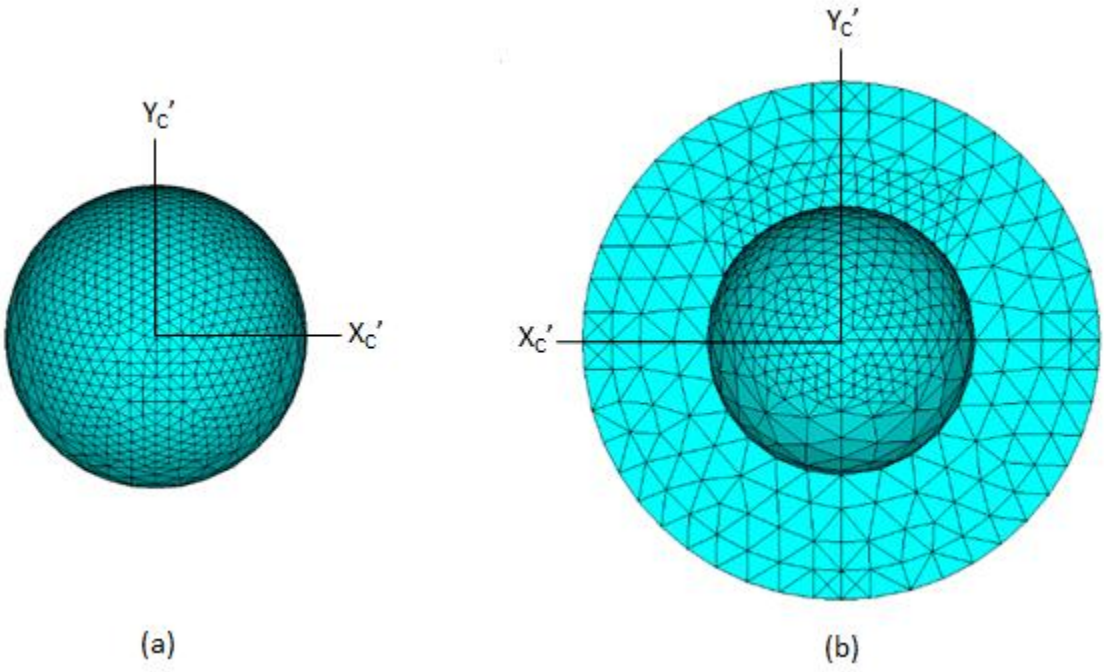

Figure A.15: M2 mesh, conventional model

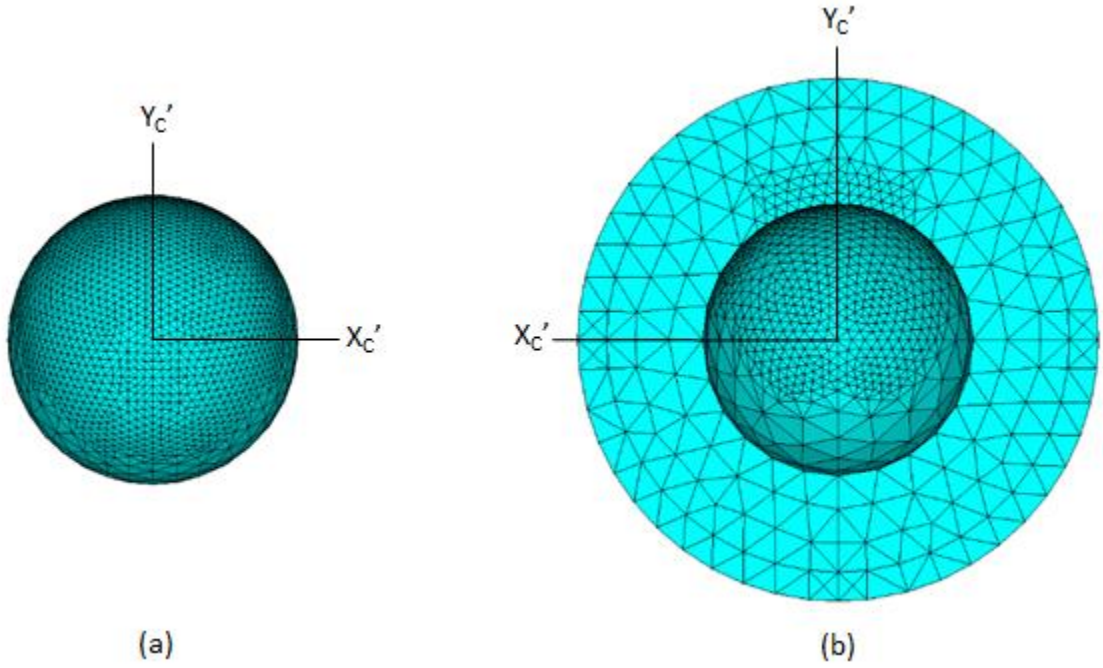

Figure A.16: M3 mesh, conventional model

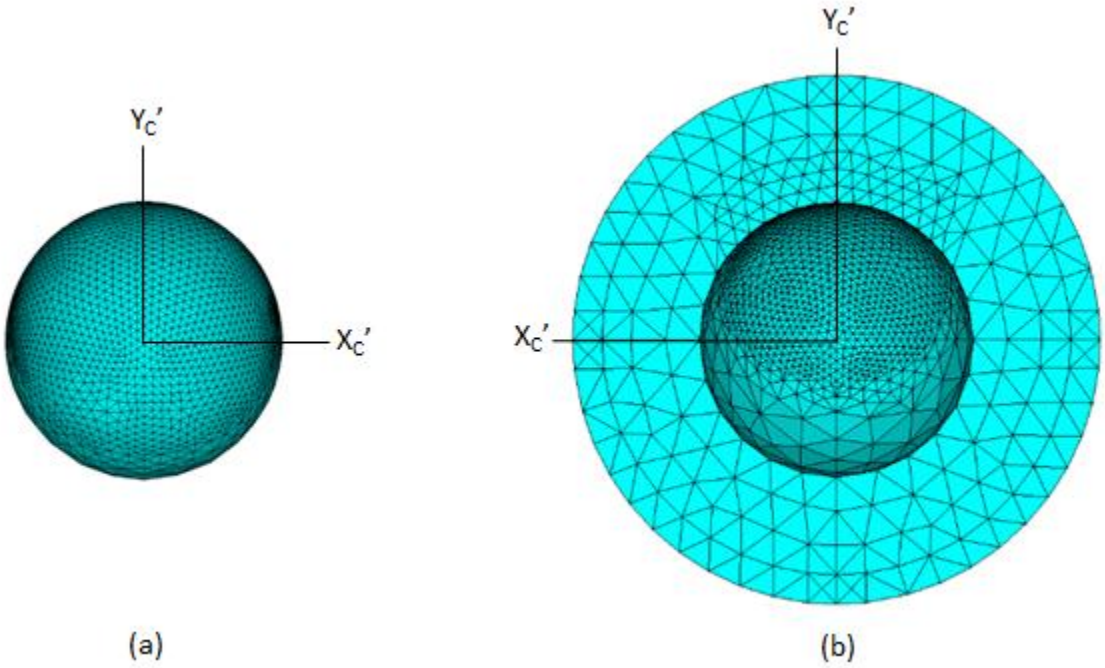

Figure A.17: M4 mesh, conventional model

Figures A.19 through A.22 show two diagrams in each instance: first, the distribution of contact pressure along a path on the internal surface of the cup is plotted; and second, the contact pressure distribution is plotted as seen perpendicular to the X_C'-Y_C' plane. The path along which the contact pressures are plotted passes directly through the region of maximum contact pressure. The path is a full circle starting on the Y_C axis that moves along the internal surface of the cup and stays in the Y_C-Z_C plane (see Figure A.18). As such, the distance along the path (in a circumferential sense) is plotted as the independent variable (X axis) and the contact pressure is plotted as the dependent variable (Y axis).

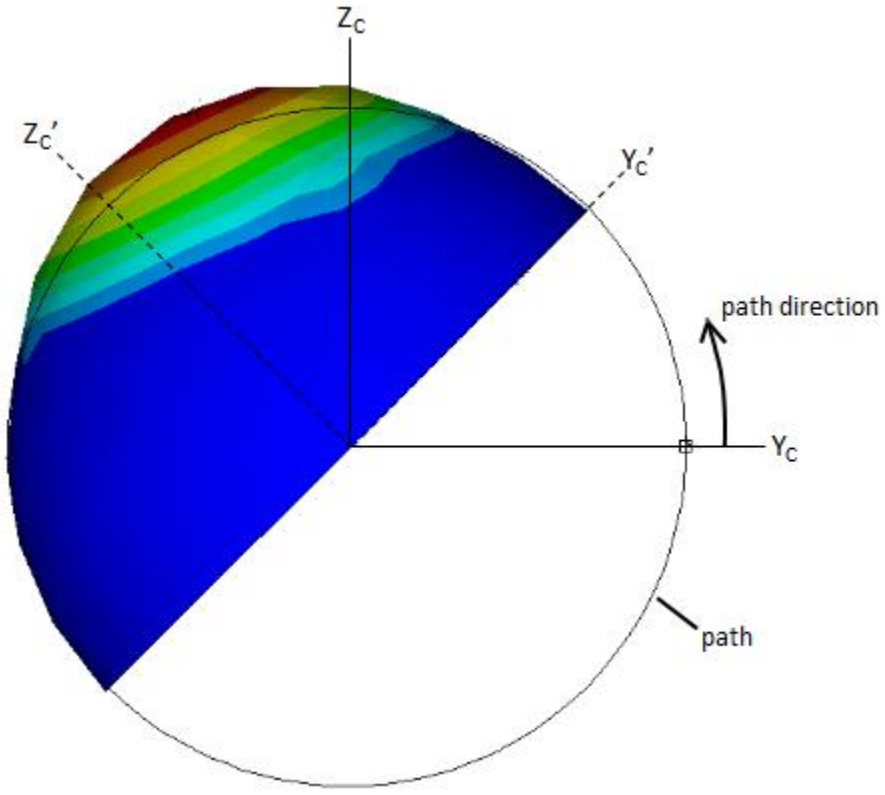

Figure A.18: Definition of path

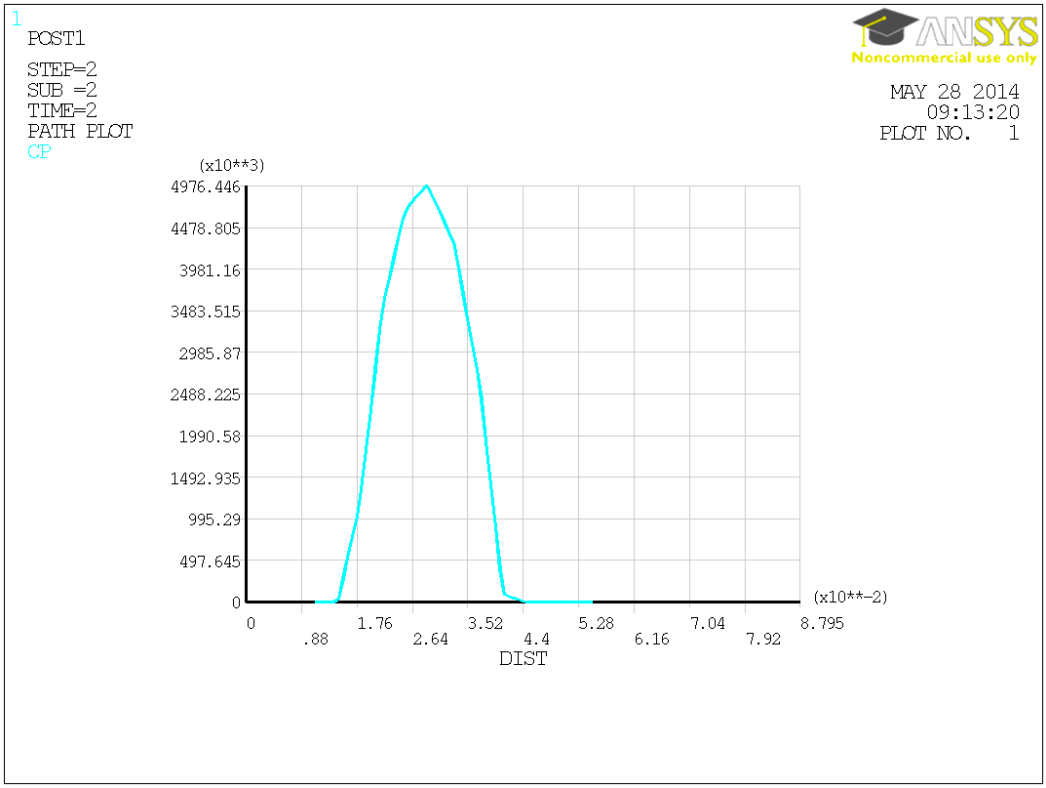

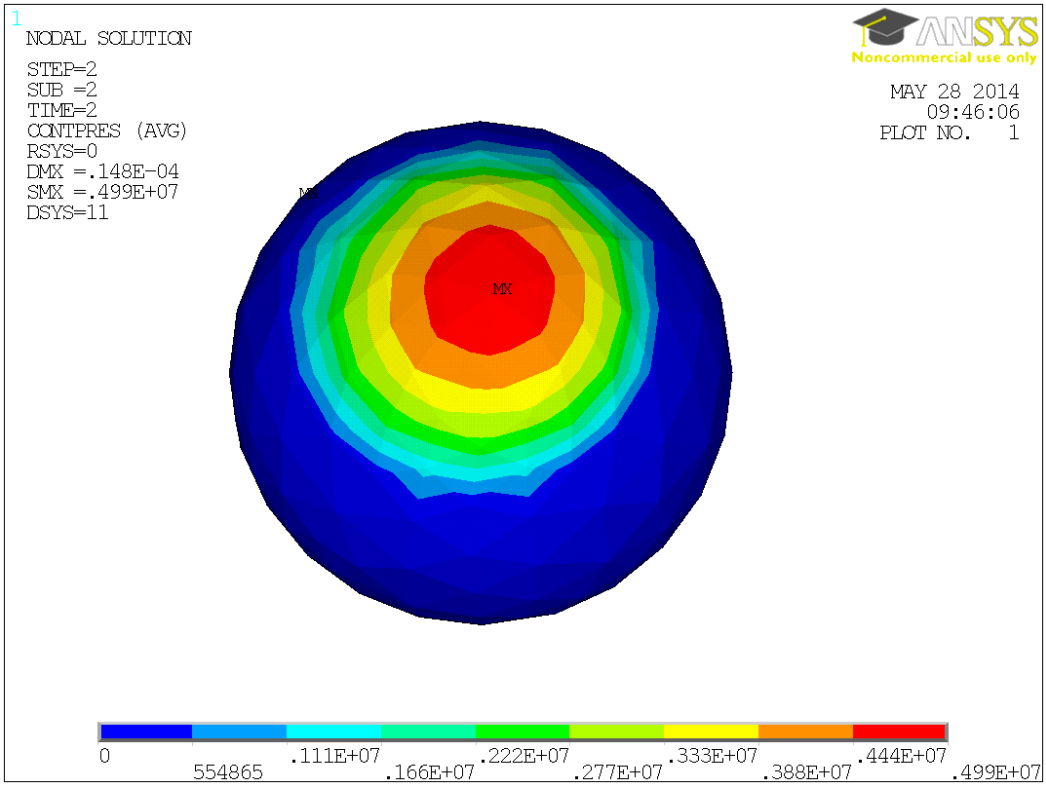

Figure A.19: Contact pressure results, M1 mesh

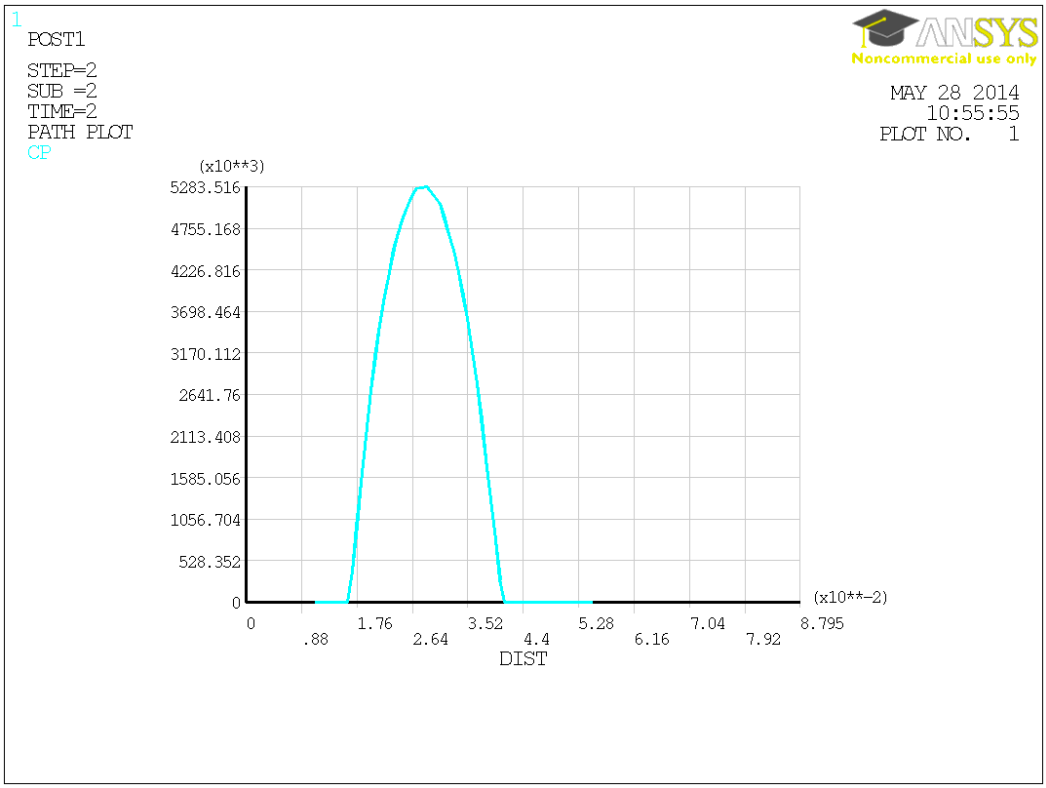

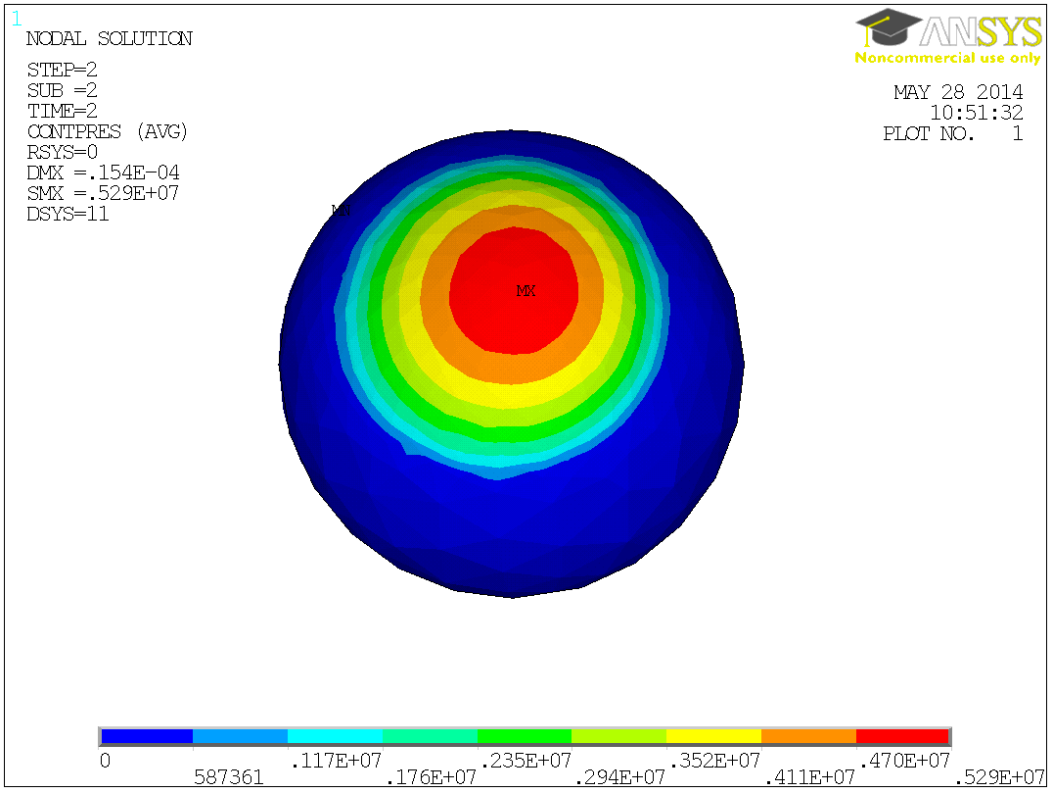

Figure A.20: Contact pressure results, M2 mesh

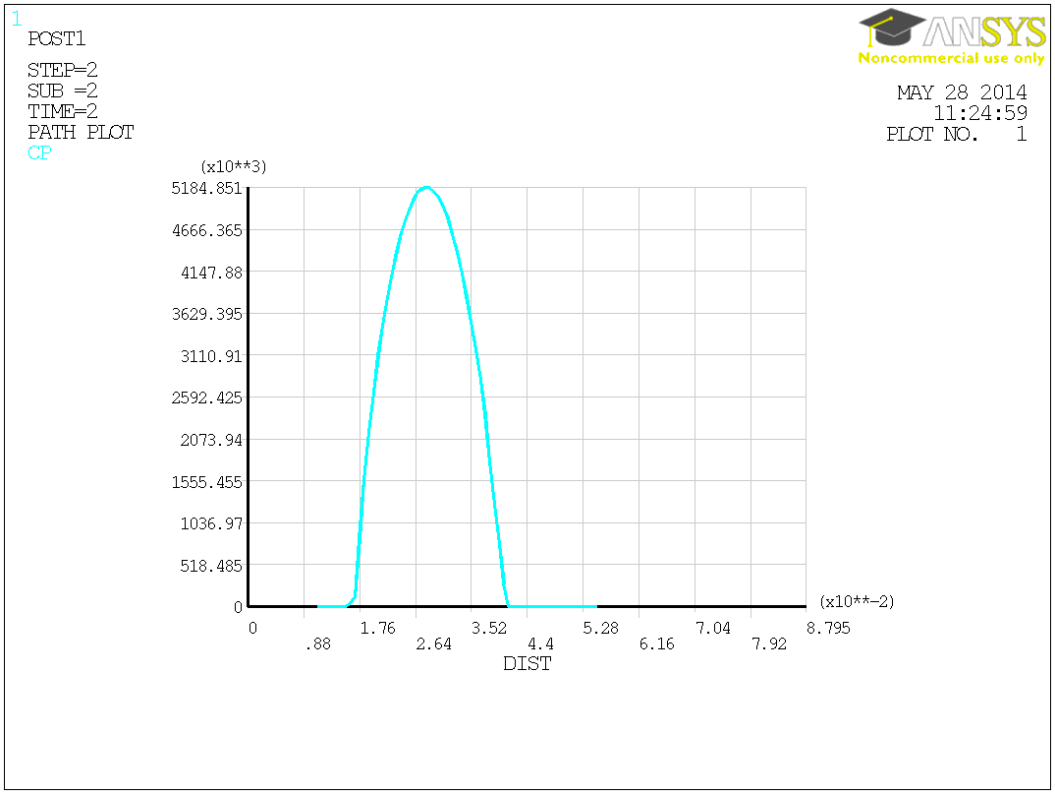

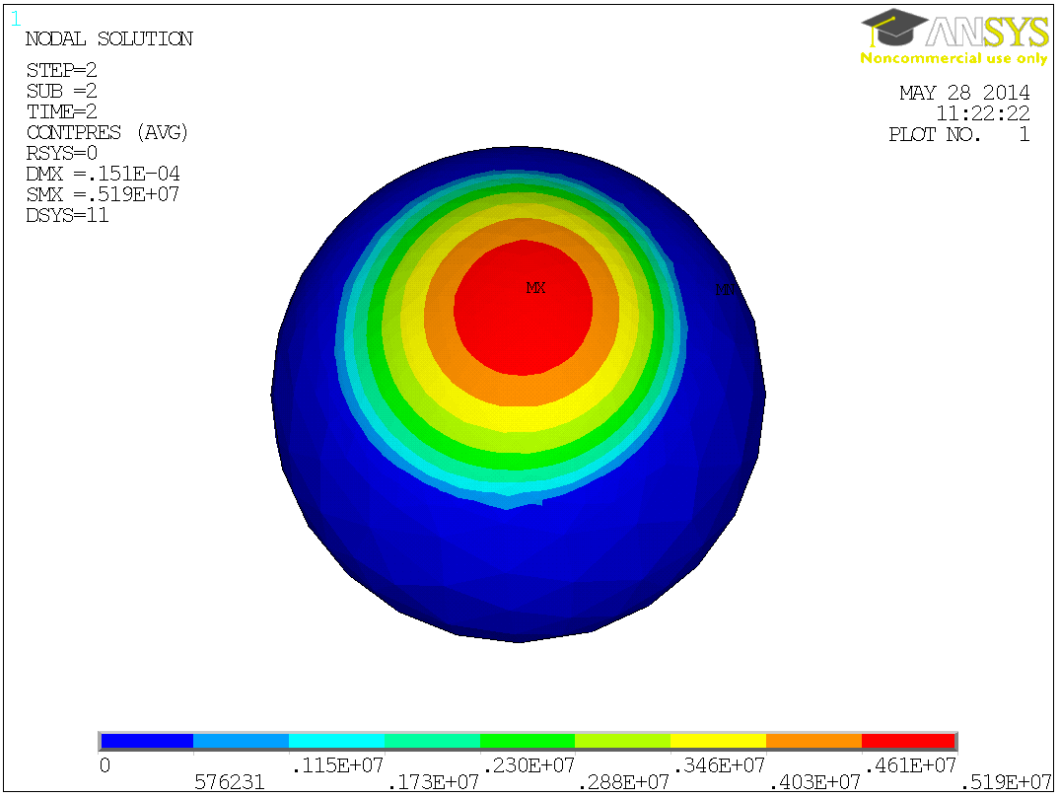

Figure A.21: Contact pressure results, M3 mesh

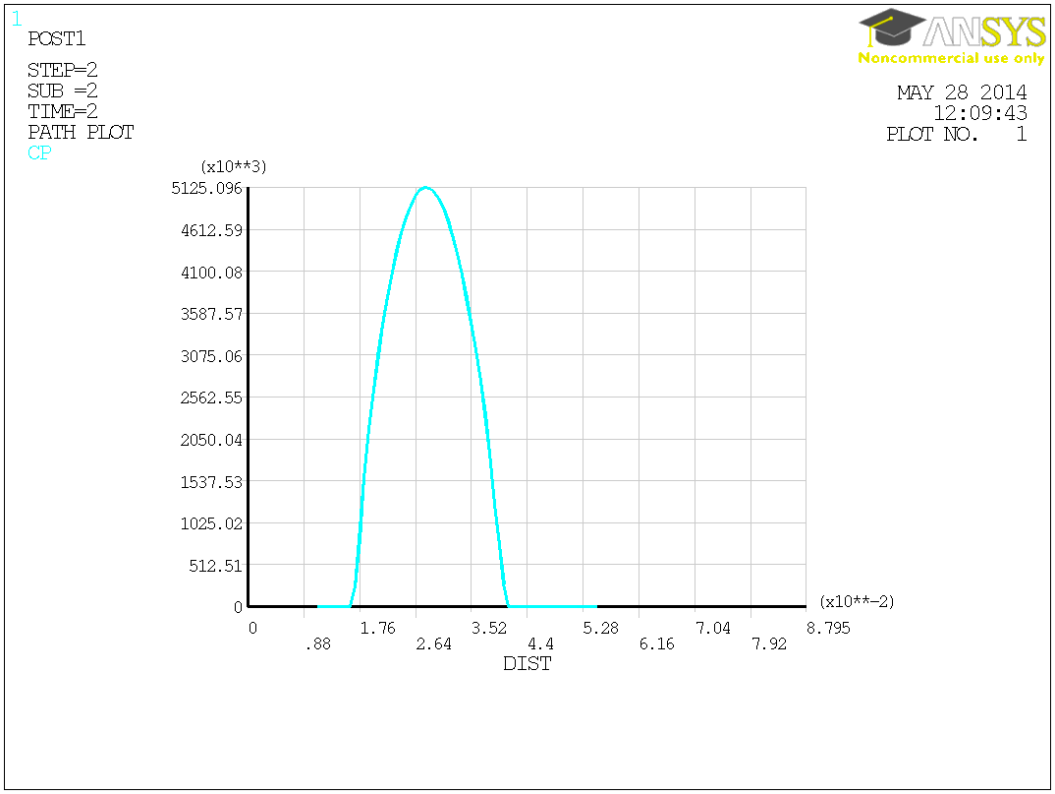

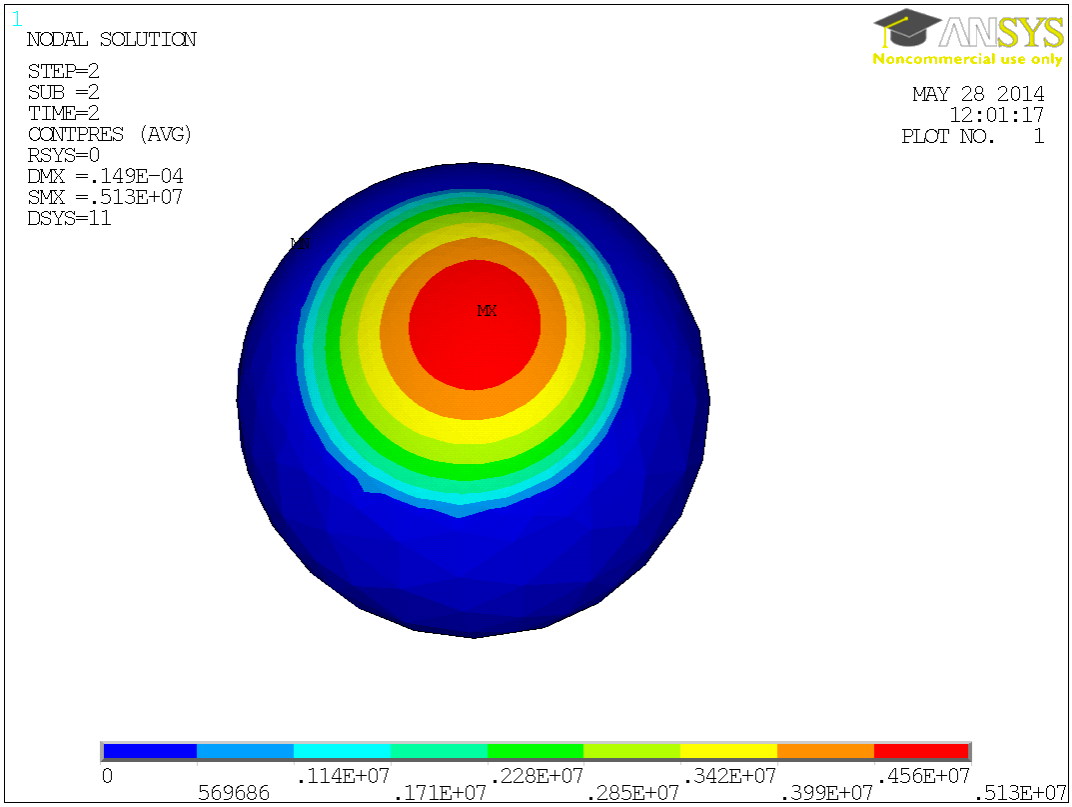

Figure A.22: Contact pressure results, M4 mesh

The mesh parameters and respective results for each mesh density are listed in Table A.10. Note that the lowest level of refinement M1 contains more elements than the mesh chosen for simulation by Mattei *et al.* [30]. Computing times increase significantly with each level of revision, adding an additional parameter to be considered when choosing a mesh for full simulation.

Mesh Density	**No. of Contact Elements**	**Peak Contact Pressure**	**Maximum Penetration**	**Contact Radius**	**Simulation Time**
Units	-	MPa	μm	mm	s
M1	204	4.99	14.8	10.05	150
M2	586	5.29	15.4	10.14	960
M3	1058	5.19	15.1	9.95	7200
M4	1676	5.13	14.9	9.97	17100

Table A.10: Summary of mesh refinement study, conventional model

The results show that each mesh gives nearly identical values for peak contact pressure, maximum penetration and contact radius. The contact region contours, however, are not particularly 'smooth' in M1 when compared with the other mesh densities. As such, it is eliminated as a choice for use in the full runs (particularly since the volumetric wear program relies on accurate contact results at the edges of the contact region). Simulation time is then used to choose mesh density M2 over the more computationally expensive M3 and M4 (7.5 and 17.8 times longer to run than M2, respectively). This is a vital component of this work, as each simulation requires 21 instances in which a load condition must converge (this study only requires 1 load condition to converge). The cumulative time for a simulation, therefore, would be extremely long (potentially multiple days of run-time) for mesh densities M3 and M4. Mesh density M2 fulfills the requirements for accuracy of the desired results, a sufficient number of elements to ensure 'smooth' contours, and reasonable computing time.

There are two additional points that should be discussed relating to the work done by Maxian *et al.* [30]. First, this mesh study is performed on a 14mm radius cup. The conventional model used for the actual simulations in this work assumes a 16mm radius cup. An identical mesh generation process is followed to create the mesh for the 16mm cup (*ie.* a single refinement is performed on the elements that fall within the contact region of the ball-cup interface). The mesh density parameters for the 16mm radius cup are shown in Table A.11.

Mesh Density	No. of Contact Elements	Simulation Time
Units	-	s
M2 – 16mm cup	691	1140

Table A.11: Mesh density parameters, 16mm radius conventional model

The second item to be discussed is the comparison of the results of this mesh study to the results published by Maxian *et al*. [30]. This work generally finds lower (sometimes significantly) contact pressures, and this trend continues in the case of the 14mm radius model. Table A.12 shows the comparison; note that considerably fewer elements are used in the paper and the elements that are used are 'brick-shaped' as opposed to tetrahedral in shape like the ones in this work. The large difference in results can also be attributed to the radial clearance used in each respective model, though it is unknown what clearance is used in their paper to give the published results.

Mesh Density	No. of Contact Elements	Peak Contact Pressure
Units	-	MPa
M2	586	5.29
Maxian *et al.* [30]	181	17.3

Table A.12: Comparison of mesh study to [30]

A.1.4.2 Novel lateral design models

The novel lateral design models simulated in this work are described in full detail in Chapter 2. The mesh strategy for these models differs slightly from that used for the conventional designs, primarily because the Contact and Target surfaces have significantly different areas. Additional mesh refinement is therefore required for the larger Target area of the ball. Furthermore, the contact region is relatively small when compared with the conventional model, making the contact results more affected by mesh density. The geometric parameters used for this study are identical to those presented in Table 2.1 and are shown in Table A.13 for completeness.

Parameter	d_c	e_0	L	φ	E_{ball}	ν_{ball}	E_{plug}	ν_{plug}
Units	mm	mm	mm	°	GPa	-	GPa	-
R = 16mm	3.0	-0.648	5	25.9	210	0.31	1.0	0.46
R = 25mm	3.5	-0.476						

Table A.13: Design parameters for lateral design mesh refinement study

Three mesh densities are simulated for each novel design model; the 16mm radius cup meshes can be viewed in Figures A.23 through A.25 (diagram (a) refers to the column surface and diagram (b) refers to the ball surface for a matching column-ball contact region, respectively). Mesh density M5, the coarsest mesh simulated, is first meshed with a SmartSize of 1 using free meshing. The mesh in the contact region of the ball must be further refined, however, to obtain similarly sized elements to those on the contact surface of the elastic columns. As such, the elements in the contact region are refined twice using a Level of Refinement of 2 each time. At this point, the elements are similar in size and convergence is found when the model is simulated. Mesh densities M6 and M7 are generated by further refinement (Level of Refinement of 1) of each subsequent mesh in the same region, just as in Section A.1.4.1.

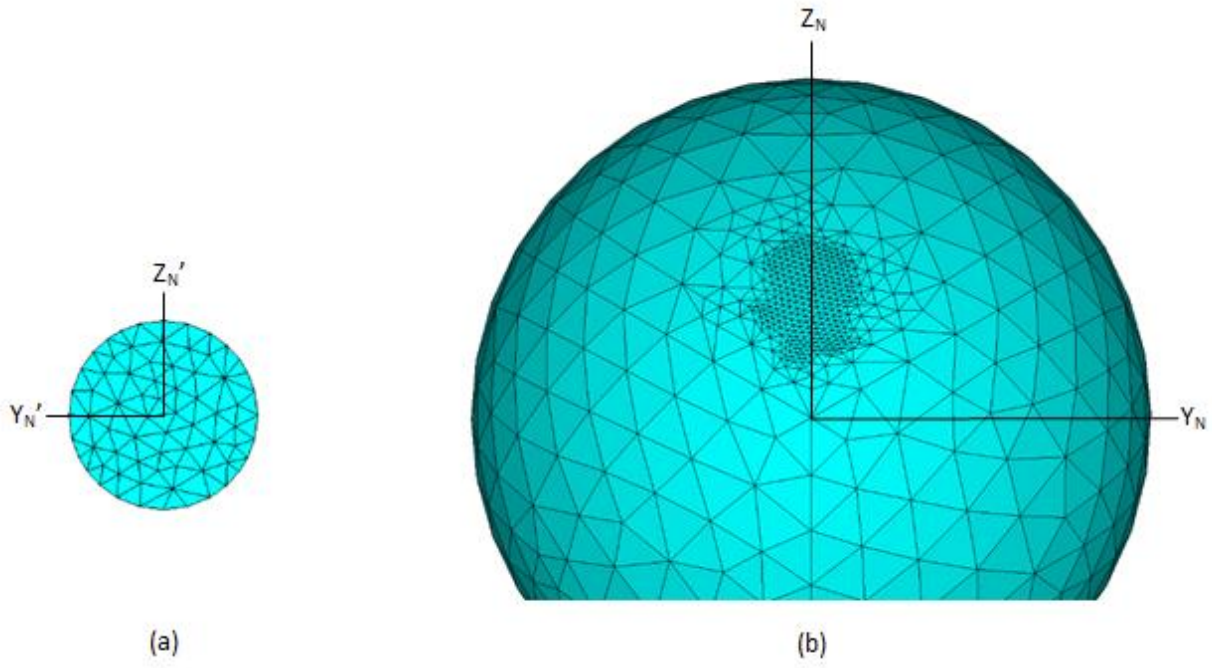

Figure A.23: M5 mesh, lateral design model

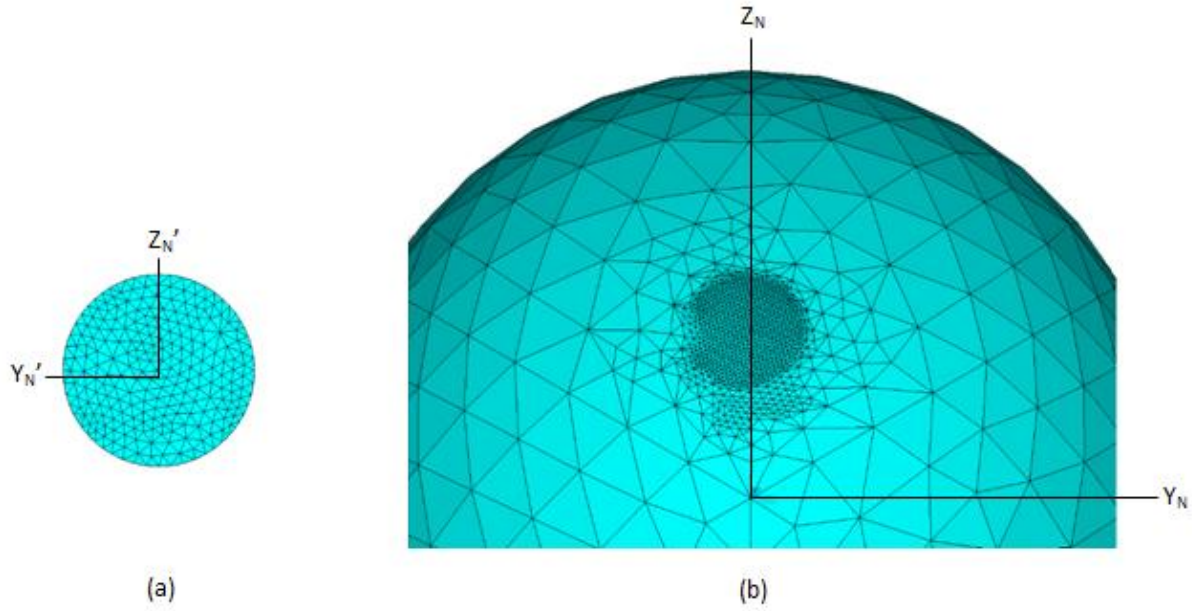

Figure A.24: M6 mesh, lateral design model

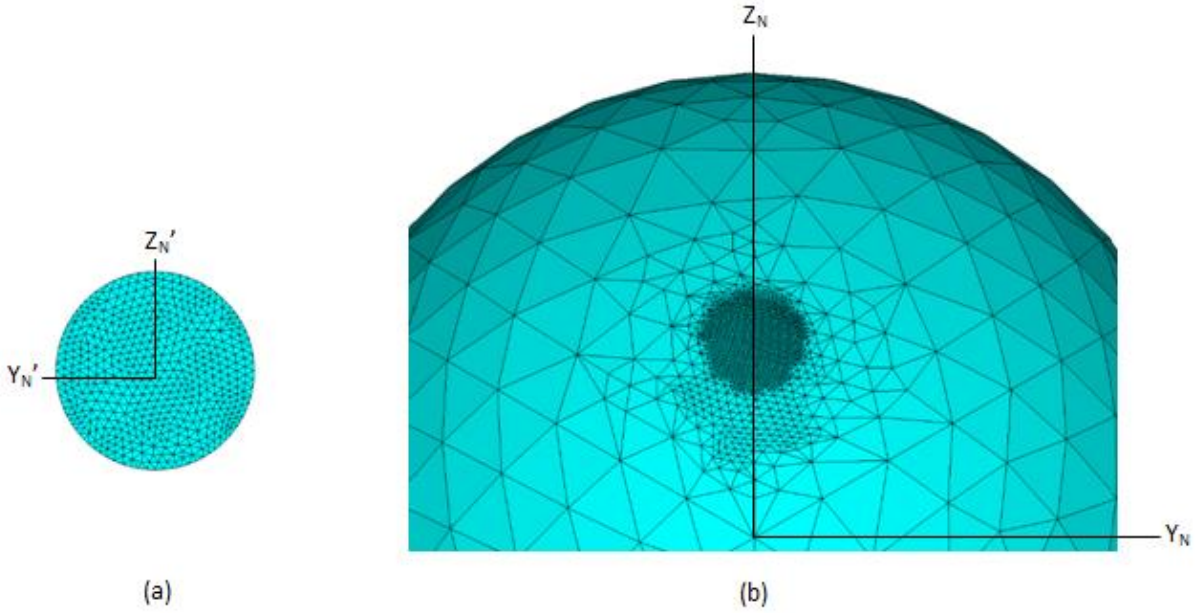

Figure A.25: M7 mesh, lateral design model

Meshes M5, M6 and M7 are simulated using the same Displacement Control method as is used to analyze the novel design models elsewhere in this work; that is, the ball is prescribed to move in the $+Z_N$-direction a distance of e_0 to compress the elastic columns and provide a reaction force. The mesh parameters and simulation results are displayed in Table A.14. Since this method of simulation is identical to that used to provide the results in Chapter 5, linear/volumetric wear results and net reaction force are also relevant to the mesh study and are listed as further validation for convergence of the results. Furthermore, this study is repeated using the 25mm radius model in meshes M8, M9 and M10 for completeness. These meshes are not shown but follow an identical mesh generation process as M5, M6 and M7, respectively. This information is shown in Table A.15. Note that the 'No. of Contact Elements' column includes contact elements on the surface of both elastic columns in the model.

Mesh Density	**No. of Contact Elements**	**Peak Contact Pressure**	**Net Reaction Force**	**Linear Wear Rate**	**Volumetric Wear Rate**	**Simulation Time**
Units	-	MPa	N	mm/year	mm^3/year	s
M5	220	89.7	304.78	2.131	12.76	1020
M6	880	91.2	306.39	2.165	14.26	16200
M7	1908	91.7	306.76	2.171	14.51	44100

Table A.14: Summary of mesh refinement study, 16mm radius lateral design model

Mesh Density	**No. of Contact Elements**	**Peak Contact Pressure**	**Net Reaction Force**	**Linear Wear Rate**	**Volumetric Wear Rate**	**Simulation Time**
Units	-	MPa	N	mm/year	mm^3/year	s
M8	218	65.4	301.66	2.425	19.31	1110
M9	672	69.6	304.52	2.583	22.68	18360
M10	1962	70.1	304.91	2.602	22.89	52740

Table A.15: Summary of mesh refinement study, 25mm radius lateral design model

The results for both the 16mm radius and the 25mm radius models show convergence between the second and third mesh densities simulated (M6-M7 and M9-M10, respectively). Therefore the intermediate mesh in each case – M6 for the 16mm model and M9 for the 25mm model – is chosen for the extended simulations. It should be noted that the meshes chosen for the novel designs employ significantly finer mesh densities than the conventional models. Since the contact region is significantly smaller on the elastic columns and the contact pressures are significantly higher than for the conformal contact inherent to the conventional models, a denser mesh is required for accurate results.

An identical mesh generation process is applied to the lateral designs that employ metal coatings. The orientation and respective parameters associated with the coated models are discussed in full in Chapter 2. It is necessary to perform a separate mesh refinement study on these models because the contact region is smaller on the surface of the coating and therefore subject to a different contact distribution. This study is performed on models using a coating thickness of 200μm. Displacement Control is used in the same manner, and three mesh densities are used for each ball radius (M11, M12 and M13 for the 16mm radius model and M14, M15 and M16 for the 25mm radius model). The coarsest mesh used (M11) corresponds to the coarsest mesh used in Section A.1.4.2 (M6). This mesh density is generated by applying free meshing with a SmartSize of 1. Mesh densities M12 and M13 are generated by further refining M11 by a Level of Refinement of 1 and 2, respectively. Note that the mesh densities for the coated models contain nearly twice the number of elements as the uncoated models; this is because the free meshing option automatically creates a more refined mesh in the immediate area of the coating, as element sizes must correspond to the coating thickness and therefore must be marginally smaller than the elements in this region of the uncoated models. Meshes M11, M12 and M13 are shown in Figures A.26 through A.28.

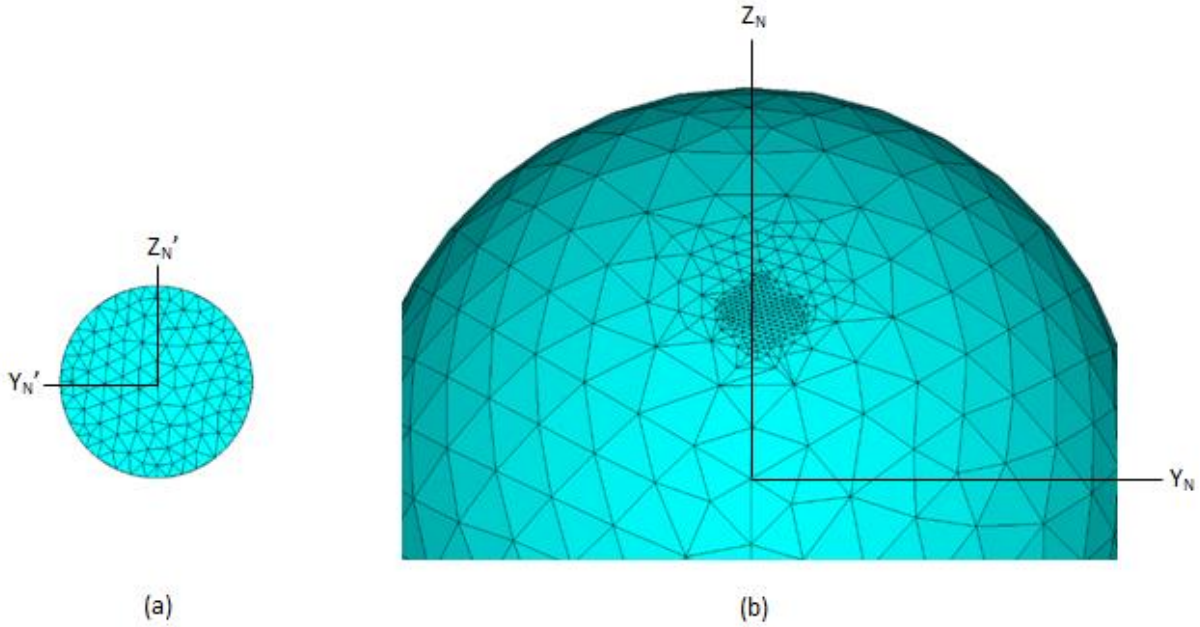

Figure A.26: M11 mesh, coated lateral design model

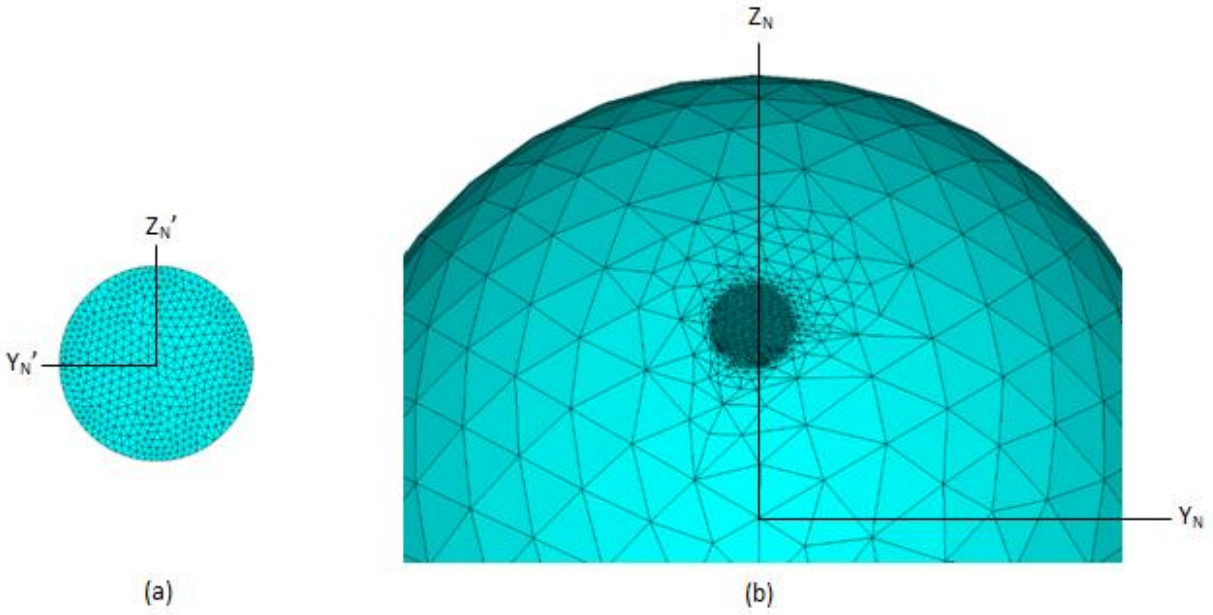

Figure A.27: M12 mesh, coated lateral design model

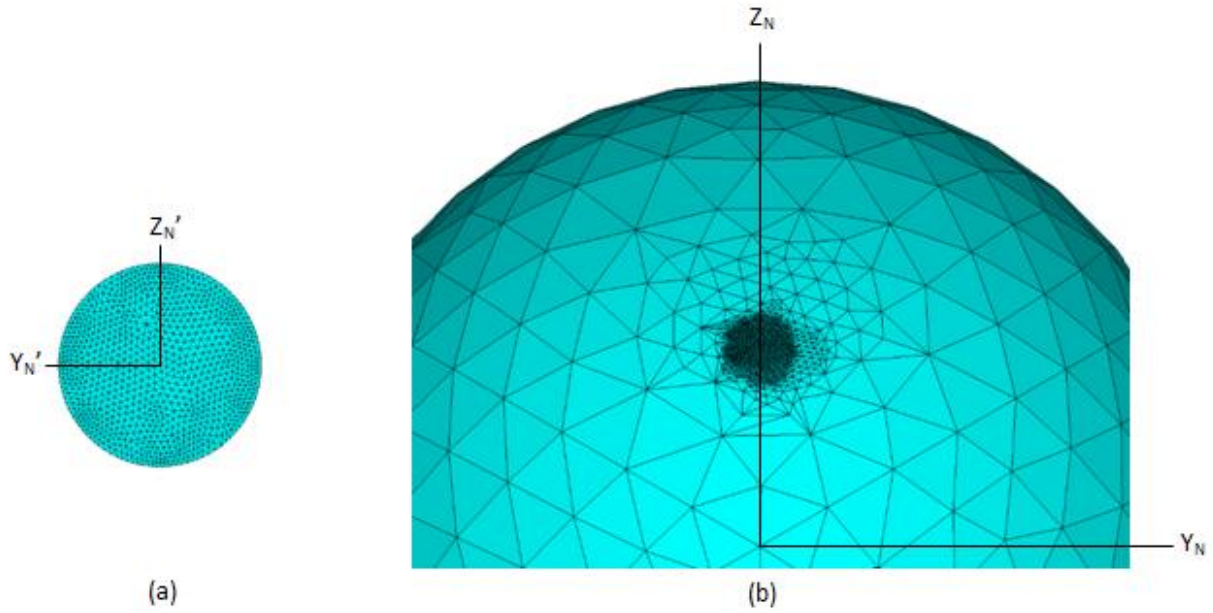

Figure A.28: M13 mesh, coated lateral design model

Mesh parameters and results for the coated models are shown in Tables A.16 and A.17 for the 16mm radius and 25mm radius models, respectively. Again, net reaction forces and wear rate results are also displayed due to the importance of mesh density on these parameters in the novel design models. The 'No. of Contact Elements' column refers to both elastic columns.

Mesh Density	**No. of Contact Elements**	**Peak Contact Pressure**	**Net Reaction Force**	**Linear Wear Rate**	**Volumetric Wear Rate**	**Simulation Time**
Units	-	MPa	N	mm/year	mm^3/year	s
M11	428	160	327.72	0.0178	0.058	3420
M12	1712	159	327.99	0.0178	0.069	22500
M13	3852	159	328.05	0.0178	0.069	59400

Table A.16: Summary of mesh refinement study, 16mm radius coated lateral design model

Mesh Density	No. of Contact Elements	Peak Contact Pressure	Net Reaction Force	Linear Wear Rate	Volumetric Wear Rate	Simulation Time
Units	-	MPa	N	mm/year	mm^3/year	s
M14	420	103	324.92	0.0179	0.083	3960
M15	1680	98.8	324.02	0.0172	0.112	25560
M16	3780	98.5	323.98	0.0172	0.113	63900

Table A.17: Summary of mesh refinement study, 25mm radius coated lateral design model

The simulation results show convergence between mesh densities M12 and M13 for the 16mm radius model and between M15 and M16 for the 25mm radius model. As such, mesh densities M12 and M15 and their associated generation processes were chosen for further simulations. The simulation time for these models is considerably longer than for the uncoated models, but the finer mesh density is required for accurate results.

Two coating thicknesses are used for full simulations: 200µm and 400µm. The mesh generation procedure is identical for this model as for the M12 mesh density. The 400µm-thick coating is only evaluated at the 16mm radius cup size and its associated mesh parameters are shown in Table A.18 for completeness.

Configuration	No. of Contact Elements	Simulation Time
Units	-	s
400µm coating	1512	24200

Table A.18: Mesh density parameters, 400µm-thick coating

A.1.4.3 Novel in-line design models

It is found in the course of simulation that the mesh densities (and respective generation processes) used for the standard and coated lateral design configurations can be applied directly to the in-line configuration to obtain converged solutions. As such, the low-modulus in-line configuration uses a mesh generation procedure as follows: first, both the vertical column and the ball are meshed using a SmartSize of 1; second, the elements in the contact region on the ball

surface are refined twice using a Level of Refinement of 2 in each case to obtain similarly sized elements on both Contact and Target surfaces; and third, both the Contact and Target elements are further refined once using a Level of Refinement of 2. The mesh parameters associated with the 16mm radius and 25mm radius models are shown in Table A.19.

Cup Radius	d_c	e_0	No. of Contact Elements	Simulation Time
Units	mm	mm	-	s
16mm	3.00	-0.248	1344	13500
	3.50	-0.182	1724	14040
	4.00	-0.139	2160	15300
25mm	3.00	-0.248	1344	18540
	3.50	-0.182	1808	19080
	4.00	-0.139	2238	19440

Table A.19: Mesh density parameters, uncoated in-line configuration

Similarly for the in-line orientation employing coatings, the same mesh generation procedure is applied as for the coated lateral design orientation; a Level of Refinement of 1 is applied to a free meshed model of SmartSize 1, corresponding to the intermediate M12 mesh density. For the in-line configuration, only the 4mm diameter column is simulated at the 16mm radius geometry. The mesh densities used for both the 200µm and the 400µm thick coatings in this orientation are displayed in Table A.20.

Coating Thickness	d_c	e_0	No. of Contact Elements	Simulation Time
Units	mm	mm	-	s
200µm	4.00	-0.248	1520	14400
400µm	4.00	-0.248	1376	15840

Table A.20: Mesh density parameters, coated in-line configuration

A.1.5 Conventional model wear rates

Applying the mesh densities chosen in Section A.1.4, the wear results applying the conventional models used in this work can be compared to the results found by Maxian *et al*. [30]. The models to be compared are geometrically identical with the exception of radial clearance in the spherical bearing; the radial clearance C used in this study is 40μm, while the clearance used in that paper is not clearly specified. As such, this potential geometric difference could cause variation between the compared results.

The wear algorithm is discussed elsewhere in this work and follows the same formulation applied by Maxian *et al.* [30]. There are differences in the modeling and contact algorithms applied as Maxian *et al.* use ABAQUS as opposed to ANSYS [30]. Moreover, this work was published in 1996; significant improvements have been made in computing power, nonlinear contact capabilities in FE packages and FE mesh refinement capabilities in the nearly two decades since this paper was published. That being said, it should be expected that contact and wear results are somewhat different in this thesis. This comparison, however, is necessary to ensure that the results found in this work are reasonable when compared to more widely-accepted results.

Applying the same gait cycle loading and kinematic conditions (Brand *et al.* [44]) as in the paper to the conventional 16mm radius model, linear and volumetric wear rates are calculated from the contact pressure distribution. These results are displayed in Table A.21. Clinical wear data provided by Maxian *et al.* [30] is also shown for validation purposes. The linear wear distribution on the cup surface is shown in Figure A.29.

Case	**Linear Wear Rate**	**Volumetric Wear Rate**
Units	mm/year	mm^3/year
16mm model	0.0696	24.77
Maxian results [30]	0.116	18
Clinical data [30]	0.10 ± 0.06	3 to 256

Table A.21: Comparison of conventional models with published results

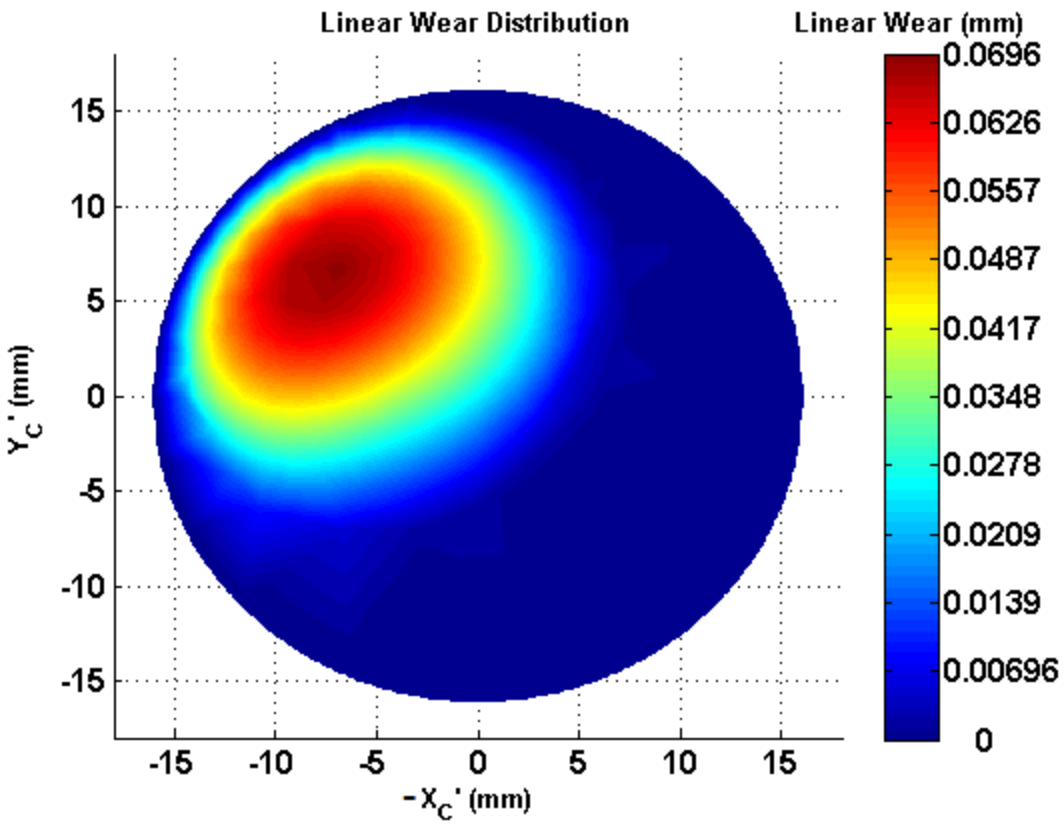

Figure A.29: Linear wear distribution, 16mm conventional model

The wear results found in this work compare reasonably with the paper. It is expected that the linear wear rate is lower for this work as lower contact pressures are consistently found using the models in this paper than other published results. That said, volumetric wear is larger using the conventional model in this work. This can likely be attributed to a considerably finer mesh that more accurately captures the wear depth at a greater number of nodes and therefore more accurately represents the true contact distribution on the cup surface. Furthermore, these wear results fall comfortably within the ranges for linear and volumetric wear rates found clinically, further validating the approach used in this paper. The wear distribution shows a shifted wear region that is representative of the relatively high loads applied to the ball in the X_C and $-Y_C$ directions. The location of the wear region compares similarly to the distribution of contact stresses that is plotted in Figure 5 of Maxian *et al.* [30], which is to be expected.

A.1.6 Effective stiffness, coated elastic columns

This section uses effective spring theory to validate that the uncoated and coated elastic columns require the same displacement to provide a net reaction load of 350N. Figure A.30 shows the specific case described in this section.

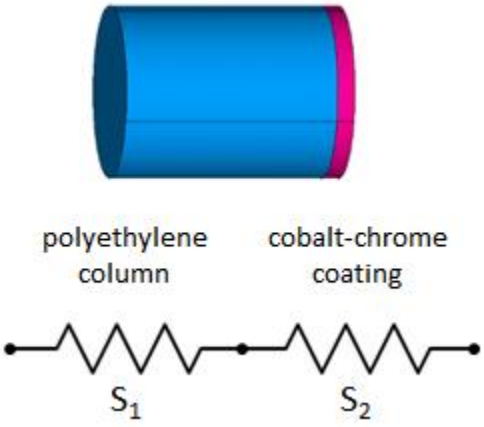

Figure A.30: Spring diagram for coated column

The polyethylene column and the cylindrical cobalt-chrome coating are effectively two springs acting in series. Assuming pure compression, the stiffness S_i of each spring is given by:

$$S_i = \frac{\pi E_i {d_i}^2}{L_i} \tag{A.7}$$

where E_i is the elastic modulus; d_i is the cross-sectional diameter; L_i is the length of the elastic column; and i is an integer that refers to the specific spring. It can further be assumed that both springs have a common diameter d. For two springs in series, the effective spring stiffness is given by:

$$\frac{1}{S^*} = \frac{1}{S_1} + \frac{1}{S_2} \tag{A.8}$$

$$or \ldots \quad S^* = \left[\frac{1}{S_1} + \frac{1}{S_2}\right]^{-1} = \frac{S_1 S_2}{S_1 + S_2} \tag{A.9}$$

Substituting Eqn. A.7 into Eqn. A.9 and simplifying gives:

$$S^* = \frac{\pi d^2}{4}\left[\frac{E_1 E_2}{E_1 L_2 + E_2 L_1}\right] \tag{A.10}$$

Assuming a desired reaction load $\boldsymbol{F}_{elast}$ equal to 350N, the required initial offset e_0 is given by:

$$e_0 = -\frac{350}{S^*} \tag{A.11}$$

Table A.22 provides a summary of the novel lateral design models simulated. To take into account that there are two effective springs and the angle at which the springs act on the ball, the following trigonometric factor is multiplied with S^* [24]:

$$S' = 2(\sin^2 \varphi)S^* \tag{A.12}$$

Note that the designation i = 1 refers to the polyethylene material ($E_1 = 1.0$ GPa and $L_1 = 5$mm) and i = 2 refers to the coating ($E_2 = 210$ GPa and L_2 is equal to the respective coating thickness).

d	**L_2**	**S'**	**e_0**
mm	µm	N/m	mm
3.0	No Coating	5.4001E+05	-0.648
	200	5.3990E+05	-0.648
	400	5.3980E+05	-0.648
3.5	No Coating	7.3501E+05	-0.476
	200	7.3487E+05	-0.476
	400	7.3473E+05	-0.476

Table A.22: Summary of effective spring calculations, lateral design orientation

d	L_2	S^*	e_0
mm	μm	N/m	mm
3.0	No Coating	1.4137E+06	-0.248
	200	1.4134E+06	-0.248
	400	1.4132E+06	-0.248
3.5	No Coating	1.4137E+06	-0.182
	200	1.9239E+06	-0.182
	400	1.9235E+06	-0.182
4.0	No Coating	1.4137E+06	-0.139
	200	2.5128E+06	-0.139
	400	2.5123E+06	-0.139

Table A.23: Summary of effective spring calculations, in-line configuration

The results for both the lateral design and the in-line design orientations show that the addition of a cobalt-chrome coating does not affect the required initial offset e_0. Since the length of the polyethylene column is much larger and the elastic modulus is much lower than the metal coating, the effective stiffness of the elastic element remains unchanged.

Appendix B

B.1 Lubrication analysis

This section provides a summary of the validation steps associated with the lubrication simulation in this thesis (Chapters 2 and 3). Topics discussed include the validation of the explicit integrator for the stance phase analysis, the time steps applied to the finite element lubrication model for the stance phase, and the finite element mesh creation methodology for the in-line design configuration.

B.1.1 Validation of explicit integrator

Boedo and Booker [24] apply an implicit variable-step numerical integration routine to the finite element lubrication model for the simulation presented in their paper. This implicit routine is used to ensure accuracy of the results, though it is somewhat less computationally efficient than an explicit routine. As such, the explicit integrator applied to the in-line models must be validated against the implicit routine.

A generic stance phase case applying a nominal radial clearance C_0 of 30μm, ellipticity δ of 40μm, viscosity μ of 2.5 mPa-s, and cavitation threshold pressure p_{cav} of 0 kPa (characteristic of parameters used for the simulations performed in Chapter 3) is simulated using both the explicit and implicit integration routines. The lateral design fluid-film mesh employed by Boedo and Booker [24] is simulated in this study. Figure B.1 displays the time history of minimum film thickness and maximum film pressure for both integration routines at the 16mm cup geometry.

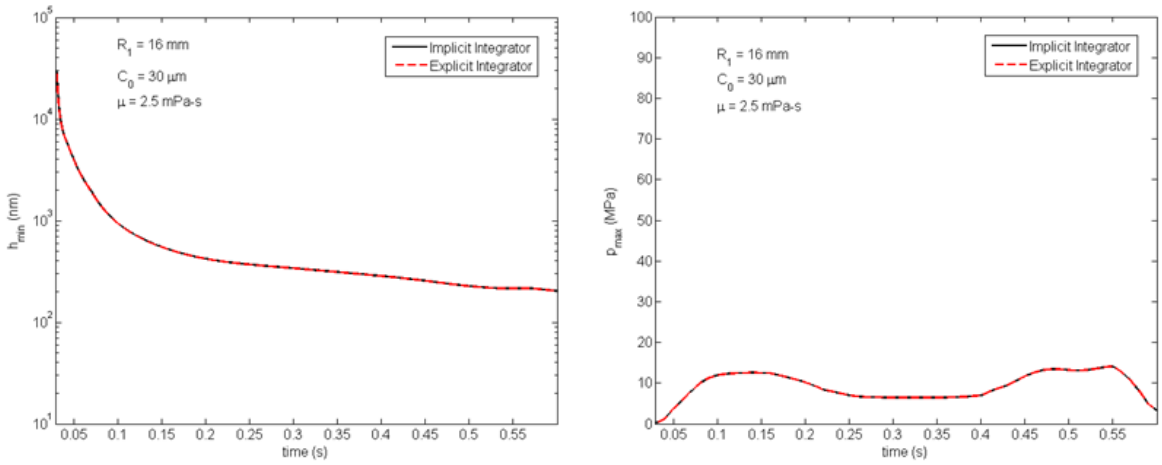

Figure B.1: Validation of explicit integration routine

The results for this case are identical, showing that the explicit integrator provides the same results as the implicit integrator applied by Boedo and Booker [24]. For this particular case, the explicit routine is 4.5 times shorter to simulate than the implicit integrator. As such, the explicit integration routine is used for the lubrication studies provided in this thesis.

B.1.2 Validation of time step

The time step applied to the stance phase finite element lubrication algorithm is important to ensure accuracy of results and to provide reasonable computing efficiency. Boedo and Booker [24] use a time step of 0.0002s in their investigation of the stance phase. The purpose of this study is to validate the time step used in the paper and to evaluate the feasibility of applying larger time steps to the lubrication analysis in this thesis.

Three time step values are simulated: 0.00005s, 0.0002s, and 0.0005s. The design case is identical to that used for the implicit-explicit validation in Section B.1.1 (that is, C_0 = 30µm, δ = 40µm, μ = 2.5 mPa-s, and p_{cav} = 0 kPa). Figure B.2 displays the time history of minimum film thickness and maximum film pressure for both integration routines at the 16mm cup geometry.

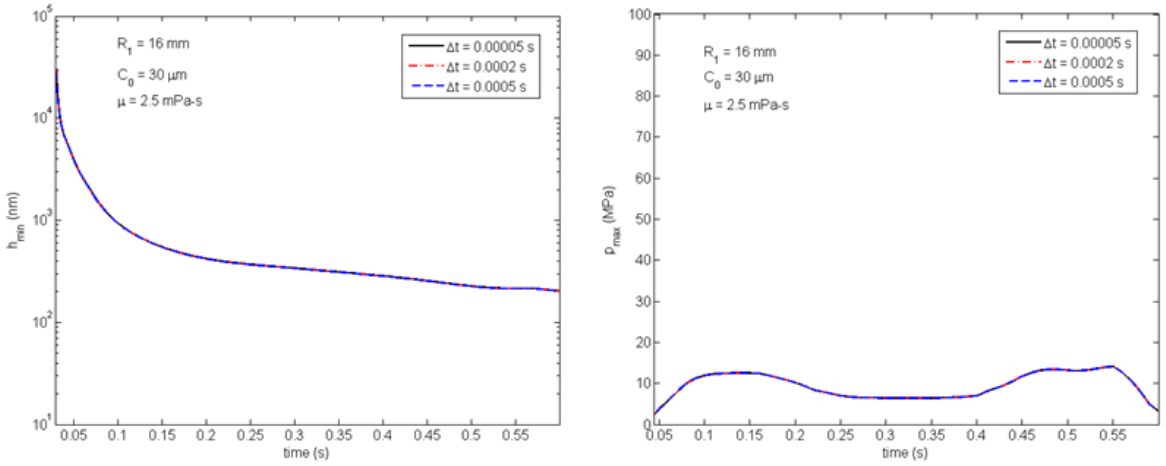

Figure B.2: Validation of time step

The shape and magnitude of the minimum film thickness and maximum film pressure curves are identical for each time step used. Table B.1 displays cyclic minimum film thickness and cyclic maximum film pressure results in addition to computation time for each time step.

Time Step	Cyclic h_{min}	Cyclic p_{max}	Computation Time
s	nm	MPa	s
0.00005	202.82	14.10	1890
0.0002	202.64	14.10	500
0.0005	202.64	14.11	235

Table B.1: Time step validation: cyclic minimum film thickness and cyclic maximum film pressure

Each time step simulated predicts the same lubrication results. The largest time step (Δt = 0.0005s) is chosen for the stance phase simulations in this work due to its advantage in computing time. Larger time steps could not be used due to issues with convergence of the finite element lubrication program.

B.1.3 Fluid-film mesh validation

The finite element mesh employed for the lubrication analyses associated with the in-line design is investigated in this section. Four mesh densities are simulated using the in-line

geometry (a hemispherical cup with a clearance hole centered on the vertical (Z) axis). The mesh density study is performed under the generic case applied in Sections B.1.1 and B.1.2 (C_0 = 30μm, δ = 40μm, μ = 2.5 mPa-s, and p_{cav} = 0 kPa) with the exception that a sealed boundary condition (no flow) is adopted at the boundary nodes of the clearance hole. SmartSize free meshing is applied to the two-dimensional geometry to ensure that element sizes are similar in area. A time step of Δt = 0.0005s is used for this study. Figures B.3 through B.6 display equal area projections of the mesh densities evaluated under stance phase conditions at the 16mm cup geometry.

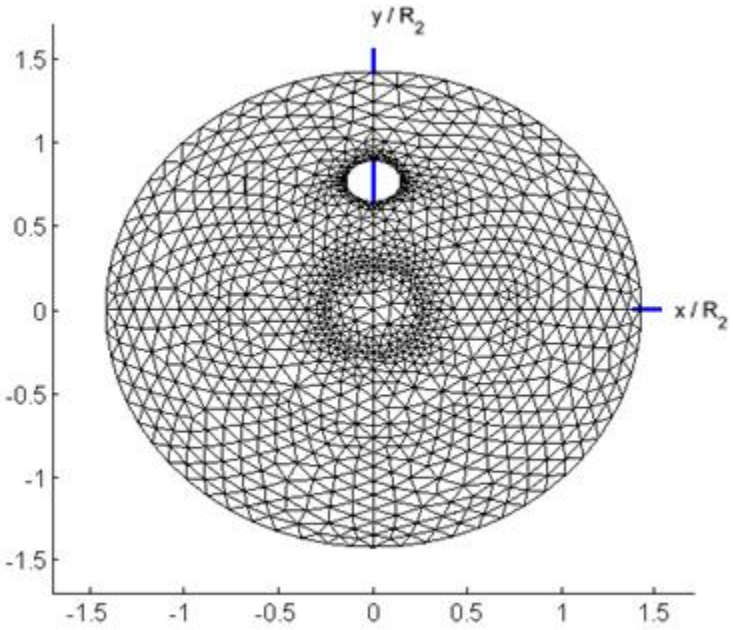

Figure B.3: Mesh B1

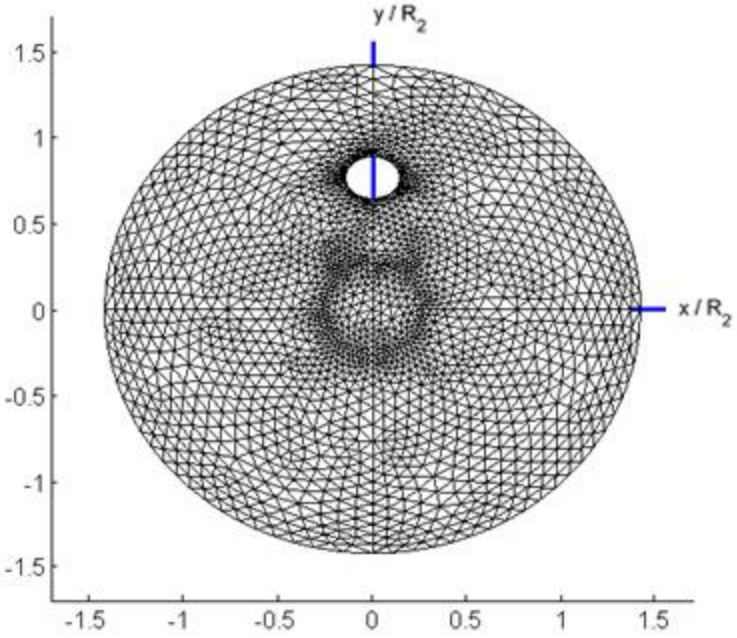

Figure B.4: Mesh B2

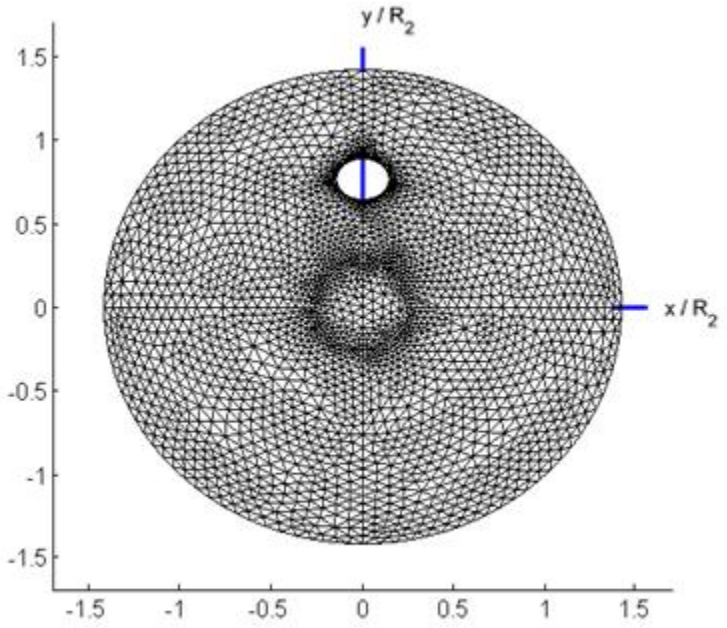

Figure B.5: Mesh B3

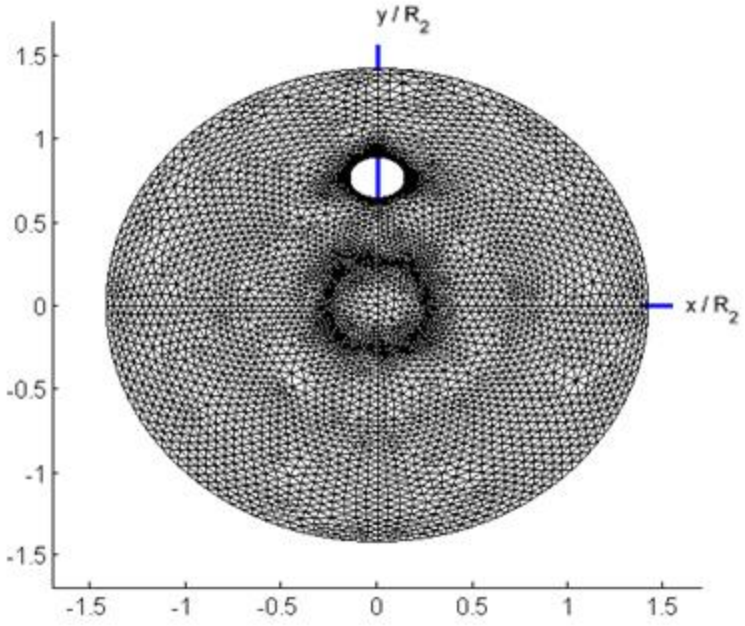

Figure B.6: Mesh B4

Table B.2 displays the results for the mesh density study. Cyclic minimum film thickness, cyclic maximum film pressure and computation time are the parameters used for the determination of the mesh density to use in this thesis. Moreover, Figure B.7 shows the time histories of minimum film thickness and maximum film pressure for each mesh density.

Mesh Density	**No. of Elements**	**Cyclic h_{min}**	**Cyclic p_{max}**	**Computation Time**
-	-	nm	MPa	s
B1	2122	162.44	14.76	130
B2	3898	180.87	14.41	400
B3	4946	186.37	14.45	555
B4	8430	192.70	14.43	1550

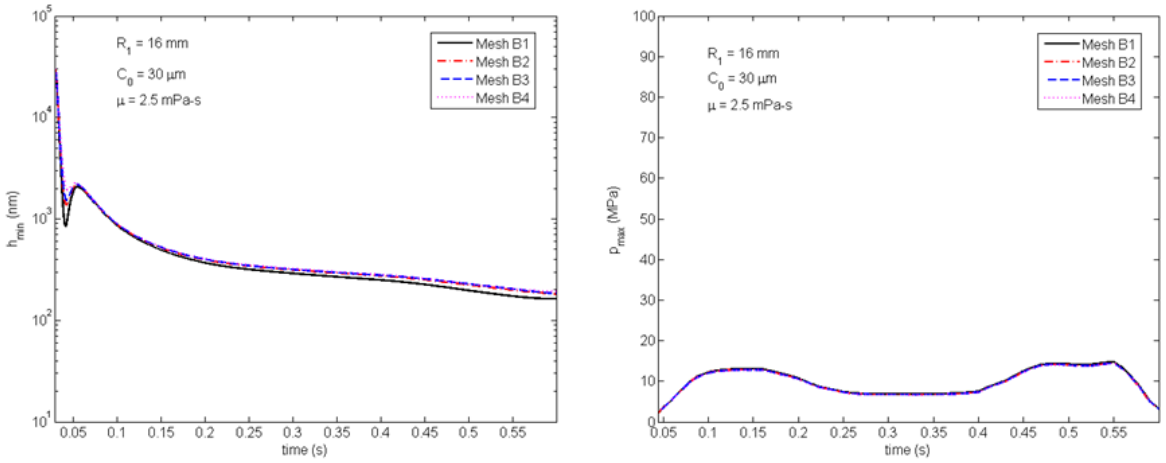

Figure B.7: Mesh density comparison

The shape of the minimum film thickness and maximum film pressure curves are nearly identical for meshes B2, B3 and B4. As such, the cyclic h_{min} and p_{max} values are used to determine convergence to a particular result. There is a difference of 3.3% in cyclic minimum film thickness and a difference of 0.1% in cyclic maximum film pressure between mesh B3 and the finest mesh B4. Due to the advantage in computing time for mesh B3 (2.8 times shorter than mesh B4) and the ability to obtain converged results, mesh B3 is chosen for the simulations in this thesis.

References:

[1] "About the Hip," Oxford University Hospitals, 2014, from http://www.ouh.nhs.uk/hipandknee/information/hip/joint-anatomy.aspx

[2] J. J. Callaghan, A. G. Rosenberg, and H. E. Rubash, *The Human Hip: Volume 1*, Second ed. Philadelphia, PA: Lippincott Williams and Wilkins, 2007.

[3] "Total Hip Replacements," American Academy of Orthopaedic Surgeons, 2011, from http://orthoinfo.aaos.org/topic.cfm?topic=a00377

[4] E. Ingham and J. Fisher, "The role of macrophages in osteolysis of total joint replacement," *Biomaterials,* vol. 26, pp. 1271-1286, 2005.

[5] J. L. Tipper, P. J. Firkins, E. Ingham, J. Fisher, M. H. Stone, and R. Farrar, "Quantitative analysis of the wear and wear debris from low and high carbon content cobalt chrome alloys used in metal on metal total hip replacements," *Journal of Materials Science: Materials in Medicine,* vol. 10, pp. 353-362, 1999.

[6] I. Catelas, J. B. Medley, P. A. Campbell, O. L. Huk, and J. D. Bobyn, "Comparison of in vitro with in vivo characteristics of wear particles from metal-metal hip implants," *Journal of Biomedical Materials Research - Part B Applied Biomaterials,* vol. 70, pp. 167-178, 2004.

[7] C. Brown, J. Fisher, and E. Ingham, "Biological effects of clinically relevant wear particles from metal-on-metal hip prostheses," *Proceedings of the Institution of Mechanical Engineers, Part H (Journal of Engineering in Medicine),* vol. 220, pp. 355-69, 2006.

[8] A. G. Cobb and T. P. Schmalzreid, "The clinical significance of metal ion release from cobalt-chromium metal-on-metal hip joint arthroplasty," *Proceedings of the Institution of Mechanical Engineers, Part H (Journal of Engineering in Medicine),* vol. 220, pp. 385-98, 2006.

[9] M. S. Bhamra and C. P. Case, "Biological effects of metal-on-metal hip replacements," *Proceedings of the Institution of Mechanical Engineers, Part H: Journal of Engineering in Medicine,* vol. 220, pp. 379-384, 2006.

[10] M. Sidebottom and M. Paliwal, "Friction-induced squeak of ceramic-on-ceramic hip implants: A stability design criteria," in *ASME 2012 International Mechanical Engineering Congress and Exposition, IMECE 2012, November 9, 2012 - November 15, 2012*, Houston, TX, United states, 2012, pp. 877-881.

[11] F. C. Wang and Z. M. Jin, "Effect of non-spherical bearing geometry on transient elastohydrodynamic lubrication in metal-on-metal hip joint implants," *Proceedings of the Institution of Mechanical Engineers, Part J (Journal of Engineering Tribology),* vol. 224, pp. 379-89, 2007.

[12] F. C. Wang, S. X. Zhao, A. F. Quinonez, H. Xu, X. S. Mei, and Z. M. Jin, "Nonsphericity of Bearing Geometry and Lubrication in Hip Joint Implants," *Journal of Tribology,* vol. 131, pp. 031201-11, 2009.

[13] Q. Meng, L. Gao, F. Liu, P. Yang, J. Fisher, and Z. Jin, "Contact mechanics and elastohydrodynamic lubrication in a novel metal-on-metal hip implant with an aspherical bearing surface," *Journal of Biomechanics,* vol. 43, pp. 849-857, 2010.

[14] H. McKellop, F. W. Shen, B. Lu, P. Campbell, and R. Salovey, "Development of an extremely wear-resistant ultra high molecular weight polyethylene for total hip replacements," *Journal of Orthopaedic Research,* vol. 17, pp. 157-167, 1999.

[15] M. P. Gispert, A. P. Serro, R. Colaco, E. Pires, and B. Saramago, "Wear of ceramic coated metal-on-metal bearings used for hip replacement," *Wear,* vol. 263, pp. 1060-1065, 2007.

[16] H. Koseki, H. Shindo, K. Baba, T. Fujikawa, N. Sakai, Y. Sawae*, et al.*, "Surface-engineered metal-on-metal bearings improve the friction and wear properties of local area contact in total joint arthroplasty," *Surface & Coatings Technology,* vol. 202, pp. 4775-9, 2008.

[17] J. Fisher, X. Q. Hu, J. L. Tipper, T. D. Stewart, S. Williams, M. H. Stone*, et al.*, "An in vitro study of the reduction in wear of metal-on-metal hip prostheses using surface-engineered femoral heads," *Proceedings of the Institution of Mechanical Engineers, Part H (Journal of Engineering in Medicine),* vol. 216, pp. 219-30, 2002.

[18] J. Fisher, X. Q. Hu, T. D. Stewart, S. Williams, J. L. Tipper, E. Ingham*, et al.*, "Wear of surface engineered metal-on-metal hip prostheses," *Journal of Materials Science: Materials in Medicine,* vol. 15, pp. 225-35, 2004.

[19] L. Mattei, F. Di Puccio, B. Piccigallo, and E. Ciulli, "Lubrication and wear modelling of artificial hip joints: A review," *Tribology International,* vol. 44, pp. 532-549, 2011.

[20] International Organization for Standardization, "ISO 14242-1: Implants for Surgery - Wear of Total Hip-Joint Prostheses - Part 1: Loading and Displacement Parameters for Wear Testing Machines and Corresponding Environmental Conditions for Test," ed, 2002.

[21] G. Bergmann, F. Graichen, and A. Rohlmann, "Hip joint loading during walking and running, measured in two patients," *Journal of Biomechanics,* vol. 26, pp. 969-990, 1993.

[22] G. Bergmann, G. Deuretzbacher, M. Heller, F. Graichen, A. Rohlmann, J. Strauss*, et al.*, "Hip contact forces and gait patterns from routine activities," *Journal of Biomechanics,* vol. 34, pp. 859-871, 2001.

[23] M. O. Heller, G. Bergmann, G. Deuretzbacher, L. Dürselen, M. Pohl, L. Claes*, et al.*, "Musculo-skeletal loading conditions at the hip during walking and stair climbing," *Journal of Biomechanics,* vol. 34, pp. 883-893, 2001.

[24] S. Boedo and J. F. Booker, "A Novel Elastic Squeeze Film Total Hip Replacement," *ASME Journal of Tribology*, vol. 136, pp. 011101, 2014.

[25] S. Boedo, J. F. Booker, and S. A. Coots, "Swing Phase Lubrication Analysis of A Novel Artificial Hip Joint," *2013 ASME International Mechanical Engineering Congress and Exposition*, November 13-21, 2013, San Diego, CA, Paper IMECE 2013-64356.

[26] A. Matthies, R. Underwood, P. Cann, K. Ilo, Z. Nawaz, J. Skinner*, et al.*, "Retrieval analysis of 240 metal-on-metal hip components, comparing modular total hip replacement with hip resurfacing," *Journal of Bone and Joint Surgery,* vol. 93-B, pp. 307-314, 2011.

[27] R. Underwood, A. Matthies, P. Cann, J. A. Skinner, and A. J. Hart, "A comparison of explanted Articular Surface Replacement and Birmingham Hip Resurfacing components " *Journal of Bone and Joint Surgery,* vol. 93-B, pp. 1069-1077, 2011.

[28] M. M. Morlock, N. Bishop, J. Zustin, M. Hahn, W. Rüther, and M. Amling, "Modes of Implant Failure After Hip Resurfacing: Morphological and Wear Analysis of 267 Retrieval Specimens," *Journal of Bone and Joint Surgery,* vol. 90, pp. Suppl 3: 89-95, 2008.

[29] E. Ebramzadeh, P. A. Campbell, K. M. Takamura, Z. Lu, S. N. Sangiorgio, J. J. Kalma*, et al.*, "Failure Modes of 433 Metal-on-Metal Hip Implants: How, Why, and Wear," *Orthopedic Clinics of North America,* vol. 42, pp. 241-250, 2011.

[30] T. A. Maxian, T. D. Brown, D. R. Pedersen, and J. J. Callaghan, "A sliding-distance-coupled finite element formulation for polyethylene wear in total hip arthroplasty," *Journal of Biomechanics,* vol. 29, pp. 687-692, 1996.

[31] J. F. Archard, "Contact and rubbing of flat surfaces," *Journal of Applied Physics,* vol. 24, pp. 981-988, 1953.

[32] L. Mattei, F. Di Puccio, and E. Ciulli, "A comparative study of wear laws for soft-on-hard hip implants using a mathematical wear model," *Tribology International,* vol. 63, pp. 66-77, 2013.

[33] T. A. Maxian, T. D. Brown, D. R. Pedersen, and J. J. Callaghan, "Adaptive finite element modeling of long-term polyethylene wear in total hip arthroplasty," *Journal of Orthopaedic Research,* vol. 14, pp. 668-675, 1996.

[34] L. Kang, A. L. Galvin, Z. M. Jin, and J. Fisher, "A simple fully integrated contact-coupled wear prediction for ultra-high molecular weight polyethylene hip implants," *Proceedings of the Institution of Mechanical Engineers, Part H (Journal of Engineering in Medicine),* vol. 220, pp. 33-46, 2006.

[35] F. E. Kennedy, "Biomechanics of the hip and knee: implant wear," in *Wear of Orthopaedic Implants and Artificial Joints*, S. Affatato, Ed., ed Oxford, UK: Woodhead Publishing Ltd., 2012, pp. 56-92.

[36] L. Kang, A. L. Galvin, T. D. Brown, J. Fisher, and Z. M. Jin, "Wear simulation of ultra-high molecular weight polyethylene hip implants by incorporating the effects of cross-shear and contact pressure," *Proceedings of the Institution of Mechanical Engineers, Part H: Journal of Engineering in Medicine,* vol. 222, pp. 1049-1064, 2008.

[37] F. Liu, A. Galvin, Z. Jin, and J. Fisher, "A new formulation for the prediction of polyethylene wear in artificial hip joints," *Proceedings of the Institution of Mechanical Engineers, Part H: Journal of Engineering in Medicine,* vol. 225, pp. 16-24, 2011.

[38] S. Boedo, J. F. Booker, and D. L. Bartel, "Elastohydrodynamic lubrication analysis of a hip simulator test machine: parametric studies," 1999.

[39] B. Bresler and J. P. Frankel, "Forces and moments in leg during level walking," *American Society of Mechanical Engineers -- Transactions,* vol. 72, pp. 27-36, 1950.

[40] N. W. Rydell, "Forces acting on the femoral head prosthesis. A study on strain gauge supplied prostheses in living persons," *Acta Orthopaedica Scandanavia*, vol. 37: Suppl 18, pp. 1-132, 1966.

[41] J. P. Paul, "Forces transmitted by joints in human body," *Institution of Mechanical Engineers -- Proceedings of Lubrication and Wear in Living and Artificial Human Joints,* vol. 181, pp. 8-15, 1966.

[42] G. Bergmann, F. Graichen, A. Rohlmann, A. Bender, B. Heinlein, G. N. Duda*, et al.*, "Realistic loads for testing hip implants," *Bio-Medical Materials and Engineering,* vol. 20, pp. 65-75, 2010.

[43] B. W. Stansfield, A. C. Nicol, J. P. Paul, I. G. Kelly, F. Graichen, and G. Bergmann, "Direct comparison of calculated hip joint contact forces with those measured using instrumented implants. An evaluation of a three-dimensional mathematical model of the lower limb," *Journal of Biomechanics,* vol. 36, pp. 929-936, 2003.

[44] R. A. Brand, D. R. Pedersen, D. W. Davy, G. M. Kotzar, K. G. Heiple, and V. M. Goldberg, "Comparison of hip force calculations and measurements in the same patient. ," *Journal of Anthroplasty,* pp. 45-51, 1994.

[45] T. P. Andriacchi and D. E. Hurwitz, "Gait biomechanics and the evolution of total joint replacement," *Gait & Posture,* vol. 5, pp. 256-264, 1997.

[46] A. Unsworth, "Cavitation in Human Joints," *Cavitation and Related Phenomena in Lubrication,* vol. D. Dowson, M. Godet, C. M. Taylor, eds., IMechE Publications Ltd., pp. 119-127, 1975.

[47] P. K. Goenka, "Effect of Surface Ellipticity on Dynamically Loaded Spherical and Cylindrical Joints and Bearings," Ph.D., Cornell University, Ithaca, NY, 1980.

[48] M. Kothari, J. F. Booker, and D. L. Bartel, "Analysis of Artificial Joints as Spherical Bearings," *Lubricants and Lubrication,* vol. D. Dowson, C. Taylor, T. Childs, G. Dalmaz, eds., Elsevier, pp. 93-98, 1995.

[49] J. Z. M. and D. Dowson, "A Full Numerical Analysis of Hydrodynamic Lubrication in Artificial Hip Joint Replacements Constructed From Hard Materials," *Proc. IMechE C: J. Mech. Eng. Sci.,* vol. 213, pp. 355-370, 1999.

[50] F. C. Wang and Z. M. Jin, "Prediction of elastic deformation of acetabular cups and femoral heads for lubrication analysis of artificial hip joints," *Proceedings of the Institution of Mechanical Engineers, Part J (Journal of Engineering Tribology),* vol. 218, pp. 201-9, 2004.

[51] J. Fan, C. W. Myant, R. Underwood, P. M. Cann, and A. Hart, "Inlet protein aggregation: a new mechanism for lubricating film formation with model synovial fluids," *Proceedings of the Institution of Mechanical Engineers, Part H (Journal of Engineering in Medicine),* vol. 225, pp. 696-709, 2011.

[52] C. Sprecher, R. Hauert, S. Grad, G. Tager, A. Fisher, and E. Schneider, "Solid Lubrication - A Relevant Lubrication Mechanism for Reducing Wear in Metal-on-Metal THA Components?," presented at the 49th Annual Meeting, ORS, 2003.

[53] A. Kumar and J. F. Booker, "A Finite Element Cavitation Algorithm," *ASME J. Trobol.,* vol. 113, pp. 276-286, 1991.

[54] J. F. Booker and S. Boedo, "Finite Element Analysis of Elastic Engine Bearing Lubrication: Application," *Revue Européenne des Éléments Finis,* vol. 10, pp. 725-740, 2001.

[55] J. F. Booker and S. Boedo, "Finite Element Analysis of Elastic Engine Bearing Lubrication: Theory," *Revue Européenne des Éléments Finis,* vol. 10, pp. 705-724, 2001.

[56] R. M. Streicher and R. Schoen, "Tribological behaviour of various materials and surfaces against polyethylene," in *17th Annual Meeting of the Society for Biomaterials in conjunction with the 23rd International Biomaterials Symposium, May 1, 1991 - May 5, 1991*, Scottsdale, AZ, USA, 1991, p. 289.

[57] L. Mattei and F. Di Puccio, "Wear simulation of metal-on-metal hip replacements with frictional contact," *Journal of Tribology,* vol. 135, 2013.

[58] C. Brockett, S. Williams, Z. Jin, G. Isaac, and J. Fisher, "Friction of total hip replacements with different bearings and loading conditions," *Journal of Biomedical Materials Research - Part B Applied Biomaterials,* vol. 81, pp. 508-515, 2007.